

AD-A253 463



WL-TR-91-2101



## OPTICAL DIAGNOSTICS IN SUPERSONIC COMBUSTING SYSTEMS

T.E. Parker, M.G. Allen, S.J. Davis, K. Donohue, R.R. Foutter,  
H.H. Legner, W.T. Rawlins, and Wm. G. Reinecke  
Physical Sciences Inc.  
20 New England Business Center  
Andover, MA 01810

April 1992

DTIC  
ELECTE  
JUL 30 1992  
S A D

Final Report for the Period December 1988 - July 1991

Approved for public release; distribution unlimited.

AERO PROPULSION & POWER DIRECTORATE  
WRIGHT LABORATORY  
AIR FORCE SYSTEMS COMMAND  
WRIGHT-PATTERSON AIR FORCE BASE, OHIO 45433-6503

92-20546

92 7

REPORT DOCUMENTATION PAGE			Form Approved OMB No. 0704-0188
<p>Public reporting burden for this collection of information is estimated to average 1 hour per response, including the time for reviewing instructions, searching existing data sources, gathering and maintaining the data needed, and completing and reviewing the collection of information. Send comments regarding this burden estimate or any other aspect of this collection of information, including suggestions for reducing this burden, to Washington Headquarters Services, Directorate for Information Operations and Reports, 1215 Jefferson Davis Highway, Suite 1204, Arlington, VA 22202-4302, and to the Office of Management and Budget, Paperwork Reduction Project (0704-0188) Washington, DC 20503.</p>			
1. AGENCY USE ONLY (Leave blank)	2. REPORT DATE	3. REPORT TYPE AND DATES COVERED	
	April 1992	FINAL DEC 1988 - JUL 1991	
4. TITLE AND SUBTITLE		5. FUNDING NUMBERS	
Optical Diagnostics in Supersonic Combusting Systems		C - F33615-88-C-2907 PE - 65502F PO - 3005 TA: 21 WV: 29	
6. AUTHOR(S)			
T.E. Parker, M.G. Allen, S.J. Davis, K. Donohue, R.R. Foutter, H.H. Legner, W.T. Rawlins, and Wm. G. Reinecke			
7. PERFORMING ORGANIZATION NAME(S) AND ADDRESS(ES)		8. PERFORMING ORGANIZATION REPORT NUMBER	
Physical Sciences Inc. 20 New England Business Center Andover, MA 01110		✓PSI-1067/TR-1133	
9. SPONSORING/MONITORING AGENCY NAME(S) AND ADDRESS(ES)		10. SPONSORING/MONITORING AGENCY REPORT NUMBER	
John R. Smith (513) 255-2175 Wright Laboratory Aero Propulsion and Power Directorate (WL/POPR) Wright-Patterson AFB, OH 45433-6503		WL-TR-91-2101	
11. SUPPLEMENTARY NOTES			
12a. DISTRIBUTION/AVAILABILITY STATEMENT		12b. DISTRIBUTION CODE	
Approved for public release; distribution is unlimited.			
13. ABSTRACT (Maximum 200 words)			
<p>The development of supersonic combusting ramjet (SCRAMJET) engines requires testing using new, nonintrusive, instrumentation methods in high-speed, high-enthalpy flow facilities. This report describes a test series using a shock tunnel to produce Mach 3.0 flows with stagnation temperatures in excess of 3000 K and an optical diagnostic set specifically tailored for measurements in supersonic high temperature systems. The test facility includes a hydrogen injection capability which makes combustion tests possible for these flows. The report describes the shock tunnel and its capabilities, provides an overview of the optical diagnostics used in the test, and discusses the results of both combusting and noncombusting tests.</p> <p>The optical measurements include concentration and vibrational temperature for NO upstream of the combustion region (via spectrally resolved emission measurements), Planar Laser</p>			
14. SUBJECT TERMS		15. NUMBER OF PAGES	
Scramjet, Scramjet combustor, optical diagnostics		167	
		16. PRICE CODE	
17. SECURITY CLASSIFICATION OF REPORT	18. SECURITY CLASSIFICATION OF THIS PAGE	19. SECURITY CLASSIFICATION OF ABSTRACT	20. LIMITATION OF ABSTRACT
Unclassified	Unclassified	Unclassified	UL

**Unclassified**

**SECURITY CLASSIFICATION OF THIS PAGE**

**CLASSIFIED BY**

**DECLASSIFY ON**

**13. ABSTRACT (Continued)**

Induced Fluorescence (PLIF) imaging of both NO and OH (yielding either concentration or temperature information), and Schlieren photography. In addition, an OH absorption measurement strategy is discussed. This diagnostic set is particularly appropriate since it includes both line-of-sight and spatially resolved measurements and additionally, comparison of results from each of the techniques is possible.

**SECURITY CLASSIFICATION OF THIS PAGE**

**Unclassified**

## Contents

<b>Figures</b>	iv
<b>Tables</b>	ix
<b>Acknowledgement</b>	x
<b>Executive Summary</b>	1
<b>Introduction</b>	4
<b>Shock Tunnel Design and Performance</b>	6
<b>Introduction</b>	6
<b>Shock Tube Theory</b>	7
<b>Shock Tunnel Design</b>	19
Chemistry Effects on Shock Tunnel Design and Performance	32
<b>Shock Tunnel Hardware Description</b>	37
<b>Shock Tunnel Injection System</b>	42
<b>Shock Tunnel System Performance</b>	46
<b>Optical Diagnostic Methods and Results</b>	51
<b>Introduction</b>	51
<b>Flowfield Predictions</b>	51
<b>Schlieren Measurements</b>	53
<b>Infrared Emission Measurements of NO</b>	59
<b>OH Absorption Measurements</b>	71
<b>Planar Laser-Induced Fluorescence Measurements</b>	80
<b>Discussion of Results</b>	132
<b>Conclusions</b>	138
<b>References</b>	140
<b>Appendix - OH Absorption</b>	143

Accession For	
<input checked="" type="checkbox"/> NTIS CRA&I <input type="checkbox"/> DTIC TAB <input type="checkbox"/> Unannounced <input type="checkbox"/> Justification	
By _____	
Distribution / _____	
Availability Codes	
Dist	Available / or Special
A-1	

## List of Figures

<u>Figure</u>		<u>Page</u>
1	Pressure Ratio as a Function of Incident Shock Mach Number .....	8
2	Reflected Shock Temperature and Pressure Ratio as a Function of Mach Number .....	9
3	Wave Diagram for Shock Tube Including Contact Surface Trajectory for Idealized Flow and Flow Including Boundary Layer .....	11
4	Shock Wave and Contact Surface Interactions .....	12
5	Test Time in a Shock Tube .....	14
6	Test Times for 12.0m Test Section Length .....	15
7	Boundary Layer Development in the Shock Tube .....	16
8	Required Driver Length as a Function of No-Reaction, Reflected Shock Temperatures .....	20
9	Relative Nozzle Throat Size for Test Section Lengths 5.55, 8.0, and 12.0m .....	22
10	Secondary Diaphragm Location .....	24
11	Conceptual Description of a Detonation Wave .....	28
12	Pressure Ratio for a Stoichiometric H <sub>2</sub> /Air Mixture as a Function of Initial Temperature .....	29
13	Pressure Ratios for a Room Temperature Mixture as a Function of Stoichiometry (less than 1.0 is a fuel-lean mixture) .....	30
14	Chemistry Effects on the Reflected Shock Zone Temperature .....	33
15	Vibrational Nonequilibrium in Mach 3 Air .....	36
16	Schematic Diagram of Shock Tunnel Facility .....	37

## List of Figures (Continued)

<u>Figure</u>		<u>Page</u>
17	Optical Access in the Shock Tunnel . . . . .	40
18	Hydrogen Injector for Shock Tunnel Experiments . . . . .	42
19	Fuel-to Air Ratio for Initial Shock Tunnel Tests . . . . .	45
20	Shock Tunnel Test Times Compared with Modeling Results . . . . .	47
21	Shock Tunnel Operating Pressures and Temperatures . . . . .	48
22	Shock Tunnel Operating Envelope Compared to the NASP Flight Corridor . . . . .	49
23	Graphic Representation of the Flowfield in the Shock Tunnel Without Injection . . . . .	52
24	Shock Tunnel Flowfield with Injection Along the Centerline of the Tunnel . . . . .	54
25	Schlieren Image of Flow over the Rearward Facing Step . . . . .	55
26	Schlieren Image of a Helium Plume into a Vacuum . . . . .	56
27	Schlieren Image of Helium Injection into Flow Behind the Rearward Facing Step . . . . .	57
28	Calibration Spectra for NO From Shock Tube Experiments . . . . .	61
29	Observed Band Integrated Radiance Compared to Calculated Values for NO . . . . .	62
30	NO Radiance as a Function of Temperature and Wavelength . . . . .	64
31	Dependence of NO(v) Radiance Ratios on Temperature . . . . .	65
32	NO Spectra in the Shock Tunnel for Several Times During the Flow . . . . .	66

## List of Figures (Continued)

<u>Figure</u>		<u>Page</u>
33	Temperature Measurements Based on NO Emission from a Mach 3.0 Flow . . . . .	66
34	NO Concentration as Measured in the Shock Tunnel . . . . .	67
35	Flow Temperature from NO Radiation in the Mach 3.0 Flow Compared with an Idealized Computed Value . . . . .	67
36	NO Concentration in the Shock Tunnel Based on Radiometer Measurements . . . . .	68
37	Illustration of Absorption and Source Lines Modeled as Triangles . . . . .	74
38	Ground State Partition Function for Selected OH Absorption Lines . . . . .	75
39	Measured Absorption for the Arc Lamp System and Predicted Number Densities of OH . . . . .	78
40	Schematic Diagram of Arc Lamp Measurement System . . . . .	78
41	Comparison of Radiance from Thermally Excited OH(A→X) with an Arc Lamp and Microwave Discharge Lamp . . . . .	81
42	Typical PLIF Experimental Setup . . . . .	82
43	Typical Pulse Energies Available From Frequency-Doubled Excimer-pumped Dye Lasers . . . . .	84
44	Responsivity of Intensified Camera System . . . . .	88
45	Quantum Efficiency of Intensifier as a Function of Wavelength . . . . .	89
46	Schematic Energy Level Diagram Showing Important Processes in Laser-Induced NO Fluorescence . . . . .	93
47	Effective Radiative Transition Rate for NO Fluorescence Strategy . . . . .	95
48	Rotational Branches of NO A-X Transitions . . . . .	96

## List of Figures (Continued)

<u>Figure</u>		<u>Page</u>
49	Schematic Diagram of Top-Hat Laser Profile and Absorption Lineshape Overlap . . . . .	101
50	Experimental Setup for Pulse Laser Excitation Scans . . . . .	104
51	Room Temperature NO Pulsed Laser Excitation Scan . . . . .	105
52	NO Excitation Scan Detail - 300 K . . . . .	106
53	Calculated and Measured Fluorescence Attenuation at Nozzle Exit Plane . . . . .	108
54	NO PLIF Distribution Without Injection . . . . .	110
55	NO PLIF Distribution With Injection . . . . .	110
56	Comparison of Predicted and Measured NO PLIF Signal Variations With Temperature . . . . .	113
57	Schematic Energy Level Diagram Showing Important Processes in Laser-Induced OH Fluorescence . . . . .	116
58	OH Fluorescence Collection Filter Transmission Efficiency . . . . .	117
59	Temperature Dependence of OH Fluorescence for Constant OH Number Density . . . . .	123
60	Flame Temperature OH (1,0) Band Excitation Scan . . . . .	125
61	OH (1,0) Band Excitation Scan Detail . . . . .	125
62	Instantaneous OH Distribution in H <sub>2</sub> Injector Near Field, Injector 1 . . . . .	126
63	OH PLIF Images at Second Injector Station . . . . .	127
64	OH Image 23 Step Heights Downstream of Step . . . . .	128
65	Optical Access Stations and the Relative Locations of the Rearward Facing Step and the Injector Tubes . . . . .	133

**List of Figures (Continued)**

<u>Figure</u>		<u>Page</u>
66	Overlay of Schlieren and PLIF Images of the Recompression Shock After the Rearward Facing Step . . . . .	133
67	Comparison of Schlieren and PLIF Images of Helium Injectant into the Flow Behind a Rearward Facing Step . . . . .	134
68	Comparison of PLIF Images of Helium Injection and Hydrogen Injection Behind a Rearward Facing Step . . . . .	136

## LIST OF TABLES

<u>Table</u>		<u>Page</u>
1	Dump Tank Size as a Function of Plenum Temperature . . . . .	27
2	Tunnel Pressures for a Detonation During Operation . . . . .	31
3	Changes Due to Chemical Reactions in a Mach 3.0 Nozzle . . . . .	35
4	Shock Tunnel Major Components List . . . . .	38
5	Hydrostatic Test Pressures . . . . .	41
6	Relative Flow Properties . . . . .	53
7	NO(v) Spectral Calibration . . . . .	62
8	OH 0-0 Band Lines with 0.6Å Separation . . . . .	72
9	OH Absorption at Approximately 30 atm and 1500 to 1600 K . . . . .	77
10	Linewidths and Shifts for NO Fluorescence . . . . .	104
11	Linewidths and Shifts for OH Fluorescence . . . . .	124

## **ACKNOWLEDGEMENT**

We are deeply grateful to the continued enthusiasm and support of John Smith, our Contract Monitor at Wright Laboratory.

## 1. EXECUTIVE SUMMARY

The development of supersonic combusting ramjet (SCRAMJET) engines requires testing using new, nonintrusive, instrumentation methods in high speed, high enthalpy flow facilities. The stagnation temperatures for very high flight speeds (in excess of 3000 K) make the production of these flows impossible using conventional methods such as resistance heaters or vitiated flows. Similarly, measurements of properties in these flows is difficult since the measurement must be non-intrusive in nature. This report describes a test series using a shock tunnel to produce Mach 3.0 flows with stagnation temperatures in excess of 3000 K and an optical diagnostic set specifically tailored for measurements in supersonic high temperature systems. The test facility includes a hydrogen injection capability which makes combustion tests possible for these flows. The report describes the shock tunnel and its capabilities, provides an overview of the optical diagnostics used in the testing, and discusses the results of both combusting and noncombusting tests.

The shock tunnel was designed and constructed as a part of this program and is configured to operate at Mach 3.0 with a two-dimensional half nozzle expanding to a 7.62 cm square cross section. This is followed by a 1.27 cm rearward facing step in one of the four walls. Hydrogen injection ports are included in the tunnel wall after the rearward facing step along the tunnel centerline at 2.3 and 8.4 step heights downstream and are directed at 30 and 60 deg angles with respect to the tunnel flow. The system is modular in nature and includes both a replaceable nozzle and injector block. Optical access is included upstream of the rearward facing step, at each of the injector locations, and at three subsequent downstream

locations. The shock tube used to drive the shock tunnel is a 15.6 cm diameter system consisting of a 4m driver section, a 14m shock tube, a transition section/secondary diaphragm station for separating the shock tube from the tunnel flow section, and a dump tank after the tunnel flow section.

As with all pulsed type flow devices, the time duration of the high temperature flow is a critical performance parameter. The relationship between test time and flow temperatures has been analytically predicted and experimentally confirmed to be between 1 and 3 ms for stagnation temperatures between 4000 and 2500 K respectively. Static flow pressures for the reported tests are approximately 0.5 atm but are not limited to this value. Substantially higher stagnation pressures are possible using hydrogen or hydrogen/helium mixes as the driver gas.

The optical diagnostic measurements are a second critical capability for this work. These measurements include concentration and vibrational temperature for NO upstream of the combustion region (via spectrally resolved emission measurements), Planar Laser Induced Fluorescence (PLIF) imaging of both NO and OH (yielding either concentration or temperature information), and Schlieren photography. In addition, an OH absorption measurement strategy is discussed. This diagnostic set is particularly appropriate since it includes both line-of-sight and spatially resolved measurements and additionally, comparison of results from each of the techniques is possible.

Results from this work include Schlieren and PLIF images of the injection zone and line-of-sight NO concentration and temperature measurements. The line-of-sight NO emission measurement was used to verify absolute concentration measurements from the NO PLIF results. In addition, the observed temperature dependence of the NO PLIF signal was shown to be in relative agreement with the temperature variations imposed by the flowfield. NO PLIF measurements were also made in the near injector region for a non-combusting flow and clearly show the bow shock produced by injection and the mixing zone between injectant and mainstream gases. Images in the near injector zone using OH PLIF also clearly show the reaction zones for combusting tests indicating prompt ignition of the hydrogen jet.

In conclusion, the results described in this report are uniquely appropriate to the development of scram jet engines since the necessary flow conditions are created and a comprehensive optical diagnostic set is used to monitor the high speed, high enthalpy combusting flow.

## 2. INTRODUCTION

The development of supersonic combusting ram jet (SCRAMJET) engines requires testing using new, nonintrusive, instrumentation methods in high-speed, high enthalpy flow facilities. The stagnation temperatures for very high flight speeds (in excess of 3000 K) make the production of these flows impossible using conventional methods such as resistance heaters or vitiated flows. Similarly, property measurements in these flows are difficult since the measurement methods must be nonintrusive in nature. Physical Sciences Inc. (PSI) has completed an initial test series using a shock tunnel to produce Mach 3.0 flows with stagnation temperatures in excess of 3000 K and an optical diagnostic set specifically tailored for measurements in supersonic high temperature systems. A hydrogen injection capability is included which makes combustion tests possible. The optical measurements include both spatially resolved and line-of-sight averaged concentration and temperature measurements. This report describes the development and performance of a shock tunnel facility capable of simulating high-speed flight conditions, provides an in-depth discussion of the optical diagnostic techniques which were developed for this facility, and presents a series of test results for both noncombusting and combusting flows.

Chapter 3 discusses the details of the shock tunnel design and describes its performance, while Chapter 4 provides a complete description of the optical measurement methods applied to this facility. These methods include schlieren photography, spectrally resolved infrared emission measurements (to determine the concentration and temperature of NO), OH absorption measurements and PLIF measurements of NO and OH. Chapter 5 describes

important results from the initial test series, and Conclusions are given in Chapter 6. References are organized in Chapter 7 and details of OH absorption measurements are found in the Appendix.

### **3. SHOCK TUNNEL DESIGN AND PERFORMANCE**

#### **3.1 Introduction**

Ground testing of simulated SCRAMJET flows requires both a facility capable of producing high enthalpy flows and nonintrusive measurement methods for probing these flows. A shock tunnel is a unique method for producing the high temperature, high-speed flows and is not subject to the temperature limitations of resistance heated systems or vitiated flows. The shock tunnel is simply a shock tube which is used to drive a flow in a transient, blow-down wind tunnel and its primary use is the production of flow conditions which are unattainable by conventional means. Shock tubes routinely produce temperatures in excess of 4000 K in air at pressures of 100 atm or more. These conditions can be used as the stagnation conditions which drive a flow through a nozzle and into a constant Mach number flow section. The shock tunnel can be used to produce a variety of stagnation temperatures and pressures and therefore includes a certain degree of flexibility in terms of the flow conditions which it can produce.

The remainder of this chapter describes the details of the shock tunnel and its performance characteristics. Section 3.2 briefly describes the theory of shock tubes, Section 3.3 discusses the shock tunnel design, and Section 3.4 discusses the role of chemical reactions in the shock tunnel's performance. Section 3.5 describes the system hardware. Section 3.6 gives details of the hydrogen injection system, and Section 3.7 discusses system performance.

### 3.2 Shock Tube Theory

The shock tube is used to produce a localized region of high temperature and high pressure gas which can be used to drive the flow through the shock tunnel. This report will not reiterate the details of idealized shock tube operation since the subject is very adequately documented in the literature.<sup>1,2</sup> However, an overview of shock tube performance, including the effect of boundary layers, will be included in this section.

The type of shock tube used for this work was a constant diameter pipe with a breakable diaphragm separating the pipe into two chambers. The two sections of the pipe are gas pressurized to different pressures; when the diaphragm ruptures a shock wave propagates into the low pressure gas thereby increasing its temperature and pressure. The shock wave travels down the tube, reflects off the end wall, and travels back toward the diaphragm. The gas near the shock tube end wall has therefore been processed twice by shock waves and can be at very substantially increased temperatures and pressures. This region of high enthalpy gas is used as a reservoir to drive the flow in the shock tunnel and from a design standpoint its properties, time duration, and spatial extent are of extreme importance.

The temperature and pressure in the reflected shock region described above are direct functions of the pressure ratio across the diaphragm immediately before rupture, the initial pressure in the low pressure region of the tube, and the speed of sound and specific heat ratio of the gases used in the tube. These relationships are well documented and may be found in the literature.<sup>1,2</sup> For a given system of driver and driven gases, increased pressure ratio across the diaphragm increases the strength of the shock which is produced.

Temperature in the reflected shock region is therefore a function of pressure ratio. Similarly, pressure in the reflected region is determined by the pressure ratio across the diaphragm, since the pressure ratio across a shock is a function of the shock mach number, and the initial pressure in the driven section of the tube. An example of the functional dependence of incident shock Mach number on pressure ratio is given in Figure 1 and the dependence of reflected shock temperature and pressure as a function of Mach number is given in Figure 2. The shock tunnel uses the reflected shock region as a high temperature and pressure reservoir upstream of a supersonic nozzle. However, the reflected shock region is transient in nature; gas temperature and pressure are lowered by the arrival of either the contact surface (the interface between the original two gases) or the rarefaction wave (an

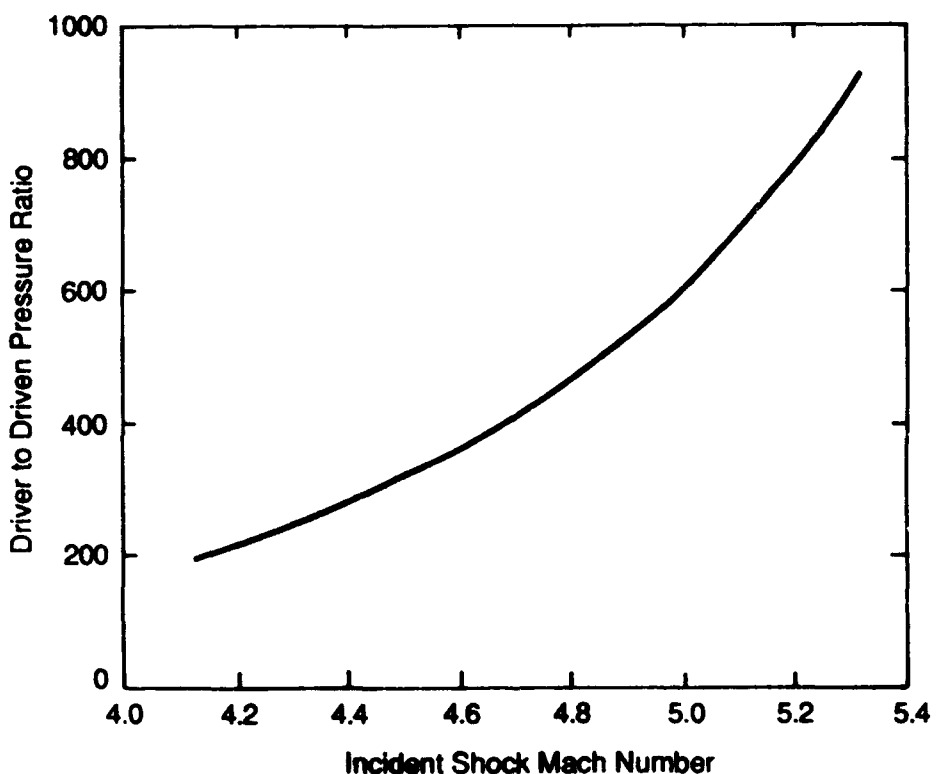


Figure 1

Pressure Ratio as a Function of Incident Shock Mach Number

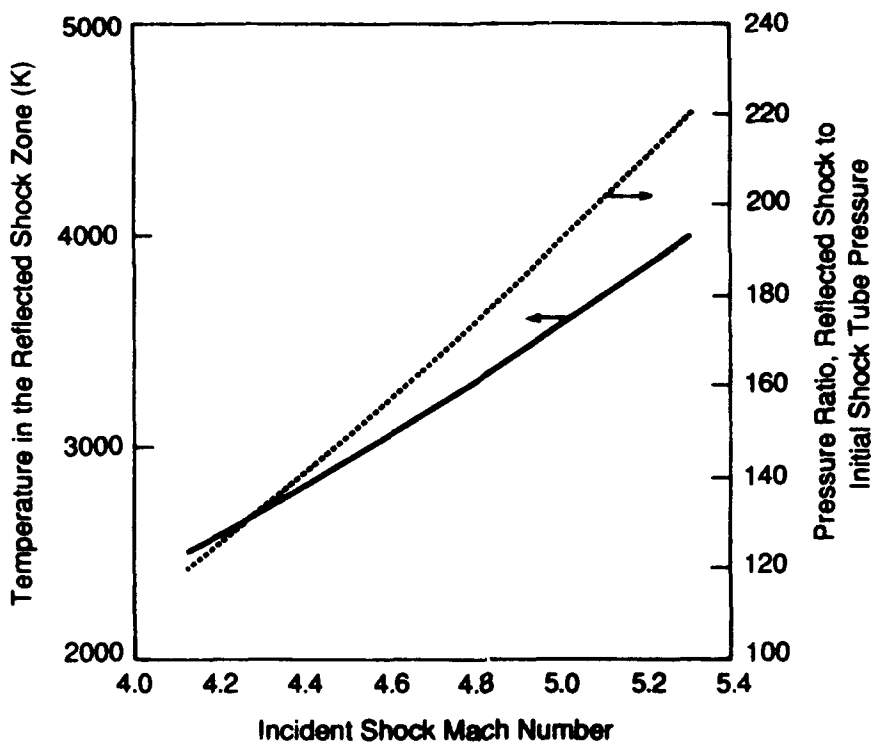


Figure 2

#### Reflected Shock Temperature and Pressure Ratio as a Function of Mach Number

expansion wave originating at the diaphragm). The duration of the high temperature and pressure reflected shock region, commonly known as the test time, is a function of initial pressure ratio and shock tube length.

The relationships of temperature, pressure, and test time for given set of initial conditions can be expressed as straightforward, albeit cumbersome, algebraic expressions for the idealized shock tube. However, non-idealities in system performance such as the existence of a boundary layer in the flow which follows the incident shock seriously complicate the prediction of shock tube performance. From a shock tunnel design standpoint, the system parameters which must be predicted are the time duration and length of the reflected shock

region. These two parameters describe maximum values for the duration of the flow in the tunnel and the mass available for the tunnel flow.

Boundary layer effects clearly play a critical role in the shock tunnel deviation from ideal performance and an excellent summary of shock tube boundary layers is given by Mirels.<sup>3</sup>. In addition to developing analytic and computational models for shock tube boundary layers, Mirels<sup>4</sup> has included the effect of the boundary layer on the separation distance between the shock and the contact surface. His analysis relies upon a comparison of the mass flow across the incident shock with the mass flow through the boundary layer at the contact surface. The difference in mass flow forces the distance between shock and contact surface to increase. When the mass flow across the two surfaces is equal, the system is said to have reached "limiting separation". Limiting separation for a 6 in diameter shock tube implies test section lengths far beyond the size of our existing laboratory.

In order to realistically estimate shock tunnel test times and the mass available to drive the flow in the shock tunnel, we have assembled a simple computational model of boundary layer effects as they relate to the trajectory of the incident shock and contact surface, the reflected shock's trajectory through the flow behind the incident shock, and the ultimate intersection of the reflected shock with the contact surface. This model allows prediction of the flow properties as a function of position behind the incident shock, the properties of the fluid on the shock side of the contact surface, the length of the high enthalpy stagnation region which will drive the flow in the shock tunnel, and the time required for the reflected shock to travel from the end wall to the contact surface. The length of the stagnation region is important

since it sets an upper bound on the total mass which can be exhausted into the shock tunnel. Working time in the shock tube is also important since it controls the shock tunnel flow duration.

Figure 3 illustrates the relevant wave behavior in a shock tube for both an idealized system and one that includes boundary layers. The clear effect of the boundary layer is to accelerate the contact surface thereby diminishing the test time available in the shock tunnel.

The shock wave interactions that will control test times in the nozzle are shown in Figure 4. We have defined two times for the system, a secondary shock limited time and a contact surface limited time. The time limit due to secondary reflected shock arises from the wave created by the shock/contact surface interaction (intersection (1) on the figure) and is a

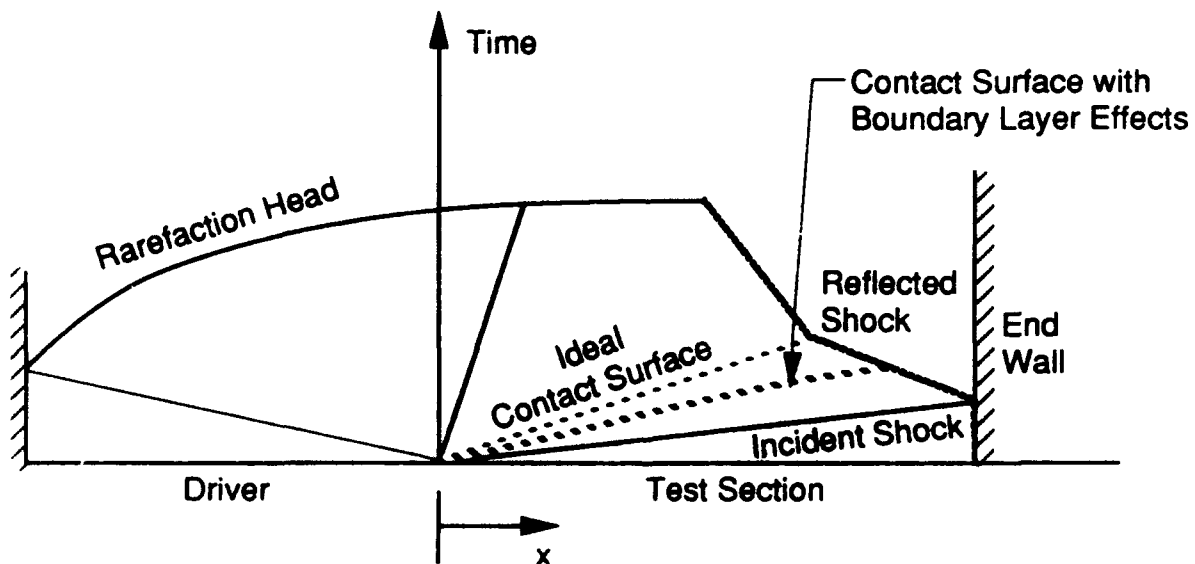


Figure 3

Wave Diagram for Shock Tube Including Contact Surface Trajectory for Idealized Flow and Flow Including Boundary Layer

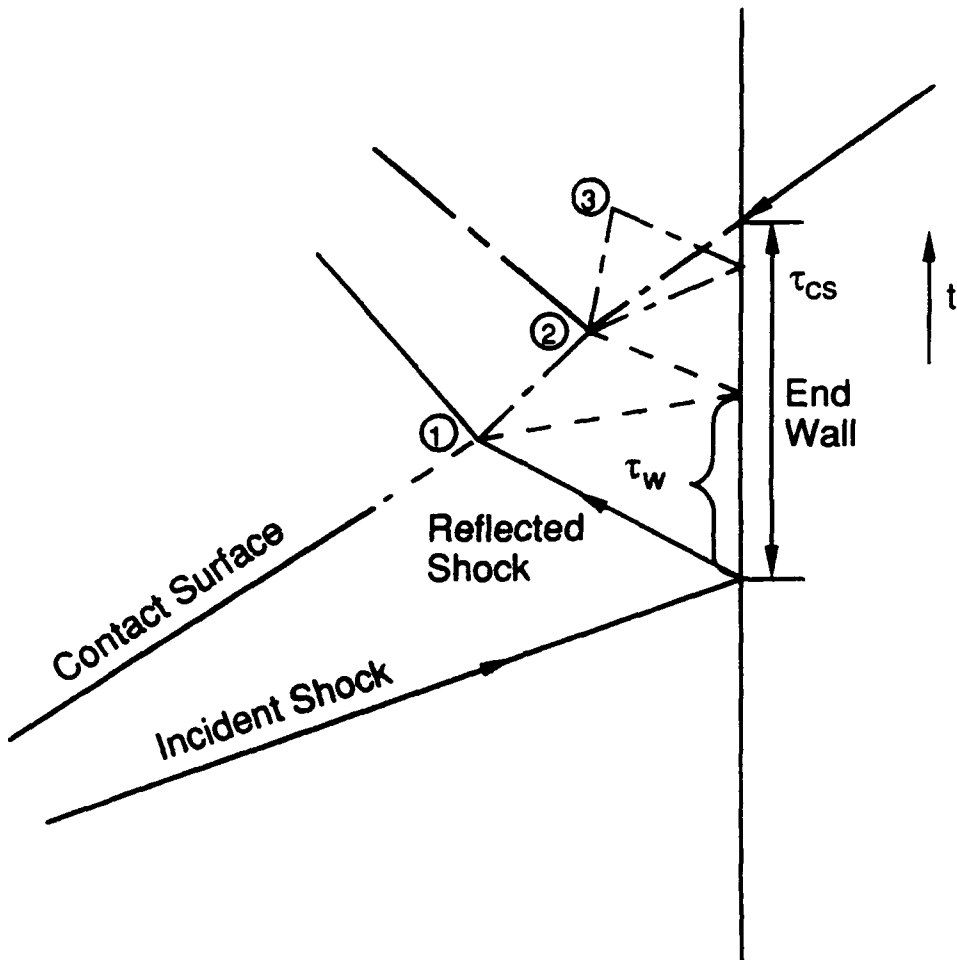


Figure 4  
Shock Wave and Contact Surface Interactions

concern for experiments that need precisely controlled temperatures ( $\tau_w$  in Figure 4). The shock tunnel has no such requirement and the test time can be approximated by extrapolating the contact surface motion from interaction (1) to the end wall. This estimate gives a conservative bound on the actual test time ( $\tau_{cs}$  in Figure 4). The shock/contact surface interaction solution has been integrated into our shock tube codes with the end result being a prediction of shock tube test times.

Results from these calculations are shown in Figures 5 and 6, corresponding to test section lengths 5.66 and 12.0m. The design curve for the shock tunnel is the contact surface limited test time including boundary layer effects. Note the dramatic increase in test time as the tailored interface condition of approximately 2000 K is approached. Figure 6 illustrates the clear benefit of increased shock tube length.

The shock tube/boundary layer model also provides a means of estimating the variation of properties which can be expected in the reflected shock zone. The development of the boundary layer model is based on the premise that the leading edge of the boundary layer is at the incident shock front, as shown in Figure 7. The model is developed in a reference frame in which the incident shock is stationary; for this reference frame, the shock tube wall moves with the speed of the incident shock. Note that in the incident shock reference frame the boundary layer flow has a larger velocity than the free stream flow. Boundary layer thickness grows as a function of distance from the incident shock and for a fully turbulent boundary layer this growth can be approximated by Eq. (1):

$$\delta \sim \ell^{1-n} \left[ \frac{v_w}{u_w - u_e} \right]^n \quad (1)$$

where:

- $n$  = 1/5 for turbulent; 1/2 for laminar
- $\ell$  = distance from incident shock
- $u_e$  = free stream velocity
- $u_w$  = wall velocity
- $v_w$  = viscosity at the wall.

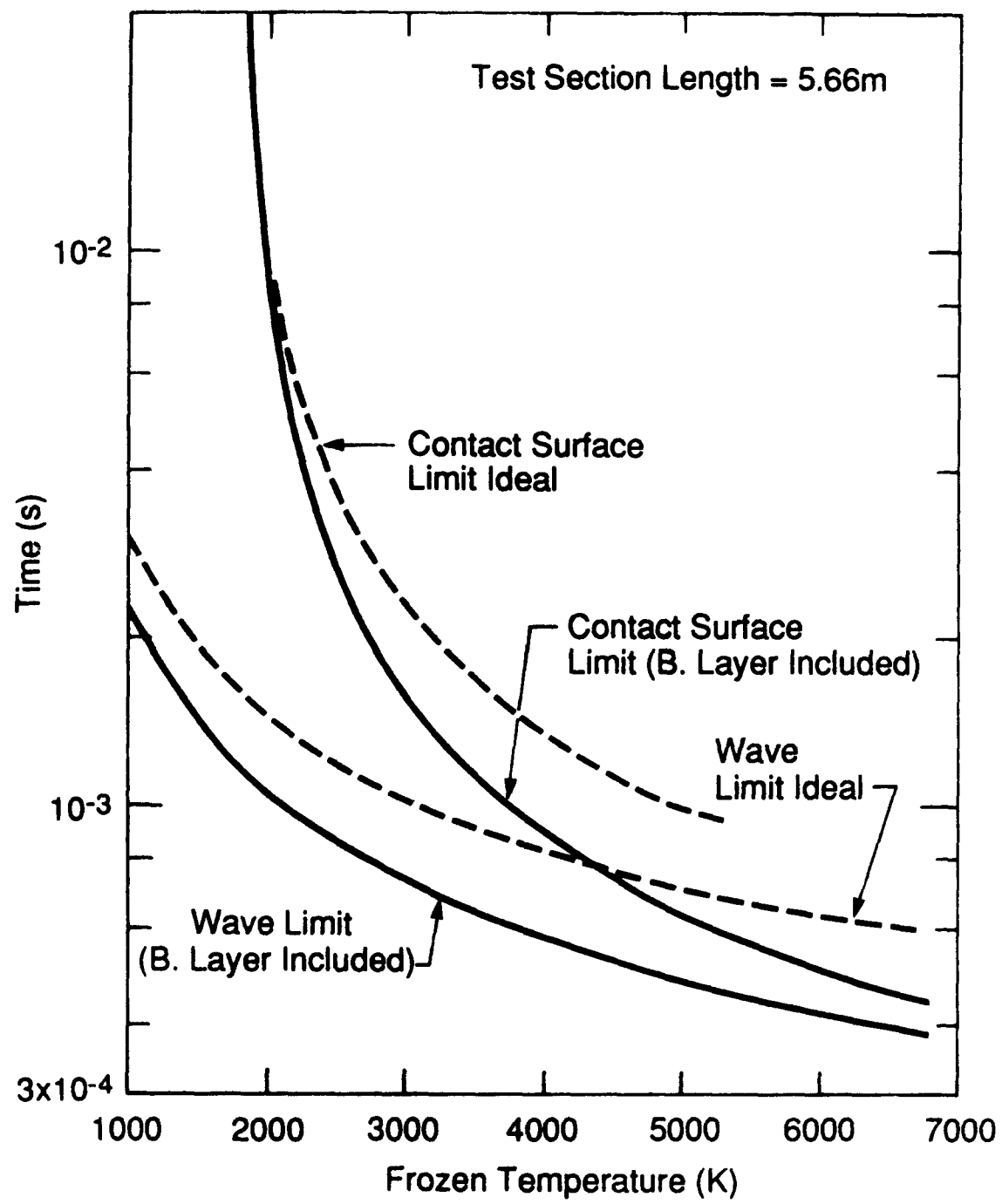


Figure 5  
Test Time in a Shock Tube

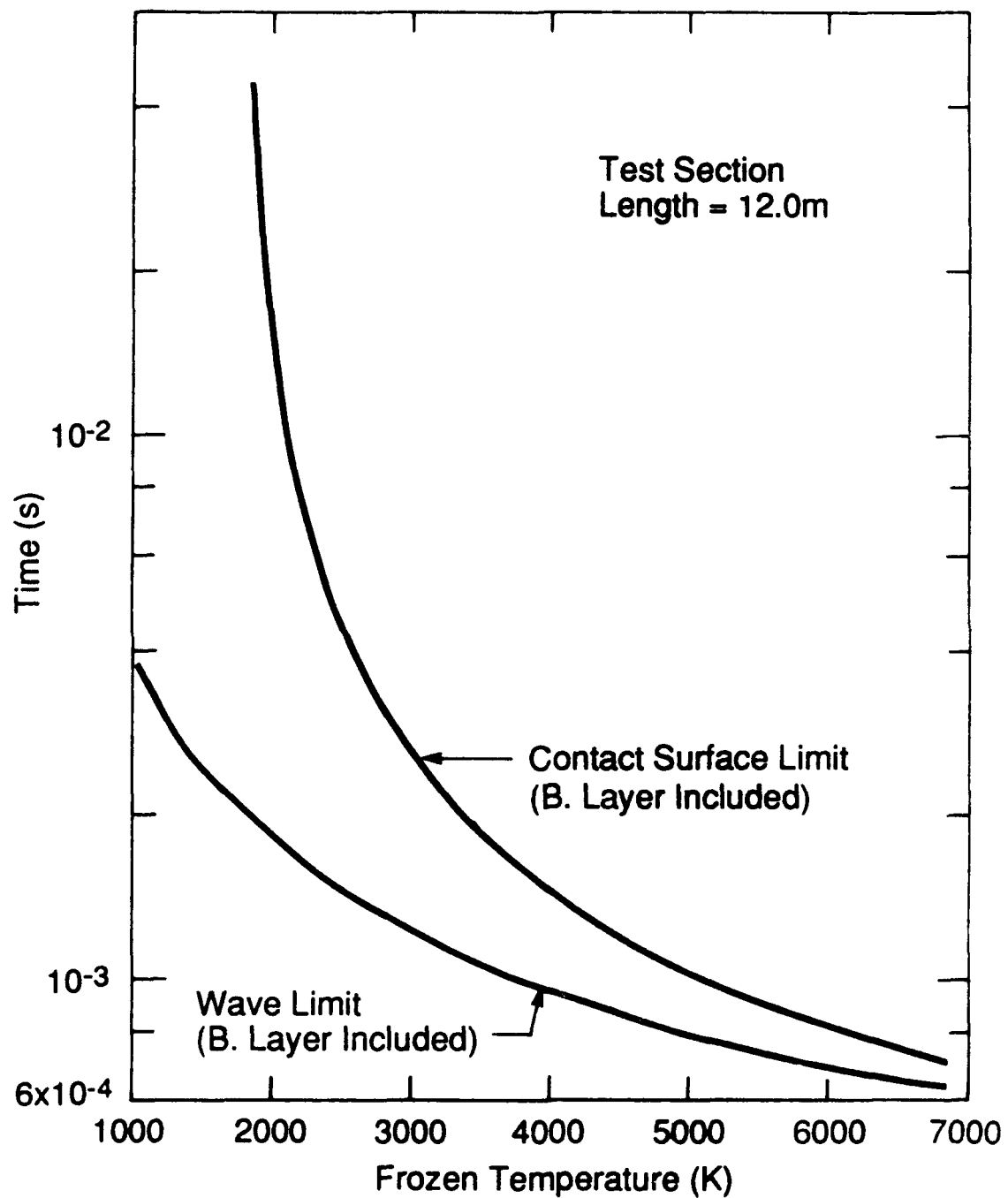


Figure 6

Test Times for a 12.0m Test Section Length

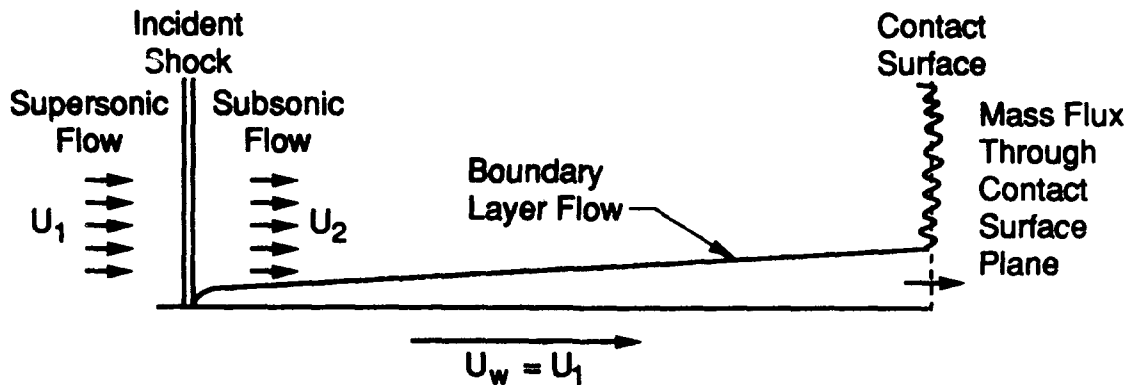


Figure 7

### Boundary Layer Development in the Shock Tube

We have assumed fully turbulent boundary layer flow beginning at the shock front. This will undoubtedly overpredict boundary layer effects since the boundary layer will at first be laminar and then at some distance from the incident shock undergo the transition to a turbulent boundary layer. The boundary layer affects the free stream flow by acting as a sink; the mass and area in the free stream will decrease continuously from the incident shock to the contact surface. The free stream flow will be isentropic between the shock and the contact surface and the variation in flow properties can be followed by assuming that the boundary layer changes the effective flow area of the free stream. The displacement thickness for this particular flow is negative implying that the boundary layer acts as an aerodynamic sink, and the free stream flow is analogous to the decelerating flow in a subsonic diffuser. This analogy is only valid in the incident shock reference frame. For the laboratory reference frame, the flow accelerates between the incident shock and the contact surface. The local area variation can be approximated by Eq. (2) and the flow variables

(pressure, temperature, and velocity) at each axial station can be found using the isentropic channel flow relations.

$$\frac{A_0}{A} = 1 - \left[ \frac{\ell}{\ell_m} \right]^{1-n} \quad (2)$$

where:

- $A_0$  = flow area with no boundary layer  
 $A$  = flow area with boundary layer  
 $\ell/\ell_m$  = ratio of distance from the incident shock to the maximum separation distance.

The variation in flow parameters with distance behind the incident shock also affects the behavior of the reflected shock and therefore the flow properties behind it, as it propagates up the tube. Solution to this part of the problem has been implemented by imposing a reflected shock on the flow at the instant in time when the incident shock meets the end wall. The reflected shock strength is set by the condition that the flow velocity in the laboratory frame behind the reflected shock must be equal to zero. The propagation of the reflected shock through the incident flow and the associated shock strength are uniquely specified by this condition. This model allows calculation of the final length of the high-enthalpy stagnation region in the shock tube as well as providing an estimate of the variation in properties which can be expected in the reflected shock zone.

Our results indicate that the variations in temperature, pressure, and density can easily be greater than 10 percent. This result highlights the necessity for nonintrusive measurements of the flowfield produced by the plenum; clearly idealized calculations of shock tunnel flow conditions will be no more accurate than the 10 percent (or more) variation which our boundary layer model has predicted.

The boundary layer solutions also allow calculations of the total mass in the core flow. This result is an important one for the shock tunnel design; it places an upper bound on the total mass available for exhausting into the shock tunnel. Results from this integration show that over a range of incident shock Mach numbers from 2 to 7, the available high enthalpy mass in a 6 in diameter, 7 m long tube, is 0.01 kg for Argon and 0.009 kg for air. These results vary approximately 10 percent over the range of incident shock Mach numbers.

The major effects of the boundary layer on the properties in the shock tube are therefore:

1. A variation in the properties of the stagnation region as a function of axial position
2. A decrease in the high enthalpy stagnation region length (and therefore the available mass for running the shock tunnel).

The previous discussion has illustrated that in order to maximize the testing time in a shock tunnel, the shock tube test section must be as long as physically possible. In addition, a minimum driver length is required to avoid premature quenching of the reflected shock by the rarefaction wave. The driver length must be long enough to ensure that the rarefaction

wave reaches the test section end wall after the contact surface. Figure 8 presents the results in terms of a ratio of driver length to test length and is based on wave processes in the tube, not including boundary layer effects. Included in these results is the effect of driver gas temperature on the required driver length. The calculated ratio will be conservatively long since boundary layer effects accelerate the contact surface and therefore lower the actual test time. Clearly the lower plenum temperature conditions require significantly longer drivers.

The previous discussion has outlined the important aspects of shock tube flows including the effects of boundary layers. These results were then used, as discussed in the following sections, to aid in the design of the shock tunnel and predict its performance.

### 3.3 Shock Tunnel Design

The previous section discussed the details of shock tube performance which are relevant to shock tunnel design. This section will relate these to the logical design of the shock tunnel. The issues which must be addressed are the relationship of shock tube size and performance to the scale (cross section area and length) of the shock tunnel, the importance of the secondary diaphragm, the pressure capacity for the system, and the nozzle design.

The mass flow rate in the shock tunnel, for a given reflected shock condition, is controlled by the size of the nozzle throat. Since the facility is a Mach 3.0, two-dimensional system, the nozzle throat size uniquely determines the cross sectional area of the tunnel. The performance of the shock tube in terms of the mass and test time available can, therefore, be used to set the scale for the shock tunnel. Test times in the shock tube and flow times in the

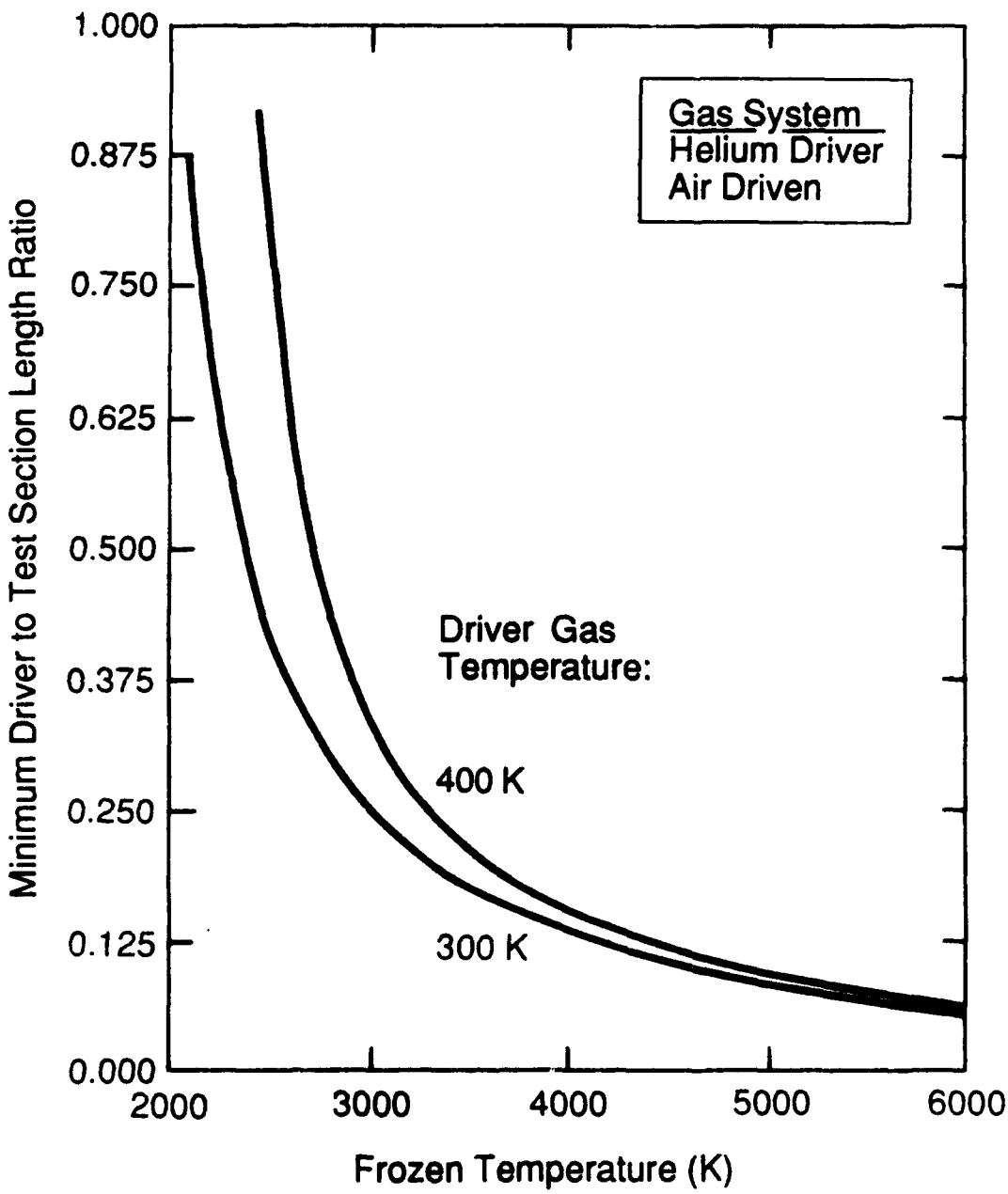


Figure 8.

Required Driver Length as a Function of No-Reaction,  
Reflected Shock Temperatures

shock tunnel are assumed to be approximately equal. The time to exhaust the available mass in the tube through the nozzle throat is given by Eq. (3):

$$\tau_e = \frac{\rho_5 l_5 A_t}{\rho^* V^* A^*} \quad (3)$$

where:

$\rho_5$	-	density in the reflected shock region
$l_5$	-	length of the "plug" of hot gas available to drive the flow
$A_t$	-	area of the shock tube
$\rho^*$	-	density at the nozzle throat
$V^*$	-	velocity at the nozzle throat
$A^*$	-	area of the nozzle throat
$\tau_e$	-	exhaust time.

Results from this equation coupled with realistic predicted test times and heated gas lengths are given in Figure 9. This figure includes results for three test section lengths (5.66, 8.0, and 12.0 m) and illustrates an almost complete independence of nozzle throat area with respect to length. Predicted area ratios (nozzle throat to shock tube cross section) do not include the effect of plug flow velocity on the contact surface speed. As a first estimate of a reasonable operation limit for a shock tunnel, we have taken the conservative view that a factor of two decrease in area ratio should account for nonidealities which we have not included in the performance of the system.

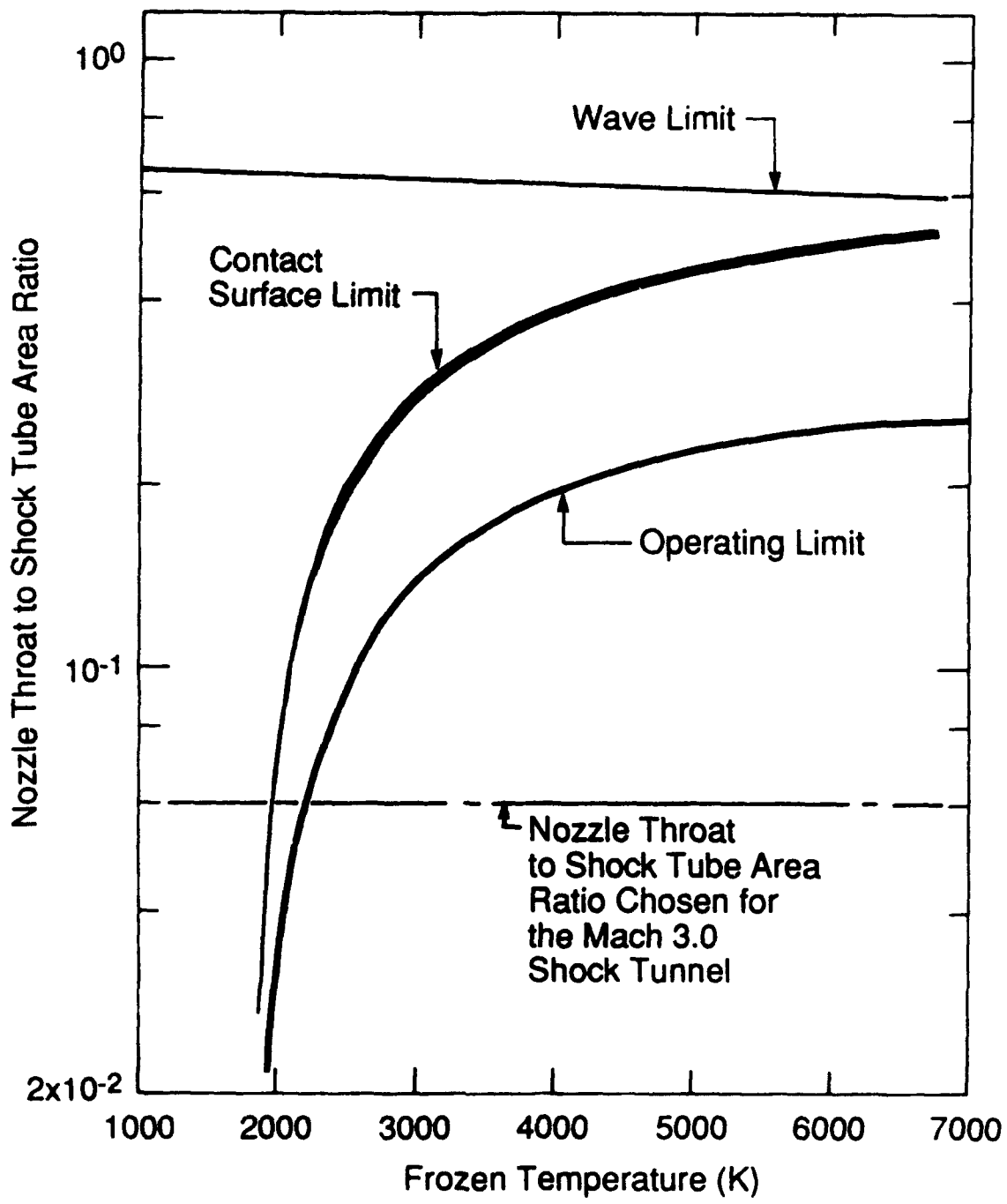


Figure 9.

Relative Nozzle Throat Size for Test Section Lengths 5.55, 8.0, and 12.0m

As shown in Figure 9, a nozzle throat to shock tube area ratio of approximately 0.06 has been chosen for this facility. For plenum conditions of 2300 K and higher the test time in the shock tunnel will not be compromised by the flow rate in the nozzle.

In addition to choosing a cross section area for the tunnel flow system, the overall length must be determined. Since the facility is designed to apply optical diagnostics to chemically reacting flows, the test section must be long enough for significant mixing to occur, and for the implied residence times, for ignition of the fuel and air. Ignition time has been investigated by other workers in a RAMJET environment for H<sub>2</sub>/Air system<sup>5</sup> and the results imply that a 1000 K, Mach 3.0 airstream would require approximately 1m to ignite. Chemical kinetic modeling implies distances significantly less than 1m. Mixing lengths can be crudely estimated from shear layer spreading rates and the results of our Phase I experiments.<sup>6</sup>

If mixing length is defined as the length required for the injectant to spread across the entire height of the test section, then an 8.9 cm wide test section will require between 0.88 and 2.2m to mix. Results from our Phase I experiments indicate a mixing length of 0.88m while shear layer spreading rates at comparable convective Mach numbers imply a 2.2m length. To insure an adequate test section, the tunnel length was chosen to be greater than the longer, or more conservative figure.

To improve startup phenomena in the shock tunnel, and for the case of high Mach number flow systems, a secondary diaphragm is included in the shock tunnel. This diaphragm is

located as shown in Figure 10 and separates the shock tube from the shock tunnel. Therefore, the initial pressures in the shock tube and tunnel do not have to be equal. To insure that the diaphragm opens quickly, it is made from very thin material so that the reflected shock causes a near instantaneous failure.

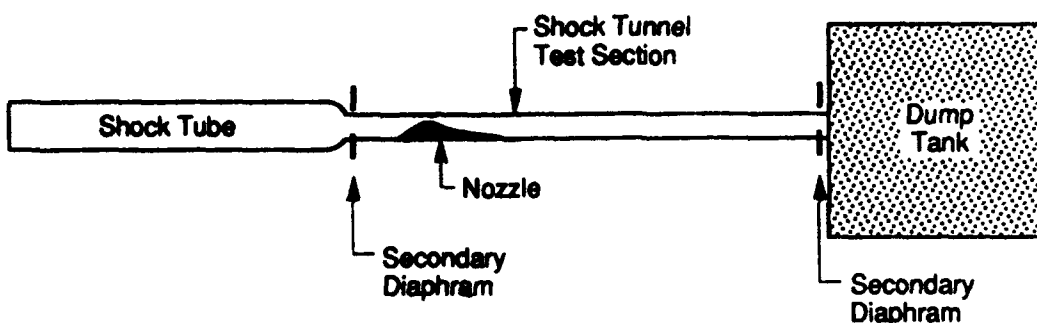


Figure 10  
Secondary Diaphragm Location

The shock tunnel also requires a dump volume to provide a low pressure exhaust environment for the test section and to regulate the late time pressures (cold driver flow) in the nozzle and test section. The size required for the dump tank may be evaluated by examining the mass flow in the shock tunnel nozzle throat, which is fundamentally related to the shock tunnel plenum conditions:

$$\dot{m} = \rho^* A^* u^* \quad (4)$$

$$\frac{\rho^*}{\rho_0} = \left( \frac{1}{1 + \frac{\gamma-1}{2}} \right)^{\left[ \frac{1}{\gamma-1} \right]} \quad (5)$$

$$u^* = \sqrt{\gamma R T^*} \quad (6)$$

$$\frac{T^*}{T_0} = \left( \frac{1}{1 + \frac{\gamma-1}{2}} \right) \quad . \quad (7)$$

The density in the tank is simply controlled by the flow into the tank and the tank volume.

If the flow process is isentropic, pressure and density are related and the tank pressure may be expressed as a function of time (Eq. (8)):

$$\frac{P_{\text{tank}}}{P_0} = \left[ \frac{A^* \Delta t}{V_t} \right]^\gamma \left[ \frac{\rho^*}{\rho_0} \left( \frac{T^*}{T_0} \right)^{1/2} \right]^\gamma [\gamma R T_0]^{\gamma/2} \quad (8)$$

where:

$m$	-	mass flow rate
$\rho$	-	density
$A$	-	flow area
$u$	-	velocity
$\gamma$	-	gas specific heat ratio
$R$	-	real gas constant
$T$	-	temperature
$\Delta t$	-	flow time
$V_t$	-	tank volume
$P$	-	pressure.

#### Subscript

$o$  - total, or plenum properties

#### Superscript

\* - properties at the nozzle throat.

$$\frac{P_{\text{tank}}}{P_0} \leq \frac{P_{\text{tunnel}}}{P_0} \quad (9)$$

$$V_t = A * \frac{\frac{\rho^*}{\rho_c} \left[ \frac{T^*}{T_0} \right]^{1/2}}{\left( \frac{P_{\text{tunnel}}}{P_0} \right)^{1-\gamma}} (\gamma R T_0)^{1/2} \Delta t \quad (10)$$

$$\frac{P_{\text{tunnel}}}{P_0} = \left( 1 + \frac{\gamma-1}{2} M^2 \right)^{-\frac{\gamma}{\gamma-1}} \quad (11)$$

The design condition for the system can be expressed in terms of the back pressure on the nozzle exit flow, Eq. (9). The tank must be sized so that the back pressure on the tunnel never exceeds the pressure in the test section. Fortunately, these quantities are all expressed in terms of property ratios, which greatly simplifies the design task. Table 1 lists appropriate tank volumes for the tunnel, assuming a Mach 3.0 system, throat area of  $0.0015 \text{ m}^2$  ( $0.78 \times 3.00 \text{ in.}$ ), flow times appropriate for a 12m test section, and frozen flow (gas properties  $R$  and  $\gamma$  are set in the plenum and do not evolve).

Clearly, the required tank sizes for this part of the design are relatively modest. Non-isentropic effects which were not considered will in general raise the tank pressure. In addition, we have not considered wave behavior in the tank.

Table 1. Dump Tank Size as a Function of Plenum Temperature

Total Temperature (K)	$\gamma$	$R \frac{m^2}{s^2-K}$	$\frac{\rho^*}{\rho_0}$	$\frac{T^*}{T_0}$	$\frac{P_{tunnel}}{P_0}$	$\Delta t$ (s)	$V_t$ ( $m^3$ )
2500	1.29	288.8	0.627	0.873	0.0243	0.00404	0.06
3000	1.28	289.3	0.626	0.877	0.0241	0.00255	0.044
4000	1.29	293.6	0.627	0.873	0.0243	0.0015	0.029
5000	1.29	302.2	0.627	0.873	0.0243	0.00102	0.03

The second function for the dump system is to control the final pressure in the shock tunnel test section. This is simply effected through the volume available for the redistribution of the driver gas. These "late time" pressures are simply computed by considering a redistribution of the mass that originally resides in the driver section. Assumptions are a 12 m long, 6 in diameter shock tube test section and a 3.7 m long driver filled to 2600 psi. The dump volume required to keep the pressure below 200 psi is approximately  $0.75 m^3$ .

Another factor which must be considered in the shock tunnel design is the pressure which the tunnel flow section could experience due to hydrogen/air combustion. In all scenarios, the most severe pressure rise is due to a detonation of the mixture and there is no means immediately available to insure, with a 100 percent confidence level, that a detonation would at all times be avoidable. Our philosophy was therefore to design the tunnel section for pressures that could be experienced from a detonation. A detonation can be modeled as a shock/combustion phenomenon that is driven through a mixture due to the energy release of

the reactants. Figure 11 illustrates this simple structure. The high pressures which are possible are confined to the region between the shock and the deflagration (commonly known as the von Neumann spike). Detonation velocities are typically on the same order as the flow velocities in the tunnel; we therefore can imagine two scenarios: first, a standing detonation wave in a fully mixed high-speed flow (this is highly unlikely but could occur for a narrow range of operating conditions); and second, a detonation in a hydrogen/air mix before the tunnel starts (due to a mistiming of the hydrogen injection). Pressure increases associated with each of these phenomena are given in Figures 12 and 13.

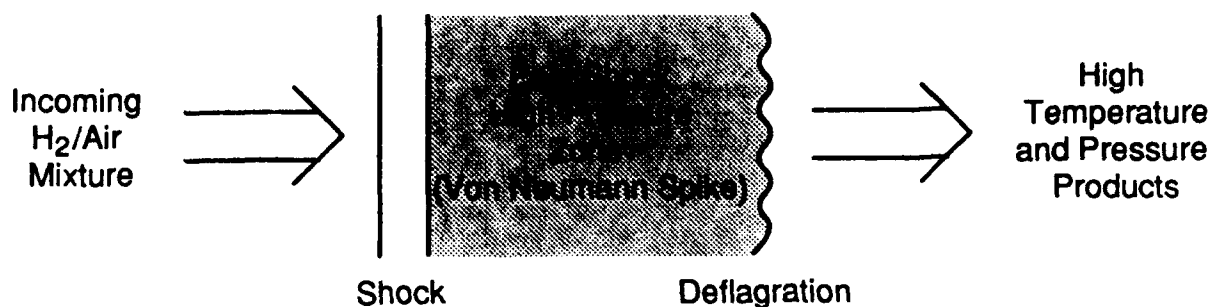


Figure 11  
Conceptual Description of a Detonation Wave

By examining the expected pressure ratio from a detonation in conjunction with maximum pressure values initially in the tunnel and during the tunnel's operation, a design pressure can be defined. This pressure is 25 atm which implies a series of operating maximum pressures as listed in Table 2 and a maximum initial pressure in the tunnel of 0.7 atm.

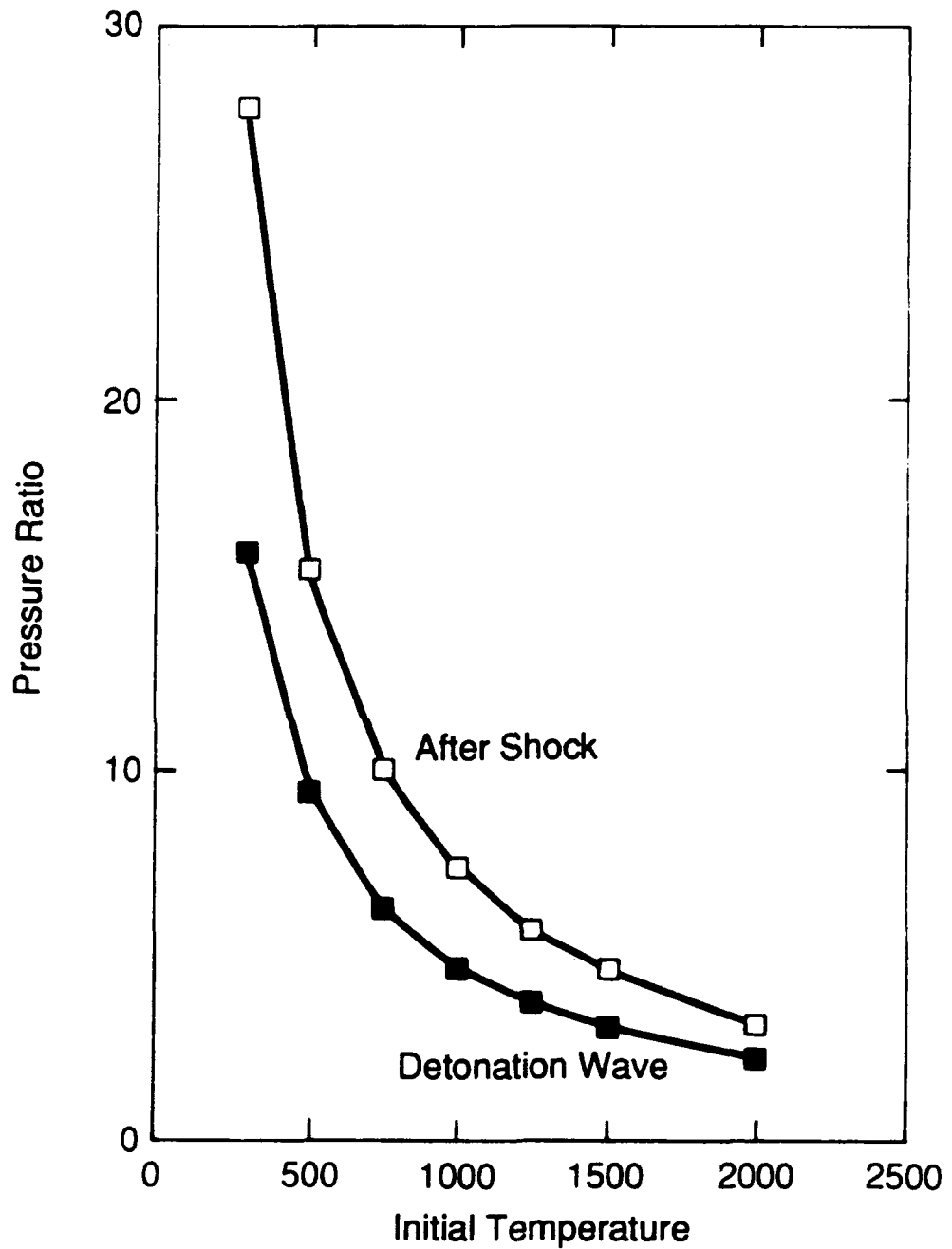


Figure 12

Pressure Ratio for a Stoichiometric  $\text{H}_2/\text{Air}$  Mixture as a Function of Initial Temperature

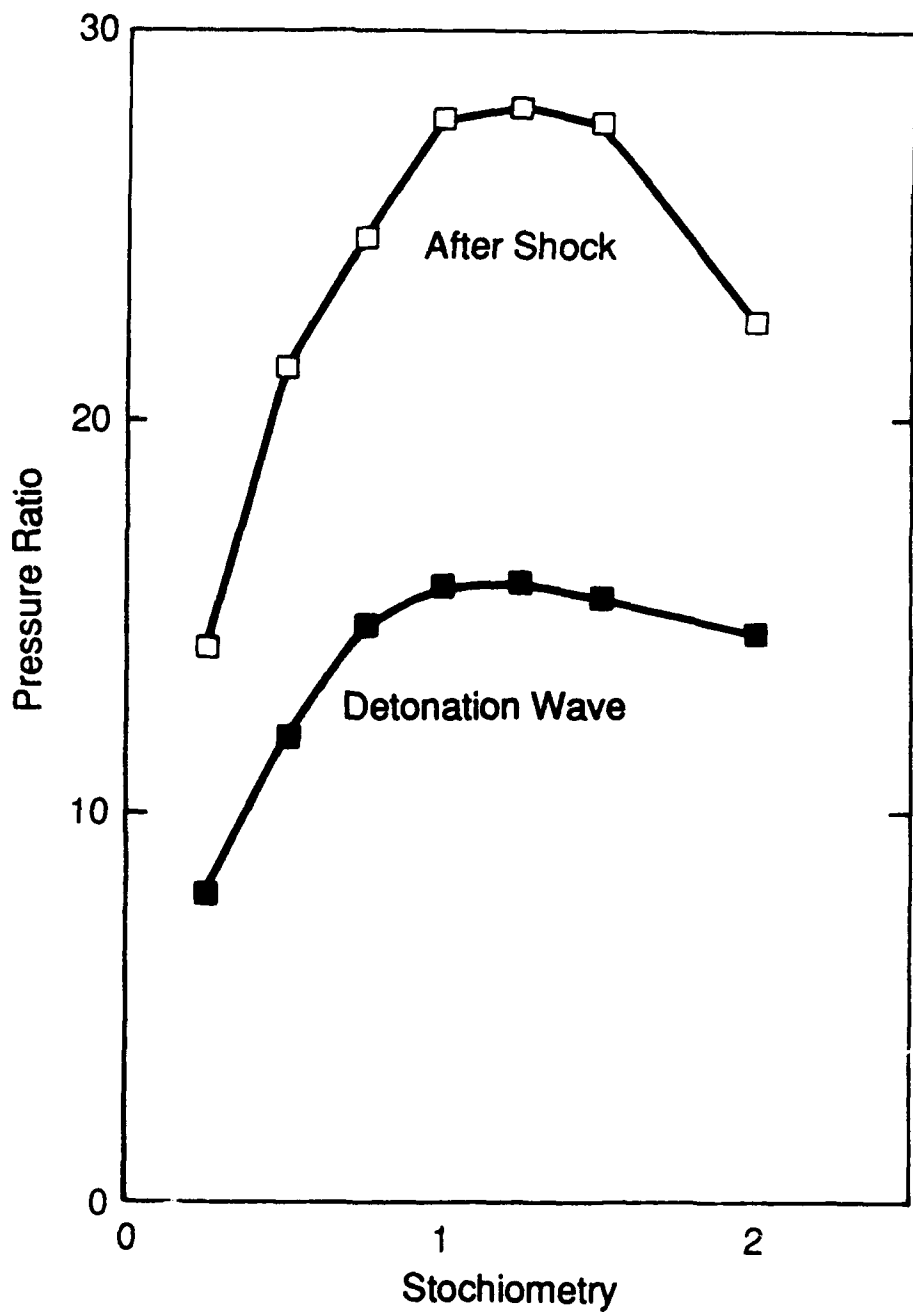


Figure 13

Pressure Ratios for a Room Temperature Mixture as a Function of  
Stoichiometry (less than 1.0 is a fuel-lean mixture)

Table 2. Tunnel Pressures for a Detonation During Operation

Flow Temperature (K)	Maximum Allowable Tunnel Pressure (atm)	Detonation Pressure Ratio
750	2.5	10.0
1000	3.38	7.39
1250	4.35	5.75
1500	5.41	4.61

The previous discussion allows us to set pressure capacities for the system. The driver system must be capable of routinely handling 2600 psig (the maximum pressure from a standard helium cylinder). The reflected shock test section which was used for the tunnel can withstand 120 atm (~ 1800 psig). The shock tunnel pressure capacity is driven by the possibility of H<sub>2</sub>/air detonation.

Finally, the nozzle must be designed for the shock tunnel. The nozzle itself is designed using the method of characteristics with rounded throat. A rounded throat design sets a radius of curvature for the throat (typically equal to twice the nozzle throat height) and solves for the shape of the sonic line in the throat region. The sonic line is then used as the initial condition for the method of characteristics design. A rounded throat design is superior to a sharp throat design for two reasons. The throat region is less susceptible to boundary layer effects, and the nozzle design is based on an accurate initial condition for the expansion contour.

The nozzle design for this system was performed by Prof. Joe Huffman, Purdue University for a nozzle throat height of 1.55 cm. However in order to define the nozzle the specific heat ratio and gas constant for the gas must be determined. For the operating temperatures in the shock tunnel, these values are 1.32 and  $209.9 \text{ m}^2/\text{s}^2\text{-K}$ , respectively.

This section has described the theoretical aspects of the shock tunnel design. With the exception of chemistry effects, Subsections 3.2 and 3.3 have described the theoretical aspects of the shock tunnel design.

### 3.4 Chemistry Effects on Shock Tunnel Design and Performance

The previous sections have described the important aspects of the shock tunnel design from a fluid mechanics viewpoint. However, since air is the gas which will be used in the tunnel, chemical reactions in the reflected shock zone and nozzle can play a significant role in the flow conditions which are produced. This section will first describe the chemical reaction effects on the conditions in the reflected shock plenum, then will address the chemical reaction as the flow progresses through the nozzle, and finally will examine the degree of vibrational equilibrium which is achieved at the nozzle exit.

Chemical reactions in the plenum can significantly reduce the system temperature simply due to the production of NO, and the dissociation of N<sub>2</sub> and O<sub>2</sub> into N and O atoms. We have modeled this process using a standard chemical kinetics package<sup>7</sup>. Figure 14 illustrates the effect of chemistry on the temperature in the reflected shock zone. Clearly, as the frozen temperature increases, the effects of chemical reactions become more and more

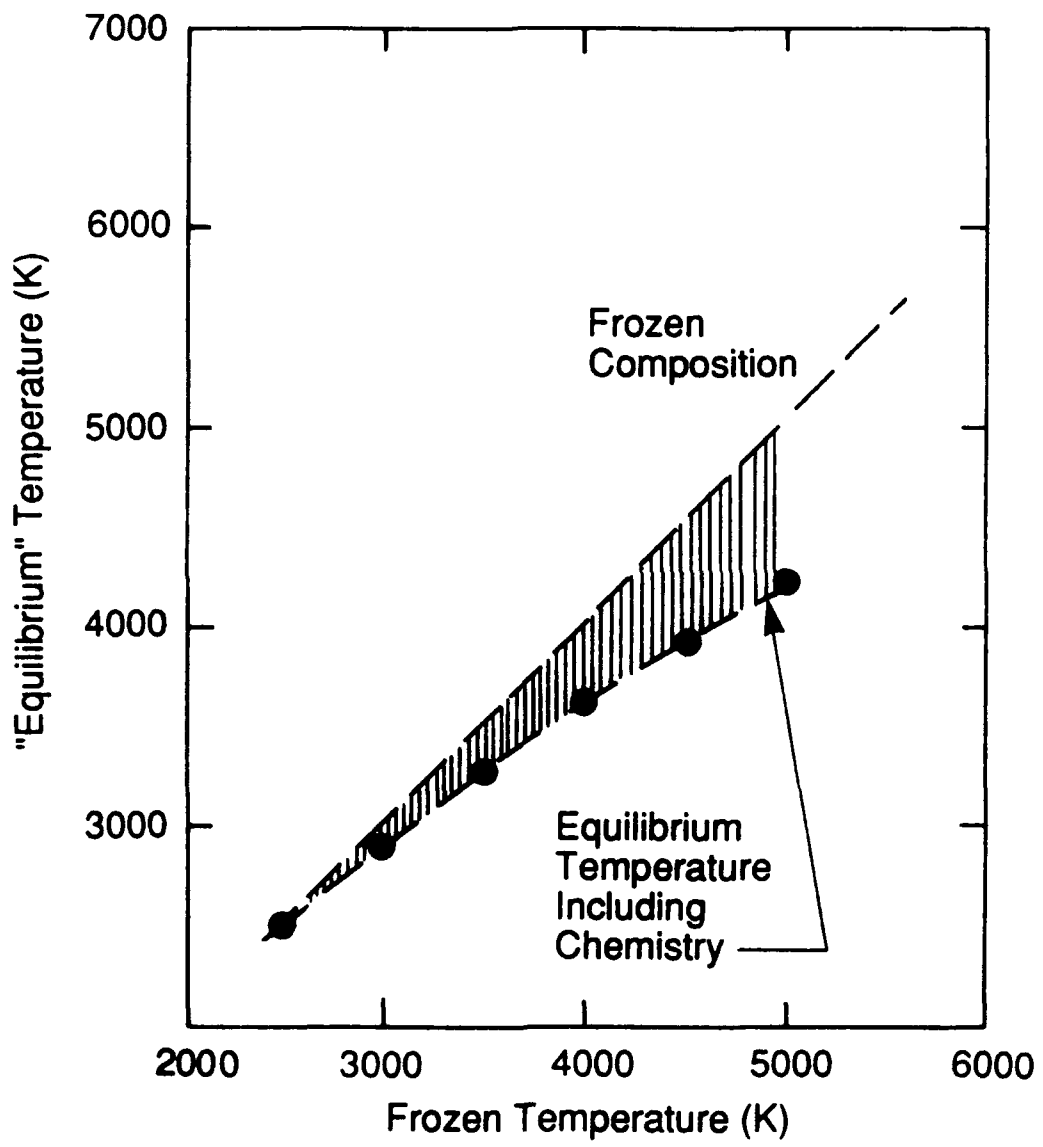


Figure 14  
Chemistry Effects on the Reflected Shock Zone Temperature

important; for a frozen temperature of 5000 K the temperature drop due to the formation of species from N<sub>2</sub> and O<sub>2</sub> is approximately 15 percent. The time scales associated with the change from an initial temperature to the "equilibrium" temperature also change with the reflected shock conditions. The period required for 85 percent of the temperature drop to occur, for a 50 atm system, is 1.2 ms at 2500 K, 0.18 ms at 3000 K, and less than 50  $\mu$ s for temperatures of 3500 K and above.

A second issue of distinct importance to the shock tunnel development is the possibility of significant chemical reaction in the cooling and expanding portion of the nozzle. We have examined this problem using a chemical kinetics code (developed by PSI) that tracks the chemical composition as a function of distance in a stream tube of specified geometry. Results from this exercise are shown in Table 3 which lists the change in concentration of NO, N, and O from nozzle entrance (at equilibrium concentrations) to exit. The concentration of NO is relatively stable while the concentration of N and O atoms are significantly depleted in the flow time in the nozzle. The insensitivity of NO concentration, once it is established, to the temperatures imposed by the flow is exceptionally important from a diagnostic point of view. NO is present in sufficient essentially nonvariant concentration that it may be used as a chemically generated molecular seed in the flow. For regions before the injection zone where NO mole fraction is constant, diagnostic strategies can be used to derive temperature information about the flow. The variation of mole fraction in the injectant region and downstream regions will provide insight into the mixing process.

Table 3. Changes Due to Chemical Reactions in a Mach 3.0 Nozzle

Plenum Temperature (K)	Species*		
	NO (%)	N (%)	O (%)
2500	-0.26	-100	-26
3000	-2.7	-100	-40.6
3500	-10.0	-100	-57

\*Change in species from plenum to nozzle exit

In addition to chemical kinetic effects, the degree of vibrational equilibrium in the shock tunnel nozzle is important since one of the diagnostic methods for this work was to monitor the vibrational temperature of NO in the shock tunnel as a means of tracking the flow temperature. The chemical kinetic stream tube code described above includes the kinetics of this process and uses relaxation rates as summarized in the literature.<sup>8</sup> Results from this calculation are shown in Figure 15. Highlighted on this plot is the deviation of the vibrational temperature of NO from the kinetic temperature. Very low pressure systems, as expected, will have a significant disagreement between these two temperatures. However, even for relatively modest plenum pressures, such as 10 atm, the agreement between vibrational temperature and kinetic temperature is better than 20 percent. For high pressure systems (30 atm and more) the inaccuracy due to vibrational nonequilibrium becomes relatively insignificant (less than 5 percent).

To conclude this section on the effects of chemistry on shock tube performance, an examination of kinetic behavior in the shock tunnel has shown that chemistry can play a significant role in determining the shock tunnel performance. Reactions in the reflected

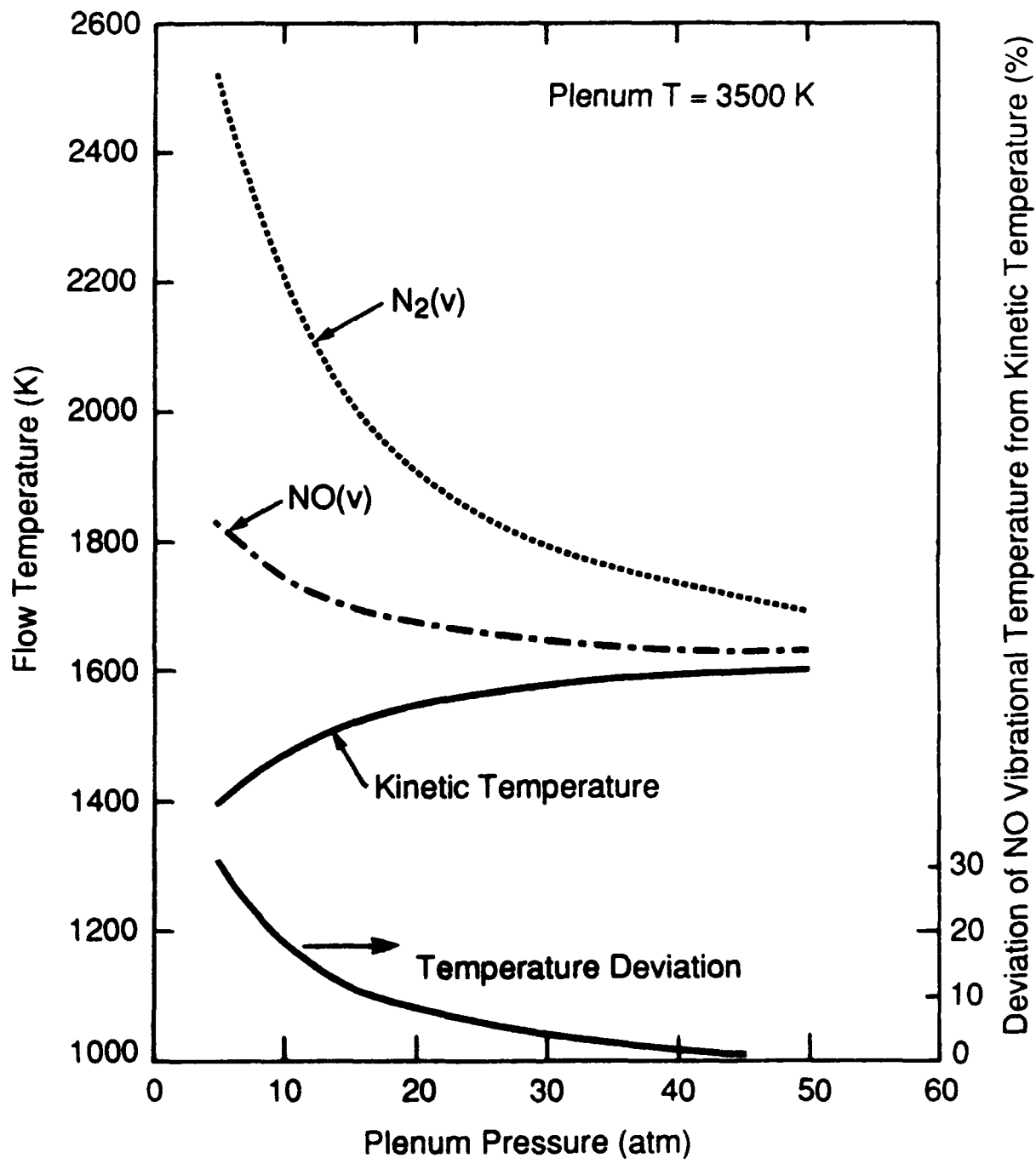


Figure 15  
Vibrational Nonequilibrium in Mach 3 Air

shock zone can significantly depress the system temperature and additionally produce a significant quantity of NO. Reactions in the nozzle, as the gas cools and accelerates, consume a significant amount of the atomic species (N and O) but leave the concentration of NO relatively unchanged. Finally the vibrational temperature of NO can be significantly different compared to the kinetic temperature for low pressures but this effect loses its significance for higher pressure systems.

### 3.5 Shock Tunnel Hardware Description

The previous discussion has centered on the theoretical aspects of the shock tunnel design. This section will concisely describe the hardware which comprises the shock tunnel.

Figure 16 and Table 4 describe the major components of the shock tunnel facility. The shock tube driver consists of a 16 cm I.D., 20.3 cm O.D., 3.6 m long 4140 steel tube fitted with an end cap/fill hose assembly on one end and threaded to accept a connection flange on the other end. The system is designed to routinely withstand pressures of 3500 psi. A vacuum and driver gas supply system are connected to the driver for evacuation and gas fill

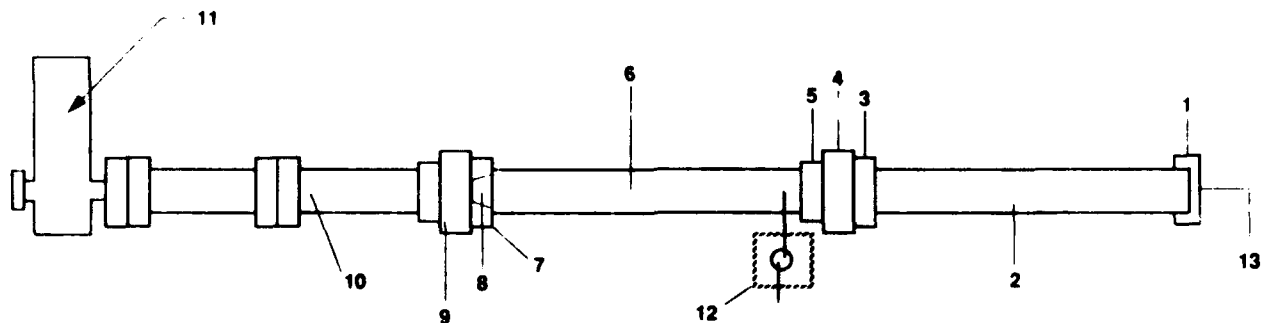


Figure 16  
Schematic Diagram of Shock Tunnel Facility

**Table 4. Shock Tunnel Major Components List**

Part Number	Description
1	Driver end cap
2	Shock tube driver, 3.6m long
3	Driver end flange
4	Double diaphragm assembly
5	Flange stiffener, test section assembly
6	Shock tube test section, 13.9m long
7	Test section end flange
8	Transition section, 6-3/8 diameter to 3 x 3.5 in. rectangle
9	High pressure piece
10	Tunnel section assembly
11	Dump tank, 240 gal, 200 psi working pressure
12	Vacuum system, $10^{-6}$ torr
13	Vacuum system, $10^{-3}$ torr adapted for dual diaphragm station

purposes. The diaphragm station for the shock tube is a dual diaphragm type system which uses 8.5 in square diaphragms that are prepared by mechanically scoring an x to enhance petal formation and retention. The driven section of the shock tube consists of six sections of stainless steel tubing with a total length of 13.9 m (tube I.D. and O.D. are 19 and 16.3 cm).

This section of the tube is equipped with a high quality vacuum system capable of  $10^{-6}$  torr operation and an accurate gas filling system. The transition between the shock tube and shock tunnel consists of a series of three flanges and an internal transition section and nozzle. The shock tube is a 16.2 cm diameter system while the basic tunnel flow section is a 7.62 cm wide by 8.9 cm high rectangle. The transition section is a 3.8 cm long circular disc

which can be inserted into the end of the tube and changes smoothly from a 11.5 cm internal diameter to a section that matches the tunnel flow section. The secondary diaphragm is held with four dowel pins on the tunnel side of this transition section. A 16.1 cm thick, 40 cm diameter steel section with a 7.6 x 8.9 cm rectangular cutout separates the shock tube from the tunnel. The single reason for this piece is to reduce the internal pressure requirements on the first tunnel section. The nozzle block is held in the first tunnel section but the initial nozzle ramp and the near throat regions are actually within the large metal block. This piece therefore effectively reduces the pressure entering the tunnel flow section simply due to fluid mechanics associated with nozzle.

The shock tunnel flow section bolts to the previously described large metal block. As previously mentioned the internal cross section of the tunnel flow section is 7.62 cm wide by 8.9 cm high. An interchangeable mach 3.0 nozzle block is held in place with four bolts and was manufactured from 302 stainless steel. The shock tunnel itself is made from 304 stainless steel with approximate wall thickness of 1.0 in. It consists of two sections totaling 2.4 m in length and held together with 28 cm diameter, 3.8 cm thick flanges. The tunnel was manufactured to produce as few flow non-idealities as possible. The sections were vacuum brazed together using annealed, blanchard ground plate. The result is a sharp cornered internal rectangle with high dimensional accuracy. A sample section of the 304 stainless steel braze joint was destructively tested to verify its strength which was found to be much more than adequate (calculated internal pressure required to produce a failure at the joint was in excess of 400 atm). The shock tunnel includes both wall-mounted pressure taps and flush mounted optical window ports. Four of the nine total pressure taps are located in the nozzle

expansion region and can be used to verify proper performance of the nozzle. The remainder of the pressure tap locations are located in the region immediately surrounding the injection/combustion region and at subsequent downstream locations. Five axially located optical access stations are included in the shock tunnel and all locations provide access in two orthogonal directions so that line-of-sight and spatially resolved measurements can be made. The first optical port is immediately after the full expansion point for the nozzle and includes three 4.45 cm maximum clear aperture windows. The second and third optical access ports are shown schematically in Figure 17. The region immediately after the rearward facing step includes two side windows that give full height optical access for a 14 cm flow length. Complementary top windows in this region can be used for laser access. The next three

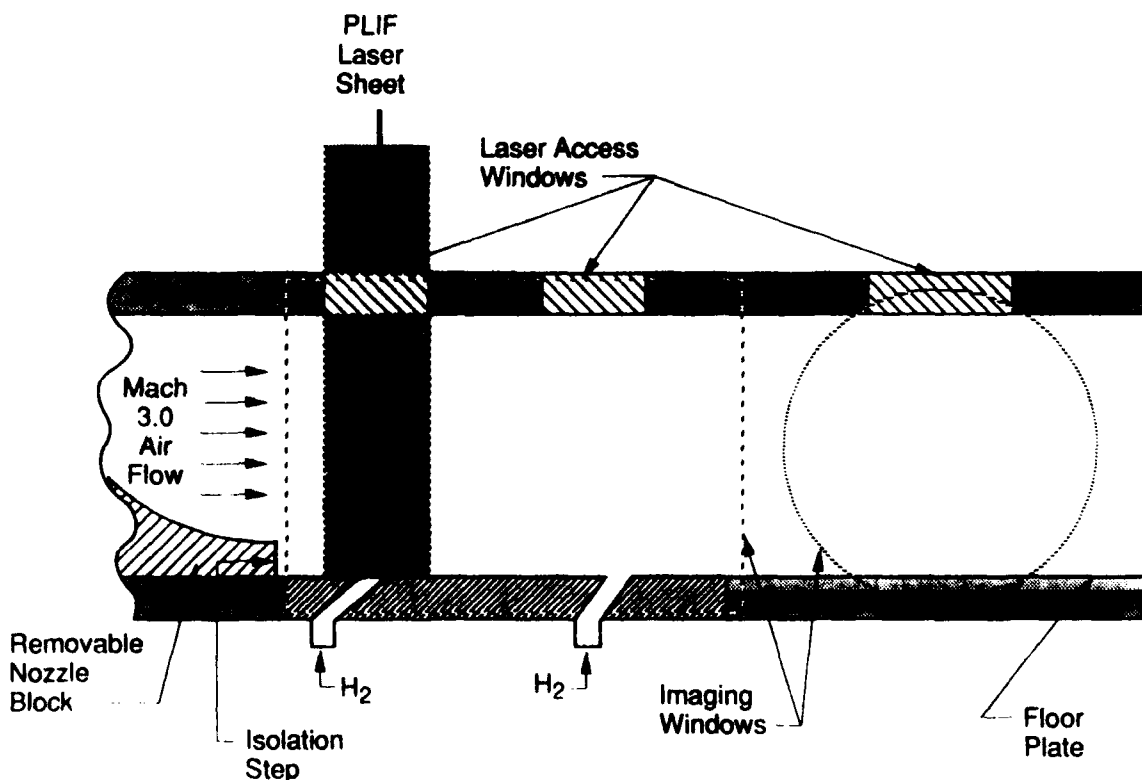


Figure 17  
Optical Access in the Shock Tunnel

optical stations are located 29, 125, and 1835 cm from the rearward facing step and consist of 10.2 cm diameter ports on the sides complemented by top and bottom 5.1 cm diameter ports.

The shock tunnel includes provisions for hydrogen injection so that reacting flows may be studied. As shown in Figure 17, an interchangeable injector block is included immediately after the rearward facing step (1.27 cm high) produced by the end of the Mach 3.0 nozzle. The interchangeable injector block can be used to test a variety of injector configurations.

Following the shock tunnel flow section is a dump tank with vacuum system. This tank is a 240 gal vertical compressed air tank (200 psi working pressure) modified to bolt to the shock tunnel using a 6-in. diameter pipe. The entire dump tank and shock tunnel assembly ride on rollers to facilitate changing the secondary diagram.

The pressure capacities for each of the shock tunnel assemblies were carefully determined and the actual parts were hydrostatically tested to a pressure 50 percent above the working pressure for that section of the system. These test pressures are summarized in Table 5.

Table 5. Hydrostatic Test Pressures

Driver	3900 psi
Shock tube low pressure sections	1100 psi
Shock tube end test section	4500 psi
Shock tunnel sections	750 psi

### 3.6 Shock Tunnel Injection System

To produce reacting flows similar to those in a scramjet, hydrogen must be injected into the shock tunnel flow. The requirements for this are pulsed operation with a fast response time, near constant injection flow rates during the shock tunnel run time, and a failsafe method of limiting the quantity of hydrogen injected into the system. We have addressed these requirements using a 1 gal, 3000 psi rated bladder accumulator with a custom manufactured, explosive burst diaphragm and manifold system. The system is shown schematically in Figure 18. A dual diaphragm system separates the nitrogen pressurized hydrogen from the delivery system for the injector block. Injection is possible on demand by simply igniting the hydrogen/oxygen mixture with the spark plug. Testing of this system revealed that initiation times of  $800 \mu\text{s}$  were routinely produced. The injection system can therefore be triggered using one of the pressure transducer signals from the shock tube.

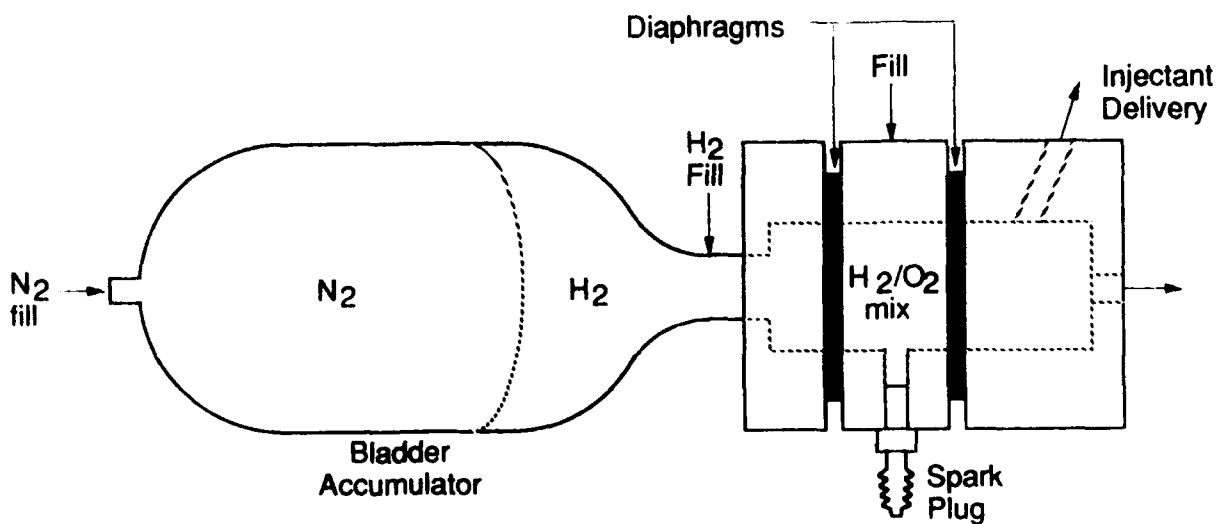


Figure 18

Hydrogen Injector for Shock Tunnel Experiments

The performance of the injection system is directly relevant to the combustion performance in the shock tunnel. To characterize this system the overall stoichiometry for the system can be calculated in addition to the momentum flux ratios. The specific geometry of the injectors in the combustion zone will also be described for the test series in this report.

The overall stoichiometry for the combusting system can be easily described since the injectors in the combustion zone are configured to produce sonic flow at their exit. Using standard gasdynamic relationships, the product of injection pressure and injector exit hole area can be shown to be a function of system stoichiometry and reflected shock temperatures and pressures, Eq. (12):

$$P_{o,H_2} A_{inj} = \phi \frac{P_5}{\sqrt{T_5}} K_1 \quad (12)$$

where

$P_{o,H_2}$	-	stagnation injection pressure
$A_{inj}$	-	injector outlet area
$\phi$	-	equivalence ratio
$P_5, T_5$	-	reflected shock plenum pressure and temperature
$K_1$	-	system constant, $2.12 \times 10^{-3} \text{ m}^2\text{-K}^{1/2}$ .

For a given flow condition and injector area, the stoichiometry is linearly related to the injection pressure. The expected penetration of the injectant plume is also a variable of interest. Injection penetration has been previously studied for cross flows with the injector

oriented at 60 to 120 degree angles with respect to the mainstream flow direction.<sup>9</sup>

Equation (13) summarizes this correlation in terms of the injection pressure and the pressure in the reflected shock zone. Injection systems are also categorized by the momentum flux ratio of the injectant to the free stream. For this system, the perpendicular fraction of momentum with respect to the free stream was used and this relationship can be calculated using Eq (14):

$$\frac{H}{D} = \frac{K_2}{1 + \cos \alpha} \sqrt{\frac{K_3 \rho_{0,H_2}}{P_5}} \quad (13)$$

where:

- $K_2, K_3$  - system constants (1.05 and 2.53 respectively)
- $H$  - penetration height, defined as distance to midpoint in barrel shock
- $D$  - injector orifice diameter
- $\alpha$  - injector orientation with respect to the main stream.

$$q = \frac{\gamma_i}{\gamma_{air}} \frac{1}{M_{air}^2} \frac{P_{0,H_2}}{P_5} 21.1 \sin \alpha \quad (14)$$

where:

- $q$  - momentum flux ratio, injectant to free stream
- $M_{air}$  - Mach number for the free stream.

For the specific injector configuration used in this work, the injection parameters may all be quantified. The injector ports were located in the tunnel flow floor after the rearward facing step along the tunnel centerline at 2.3 and 8.4 step heights downstream and are directed at 30 and 60 degree angles with respect to the tunnel flow. Both holes were 0.48 cm in diameter. Injectant pressure was in all cases 300 psi and the resulting stoichiometry is shown in Figure 19. The expected penetration height for the barrel shock was 0.60 cm above the tunnel floor and the momentum flux ratio for all of the mixing and combustion and combustion tests was approximately 2.0 with a helium injectant and 1.6 for a hydrogen injectant.

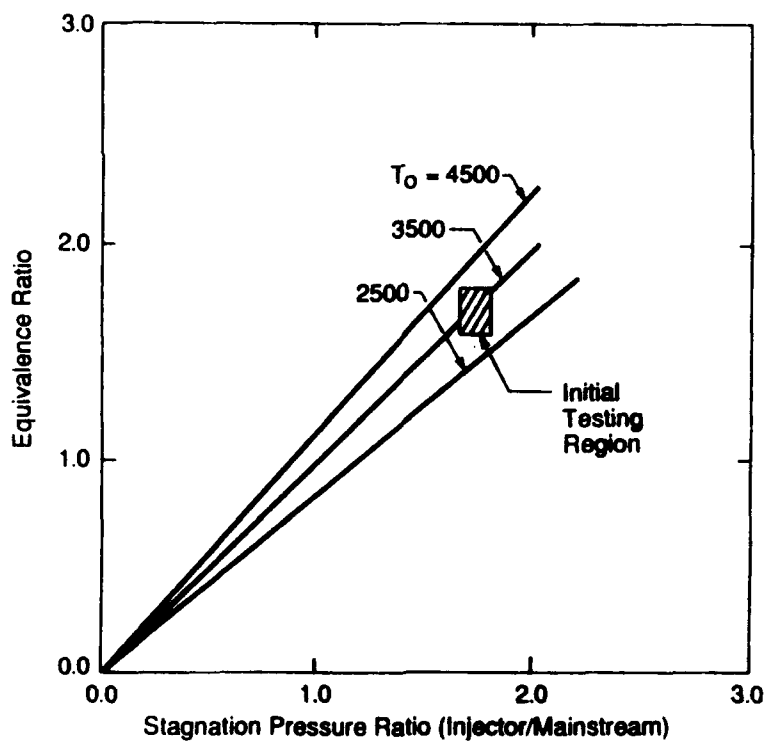


Figure 19

Fuel-to-Air Ratio for Initial Shock Tunnel Tests

### **3.7 Shock Tunnel System Performance**

The previous sections have described both the design of the shock tunnel and the hardware which comprises the system. The actual performance for the shock tunnel, in terms of test times available, static and stagnation temperatures and pressures that can be achieved, and simulation capability for high speed flight, is documented in this section.

A critical performance parameter for impulse facilities, such as this shock tunnel, is the time duration of the high enthalpy flow which is produced. Figure 20 illustrates the observed test times in the shock tunnel as function of static temperature in the Mach 3.0 flow. Test times are determined by monitoring the NO emission at  $5.2 \mu\text{m}$  as described in Subsection 4.4 in this report. Predicted test times from the model described in Subsection 3.2 are also included in this figure and the agreement between predicted and observed values is excellent.

The range of static temperatures and pressures which can be achieved in the tunnel is illustrated in Figure 21. Since the relationship between static and stagnation temperatures and pressures for Mach 3.0 flow is a simple multiplicative factor, a second set of axes is included which describe the range of stagnation conditions which can be produced. As expected, the maximum pressure drops as the flow temperature increases. This is simply explained by noting that the temperature in the shock tunnel is controlled by the driver to driven pressure ratio in the shock tube. Since the driver pressure cannot exceed 2600 psi, the initial pressure in the driven tube and therefore the pressure produced by the reflected shock is reduced for higher temperature conditions.

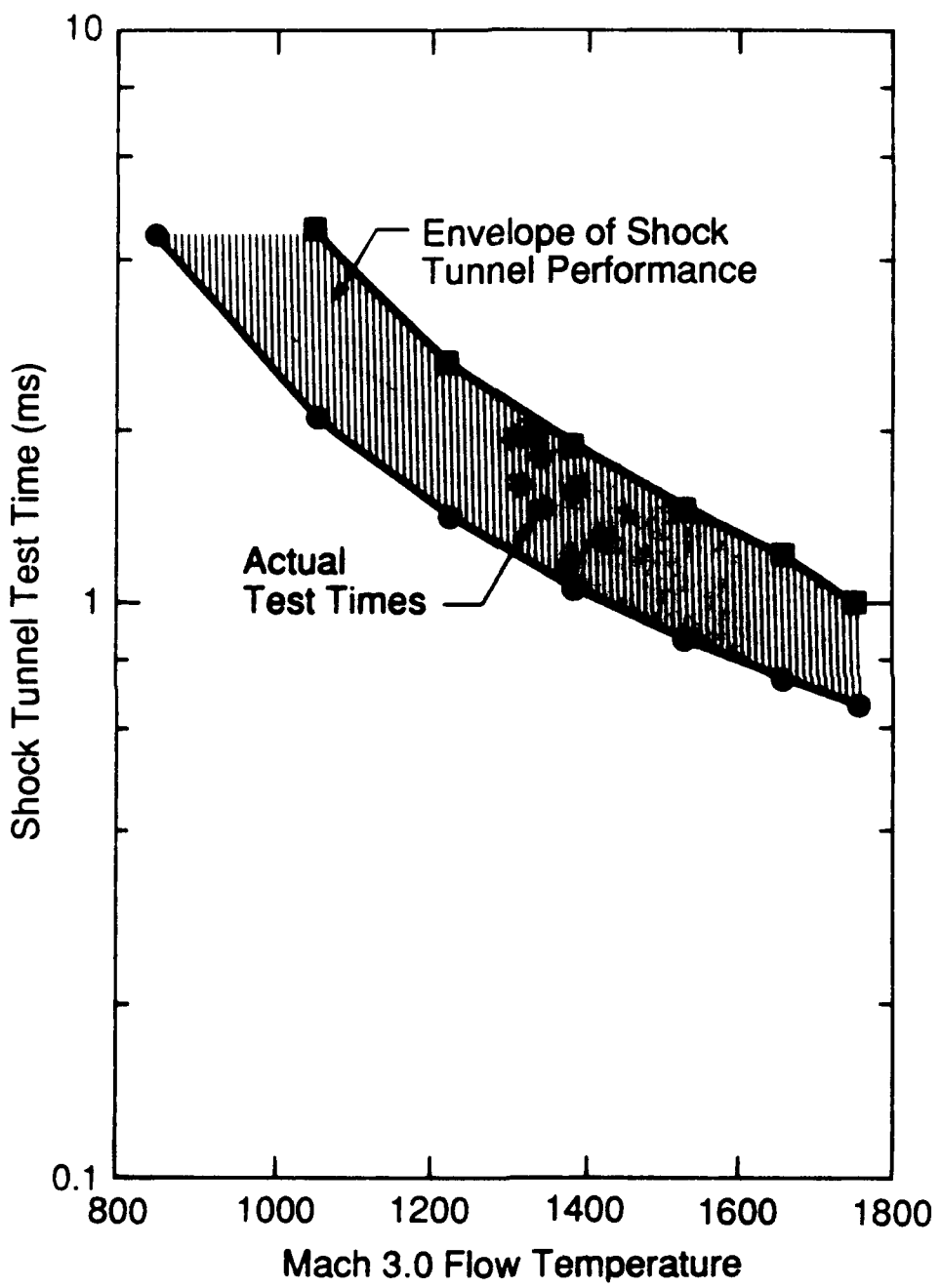


Figure 20  
Shock Tunnel Test Times Compared with Modeling Results

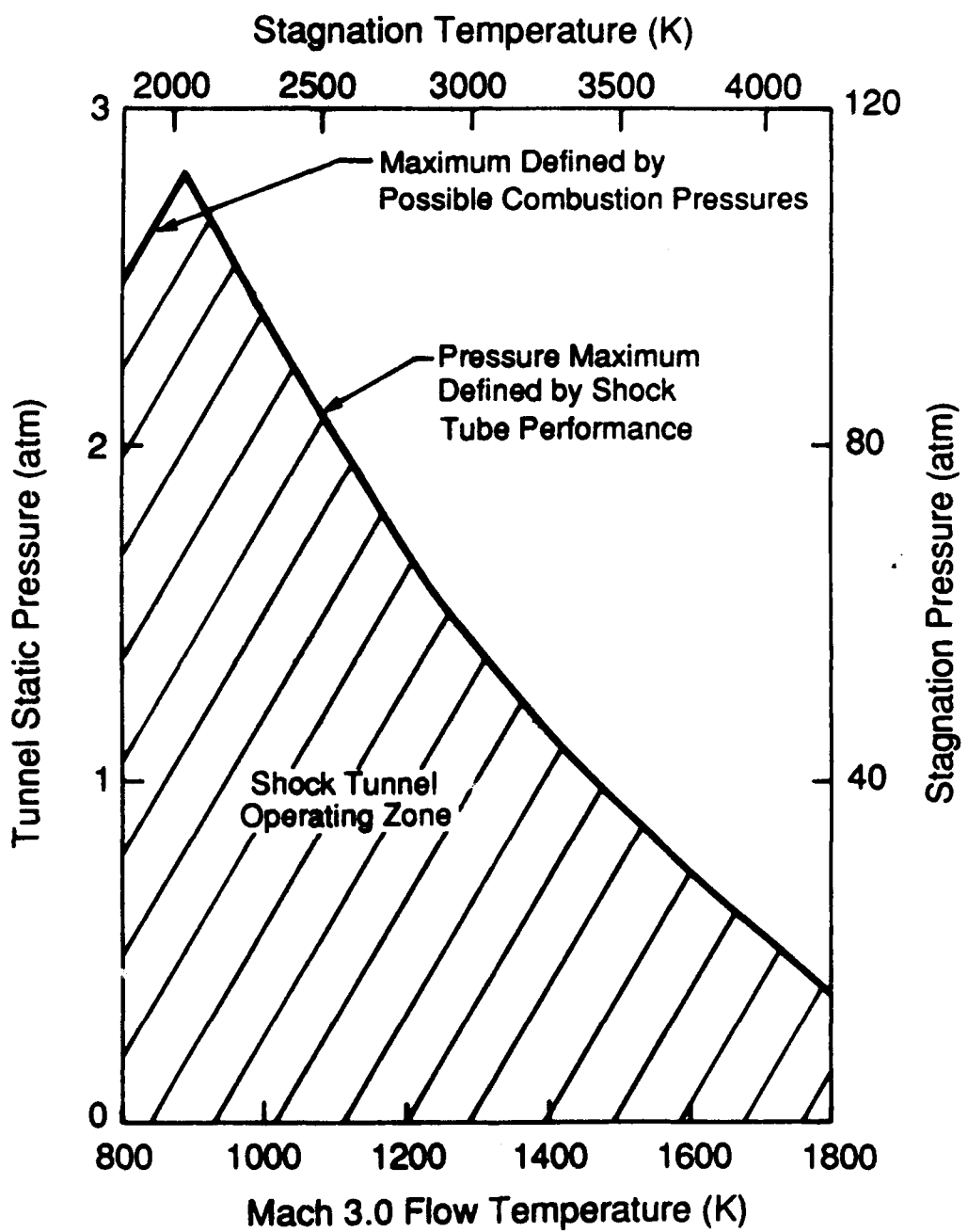


Figure 21

Shock Tunnel Operating Pressures and Temperatures

Figure 22 illustrates the flight simulation capabilities for the shock tunnel compared to a proposed NASP flight corridor adopted from Billig.<sup>10</sup> Clearly the shock tunnel is capable of simulating flight speeds below 3 km/s in the lower pressure regions of the flight corridor. Also included in this figure is the initial testing region used to verify the optical diagnostics described in Subsection 4.3 to 4.6. In terms of the Reynolds number for the flows in the tunnel a maximum value of  $6 \times 10^7/m$  can be produced for static temperatures of 800 K and  $9 \times 10^6/m$  for static temperatures of 1500 K. Lower Reynolds numbers may be produced by simply operating the tunnel at lower pressures.

The previous paragraphs have discussed the operating conditions for the tunnel assuming that the supersonic nozzle performs in a constant manner (i.e., produces Mach 3.0 flow). In addition to schlieren measurements which indicate a Mach 3.0 free stream, the pressure measurements in the nozzle confirm the production of a Mach 3.0 flow.

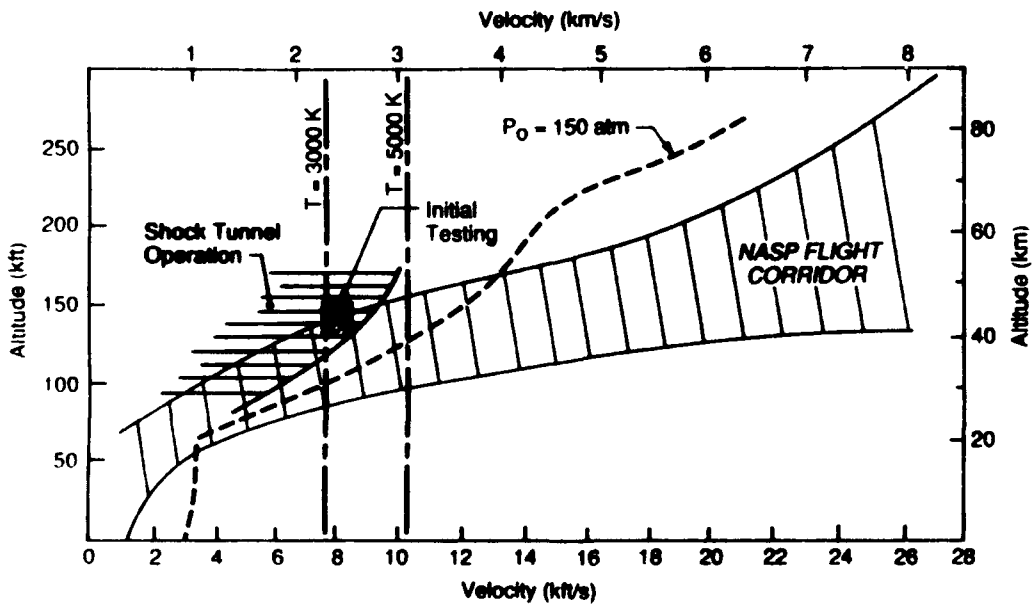


Figure 22

Shock Tunnel Operating Envelope Compared to the NASP Flight Corridor

This section has described the performance for the shock tunnel which was developed as a part of this work. The tunnel is capable of producing flows very relevant to high speed flight (up to 3 km/s) and in addition is very versatile in term of the range of conditions which can be created. This capability, in conjunction with the injection system for creating mixing/reacting flows and the large optical access, make this facility ideal for studying high enthalpy combustion systems for high speed flight.

## 4. OPTICAL DIAGNOSTIC METHODS AND RESULTS

### 4.1 Introduction

A major thrust for this work was to demonstrate a series of optical measurements in mixing and/or reacting high enthalpy flows. These measurements are described in this section. As a means of interpreting/understanding these results, Section 4.2 describes the flow field over the rearward facing step which is produced with and without injection. Section 4.3 describes the results of Schlieren photography for this system. The next section, 4.4, describes infrared emission measurements of the fundamental band of NO which are calibrated to monitor both number density and temperature. Following this section is a description of OH absorption measurements and a measurement strategy for monitoring the number density and temperature of OH. Finally, Section 4.6 presents and discusses Planar Laser Induced Fluorescence (PLIF) imaging measurements of NO and OH in the flowfield.

### 4.2 Flowfield Predictions

Both the Schlieren and PLIF measurements create images of certain properties in the flowfield and it is instructive to compare these images with analytical predictions of the major features of the flow. Figure 23 illustrates the expected flow over the rearward facing step. Certain aerodynamic features of the flow are immediately apparent. The interaction of the supersonic flow with the step creates an expansion fan that begins at the step corner with a leading edge oriented with a 19.5 deg angle ( $\sin^{-1} 1/M$ ) to the flow. The expansion fan extends from this beginning ray to a uniform flow region starting 23 degrees below the horizontal. On the other edge of the uniform flow region is a recirculation zone whose

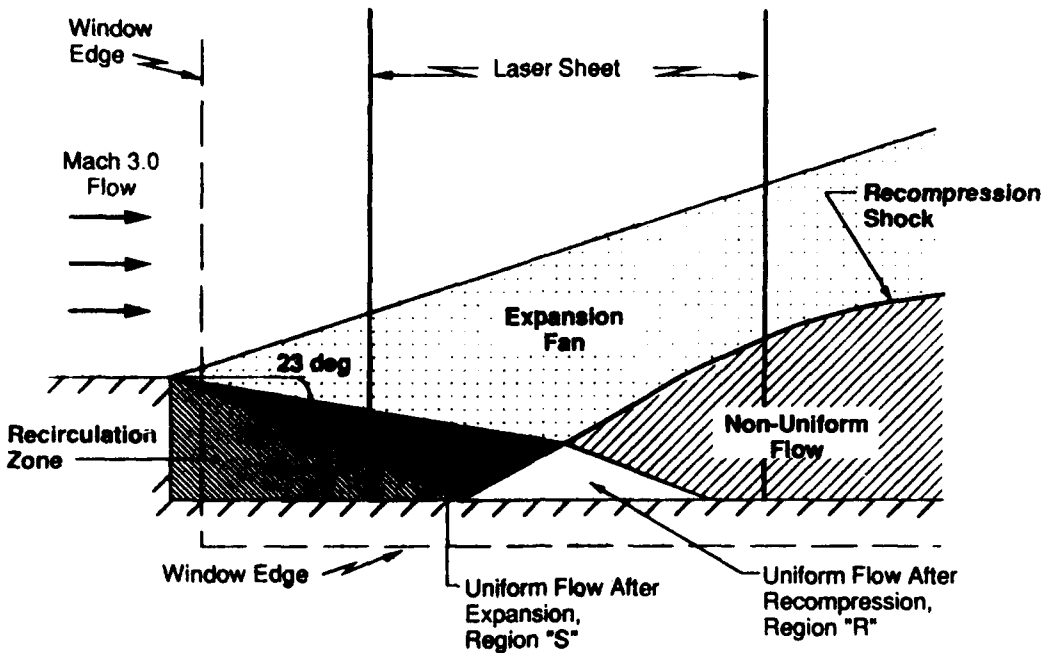


Figure 23

#### Graphic Representation of the Flowfield in the Shock Tunnel Without Injection

extent can be estimated from previous results.<sup>11-14</sup> A recompression shock is introduced by the wall and turns the flow once again so that it proceeds directly down the duct. Table 6 lists property ratios of these flow regions with respect to the mainstream.

The flowfield after the rearward facing step with injection is more complex and a detailed estimate of the features of this flow is beyond the scope of this work. However, gross features of this flow may be predicted by simply overlaying an injectant plume on the flow prediction just described. This prediction will be valid only along the centerline of the tunnel which includes the centerline of the injector. For regions not along the tunnel longitudinal centerline, the flowfield will be some combination of the no-injectant flow and the flow with injection. Figure 24 illustrates this global flow prediction and illustrates the major flow

Table 6. Relative Flow Properties

Region	P/P <sub>∞</sub>	T/T <sub>∞</sub>	$\rho/\rho_{\infty}$
S	0.137	0.619	0.233
R	0.881	1.138	0.775

features. The injectant plume will produce a bow shock in a similar fashion to that produced by a solid body in a supersonic flow. Following this shock will be the plume itself and a thin mixing region where the injectant and air meet. The plume, initially oriented at a 30 deg angle to the flow will spread as it proceeds downstream and will gradually align itself with the flow.

#### 4.3 Schlieren Measurements

Schlieren measurements of flowfields have been widely used for many decades and are a direct indicator of density variations in the flow. These images are, therefore, exceptionally appropriate for defining the position of shocks in the flow. A Schlieren imaging system simply consists of a set of spherical mirrors, a pulsed point light source, a knife edge or aperture, and a polaroid film plane for recording the images. The mirrors for this work were 4.0 in diameter, 24 in focal length and a knife edge was located at the focal point of the second mirror. The pulsed light source was a xenon flash bulb which had a 3 mm arc and flash duration verified to be less than 2  $\mu$ s long. The film was Type 55 polaroid positive/negative film in a 4 x 5 in format. All Schlieren images include the full height (3.5 in.) of the shock tunnel in the injector region.

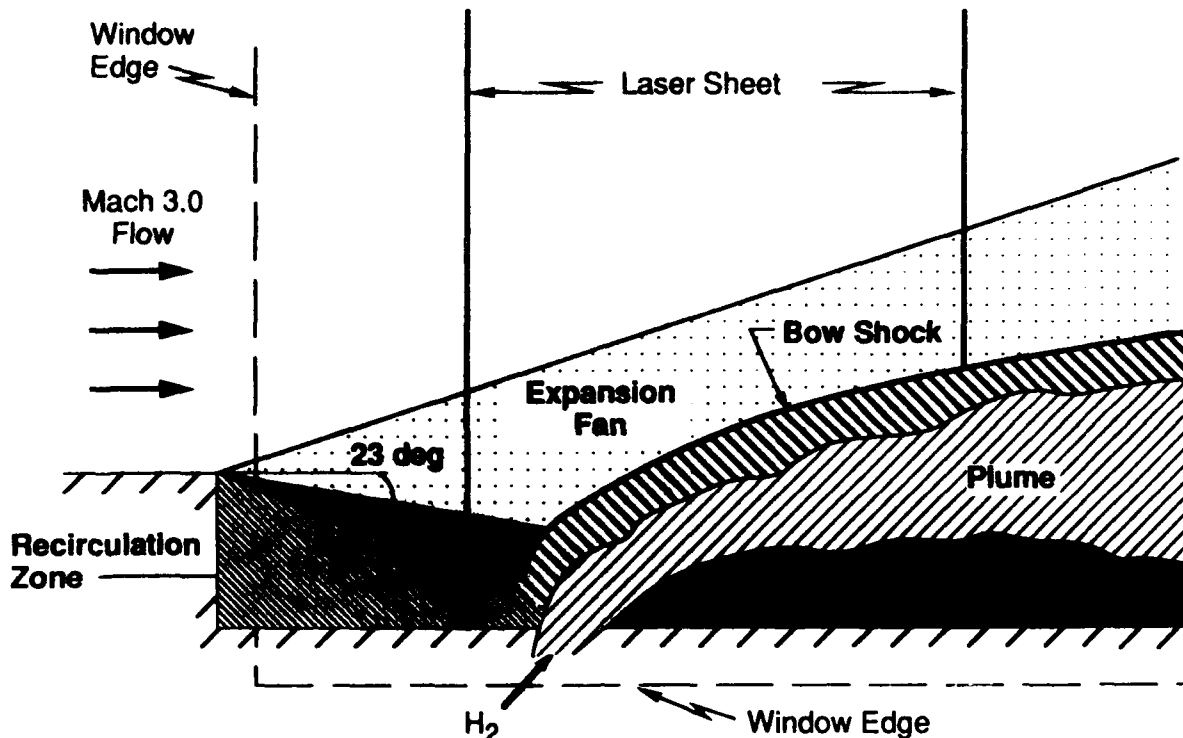


Figure 24

**Shock Tunnel Flowfield with Injection Along the Centerline of the Tunnel**

Figures 25, 26, and 27 are Schlieren photos of the flow without injection, injection without flow, and the flow with injection. The prominent aerodynamic feature in Figure 25 is the recompression shock which shows very little curvature in this region of the flow. The shock makes an approximately 13 degree angle with the tunnel wall compared with a predicted angle of 11 degrees. An additional feature of this shock is worthy of note. The shock does not appear as a single line in the image but rather appears as a group of closely spaced lines. This is an indication of a slight "waviness" in the shock as it progresses across the tunnel and this appears in the image since the measurement is a line-of-sight or path integrating measurement.



Figure 25

Schlieren Image of Flow over the Rearward Facing Step. Free stream conditions are 0.30 atm and 1350 K. Image features which are due to window imperfections are the horizontal dark streak, the concentric arcs in the left-hand side of the image and the irregular semi-transparent bumps on the bottom of the image.



**Figure 26**

**Schlieren Image of a Helium Injector Plume into a Vacuum.** Image features which are due to window imperfections are the horizontal dark streak, the concentric arcs in the left-hand side of the image and the irregular semi-transparent bumps on the bottom of the image.

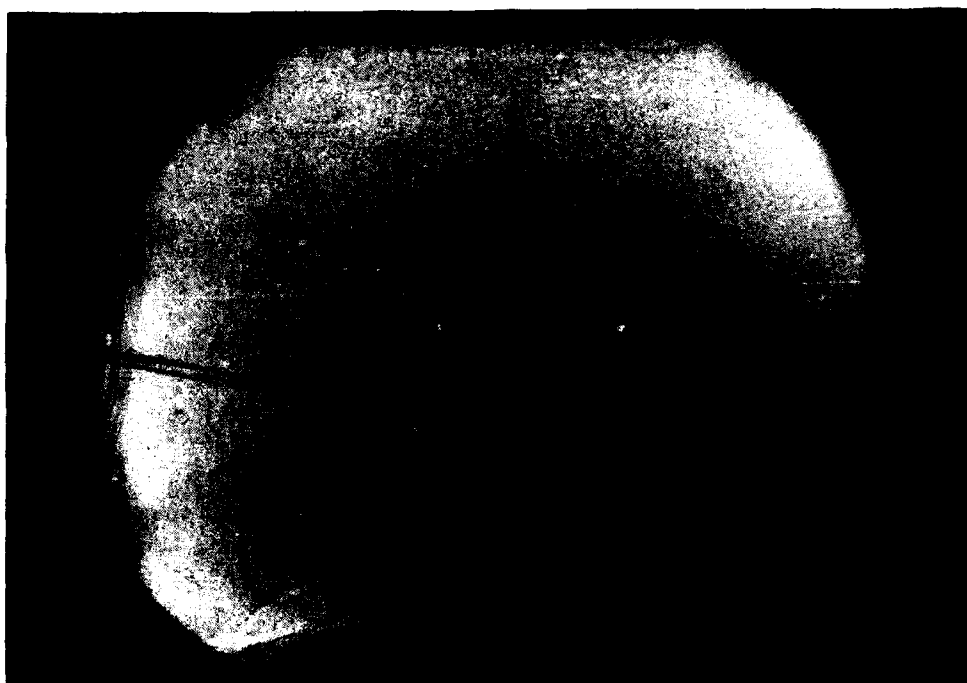


Figure 27

Schlieren Image of Helium Injection into Flow Behind the Rearward Facing Step. Free stream temperature and pressure are 1370 K and 0.30 atm. Image features which are due to window imperfections are the horizontal dark streak, the concentric arcs in the left-hand side of the image and the irregular semi-transparent bumps on the bottom of the image.

Other images of the no-injection flow condition distinctly show a lip shock originating from the boundary layer on the rearward facing step and Mach lines coming from the top wall. The mach lines are inclined at 19.5 degrees further indicating a Mach 3.0 flow.

Figure 26 is a Schlieren image of helium injection into the tunnel section with no flow (vacuum conditions). The image is interesting from the point of view that it verifies the operation of the injection system and provides a dramatic point of comparison for injection into a supersonic cross flow. Recall that the injector is oriented at a 30 degree angle to the mainstream flow and the exit is located 2.3 step heights downstream from the rearward facing step (orifice diameter 0.48 cm).

Figure 27 illustrates an image of helium injection into a Mach 3.0 cross flow. This image contains elements of each of the flow predictions discussed earlier. The wavy uppermost shock appears to be the bow shock which is expected on the tunnel centerline due to the interaction of the injectant with the tunnel flow. The wavy nature of this shock suggests that its relative shape may change with time. The lower shock in the photograph may be discussed in two parts. The portion of the shock on the left hand side of the photograph is nearly identical to the shock observed for the no injection case (Figure 27). However, this shock includes a distinct bend in the center of the photograph that is not present in the no injection case. Clearly, this bend is due to the injection but the details of the fluid mechanics are not clear. This photograph is an excellent example of the three dimensional character of this flow that is a direct result of the helium injection. Spatially resolved images (i.e., PLIF)

of the flowfield could be used to unravel the details of the interaction of the jet with the supersonic flow.

#### 4.4 Infrared Emission Measurements of NO

The infrared emission from the fundamental band of NO provides an excellent means of nonintrusively monitoring the flow produced in the shock tunnel. The temperature of the flow in the tunnel, as with other high enthalpy flow facilities, is calculated using one-dimensional gasdynamic relationships which relate conditions in a Mach 3.0 flow to those in the plenum. This calculation assumes idealized processes in the shock tube plenum and nozzle. Therefore, a real-time monitor of the flow temperature and NO concentration would serve to confirm the calculated flow conditions and continuously assess the character of the Mach 3.0 flow. The motivation for this diagnostic is therefore quite clear; it will serve to accurately quantify the flow conditions in the Mach 3.0 flow.

Simultaneous observation of the bandshape and the absolute radiance from vibrationally excited NO provides the column density (integral of number density along the line-of-sight) and path-averaged vibrational temperature of NO in the flow field. As discussed in Subsection 3.4, NO is formed at equilibrium levels in the high-temperature air in the plenum and is not significantly depleted through chemical reactions in the supersonic expansion. Thus, this species provides a convenient tracer for the number density and temperature of the air flow. Since the vibrational relaxation of NO is fast (also discussed in Subsection 3.4), the vibrational temperatures determined from infrared measurements closely approximate the kinetic temperatures in the gas flow. Furthermore, continuous monitoring of the NO

emission characteristics provides a direct measure of flow onset, stability, and duration over the test period.

Infrared emission from the fundamental ( $\Delta v = 1$ ) band of NO originates near  $5.3 \mu\text{m}$  (the center of the  $v' \rightarrow v'' = 1 \rightarrow 0$  band), and extends to longer wavelengths as higher temperatures populate higher vibrational levels. Spectrally resolved emission from the entire band was observed using a specially constructed infrared array spectrometer. This device consists of a 12-element HgCdTe linear detector array (Infrared Associates) interfaced to a 0.35m, f/6.2 monochromator (McPherson 270), with a 30-groove/mm grating blazed at  $5.5 \mu\text{m}$ . The resulting spectral resolution is  $0.19 \mu\text{m}/\text{pixel}$ . Each pixel in the array has a dedicated amplifier and digitizer which allows synchronous collection of spectra at 125 kHz. Absolute responsivity calibrations were performed with a temperature-controlled blackbody source. For the present measurements, the instrument was configured to obtain time-resolved, first-order spectra over the wavelength range 4.5 to  $7.0 \mu\text{m}$ , encompassing the entire NO fundamental band.

The field of view for this device was controlled using a folded imaging system consisting of a gold spherical mirror, focal length 100 mm, and a gold planar mirror. This system effectively controlled the collection area in the tunnel to be 3.1 by 3.1 mm along the tunnel centerline and 6.6 by 6.6 mm along its edges.

Prior to implementation on the shock tunnel, the observed radiances and bandshapes were calibrated for NO number density and vibrational temperature by recording emission spectra

from known amounts of NO (diluted in argon) shock-heated to known temperatures in the reflected shock region of a conventional, 10.4 cm (i.d.,) shock tube. Representative spectra of shock-heated NO/Ar mixtures are illustrated in Figure 28. The observed radiances and spectral distributions are in excellent agreement with values computed using Boltzmann equilibrium vibrational populations together with the known spectroscopic constants and transition probabilities of NO.<sup>15</sup> The quality of this calibration is demonstrated in Figure 29 which compares the integrated radiance to the predicted radiance using the fundamental properties of NO. Clearly, the agreement is excellent. Table 7 summarizes the results of this calibration.

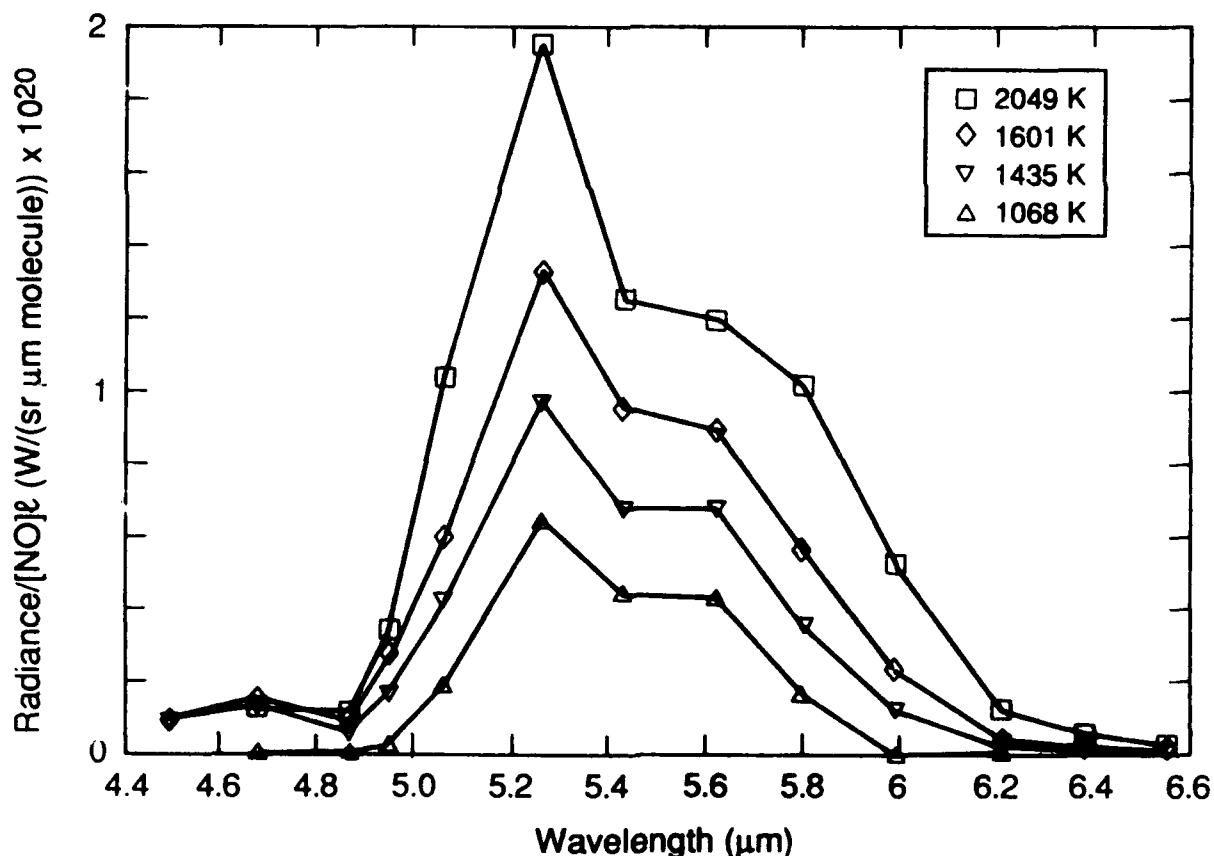


Figure 28  
Calibration Spectra for NO From Shock Tube Experiments

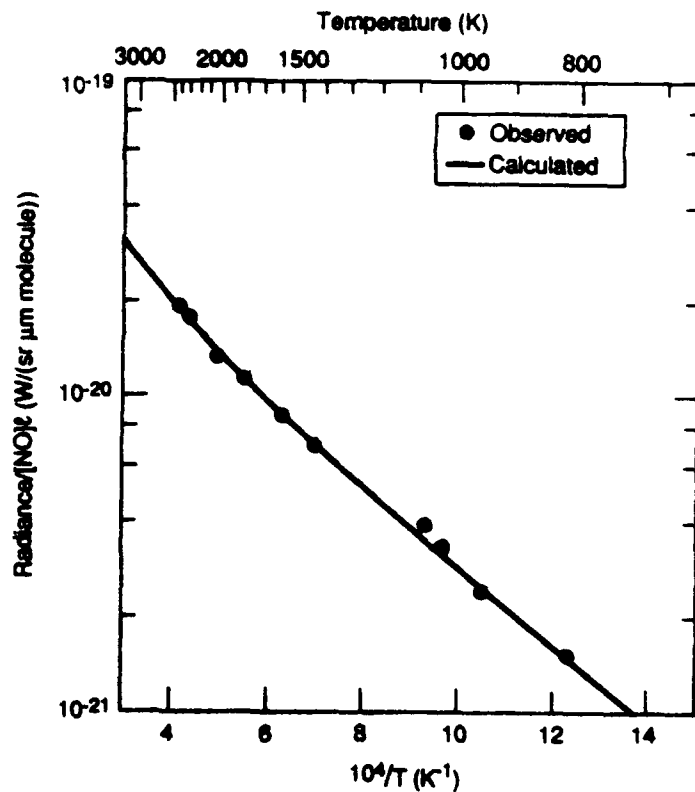


Figure 29

Observed Band Integrated Radiance Compared to Calculated Values for NO

Table 7. NO(v) Spectral Calibration

$\lambda$ ( $\mu m$ )	A (W/(sr molecule))	B (Kelvin)
5.26	(7.0 $\pm$ 0.2) (-20)	2618 $\pm$ 45
5.43	(4.1 $\pm$ 0.3) (-20)	2423 $\pm$ 110
5.62	(3.8 $\pm$ 0.1) (-20)	2373 $\pm$ 39
5.80	(7.3 $\pm$ 0.6) (-20)	4101 $\pm$ 102
5.99	(7.9 $\pm$ 0.9) (-20)	5584 $\pm$ 143
6.21	(1.3 $\pm$ 0.7 (-19)	9265 $\pm$ 822
6.38	(5.2 $\pm$ 3.6) (-20)	9203 $\pm$ 978

The observed temperature dependence of optically thin radiance at several wavelengths is illustrated in Figure 30. Ratios of radiance at any two wavelengths are sensitive only to temperature, as shown in Figure 31. Thus, observation of the radiance ratios, under optically thin conditions, provides a measure of temperature via the relationships illustrated in Figure 31; this information together with the absolute radiance at a given wavelength (again optically thin) in turn provides a determination of NO number density via the radiance relationships shown in Figure 30.

For some of the shock tube calibration measurements, spectra were observed at sufficiently large NO number densities that the  $1\rightarrow0$  transition was optically thick. This results in a non-linear relationship between NO number density and the radiances at wavelengths shorter than  $5.8 \mu\text{m}$ , where the total intensity contains contributions from this band. However, wavelengths of  $5.8 \mu\text{m}$  and above are not affected by the optically thick  $1\rightarrow0$  band, and the corresponding radiances remain optically thin, providing an accurate measure of NO number density and temperature. While this strategy can also be applied to shock tunnel measurements under optically thick conditions, the NO number densities and path lengths in our tunnel are small enough that the NO radiance is optically thin over the entire band.

An example determination of NO number density and temperature at the exit plane of the nozzle is given in Figures 32 to 36. These figures represent two different tunnel test conditions and their processing was essentially identical. Data from the IR spectrometer was filtered using a 12.5 kHz sharp-cutoff, low pass filter and datapoints at 0.1 msec intervals

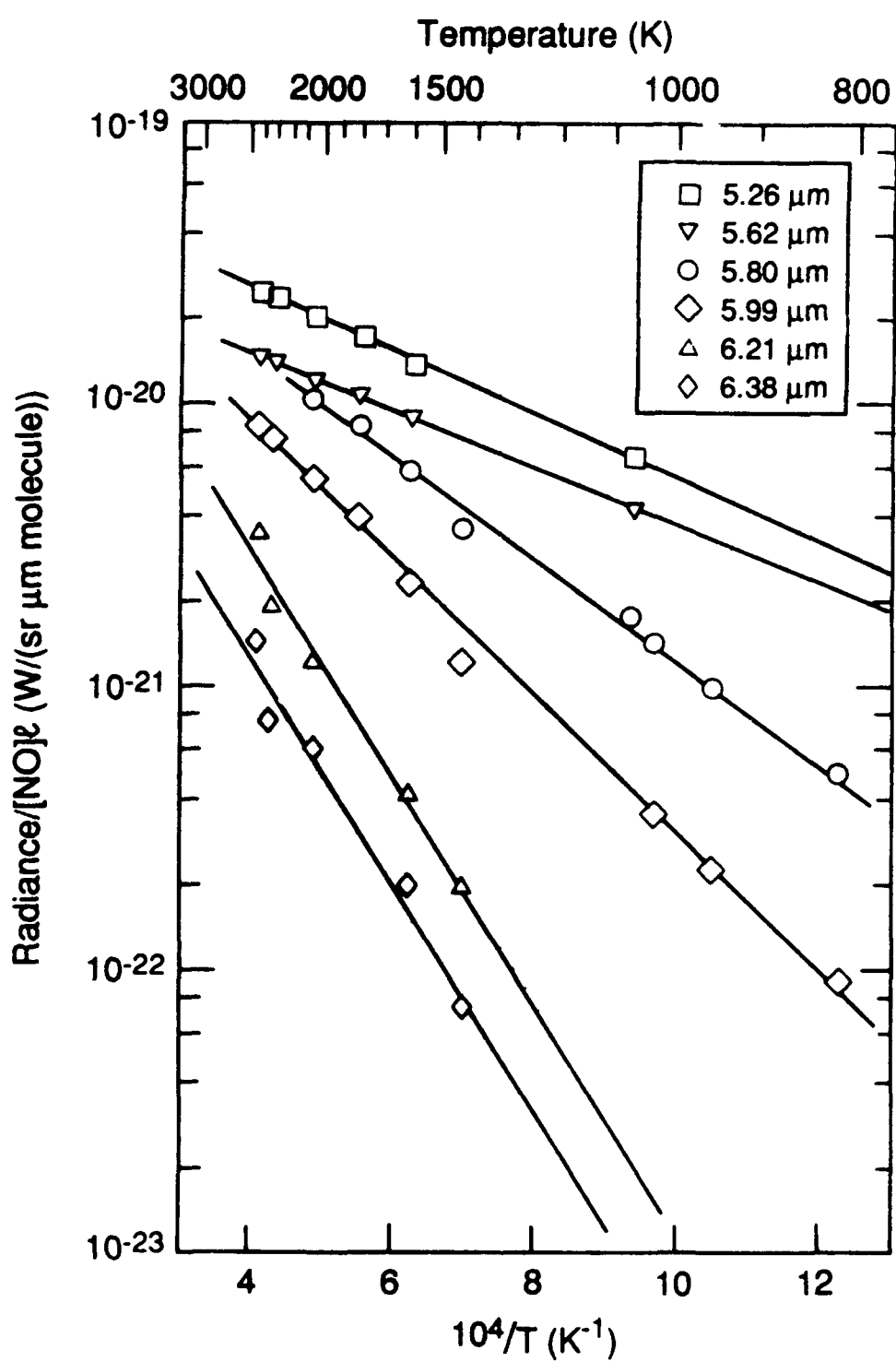


Figure 30

NO Radiance as a Function of Temperature and Wavelength

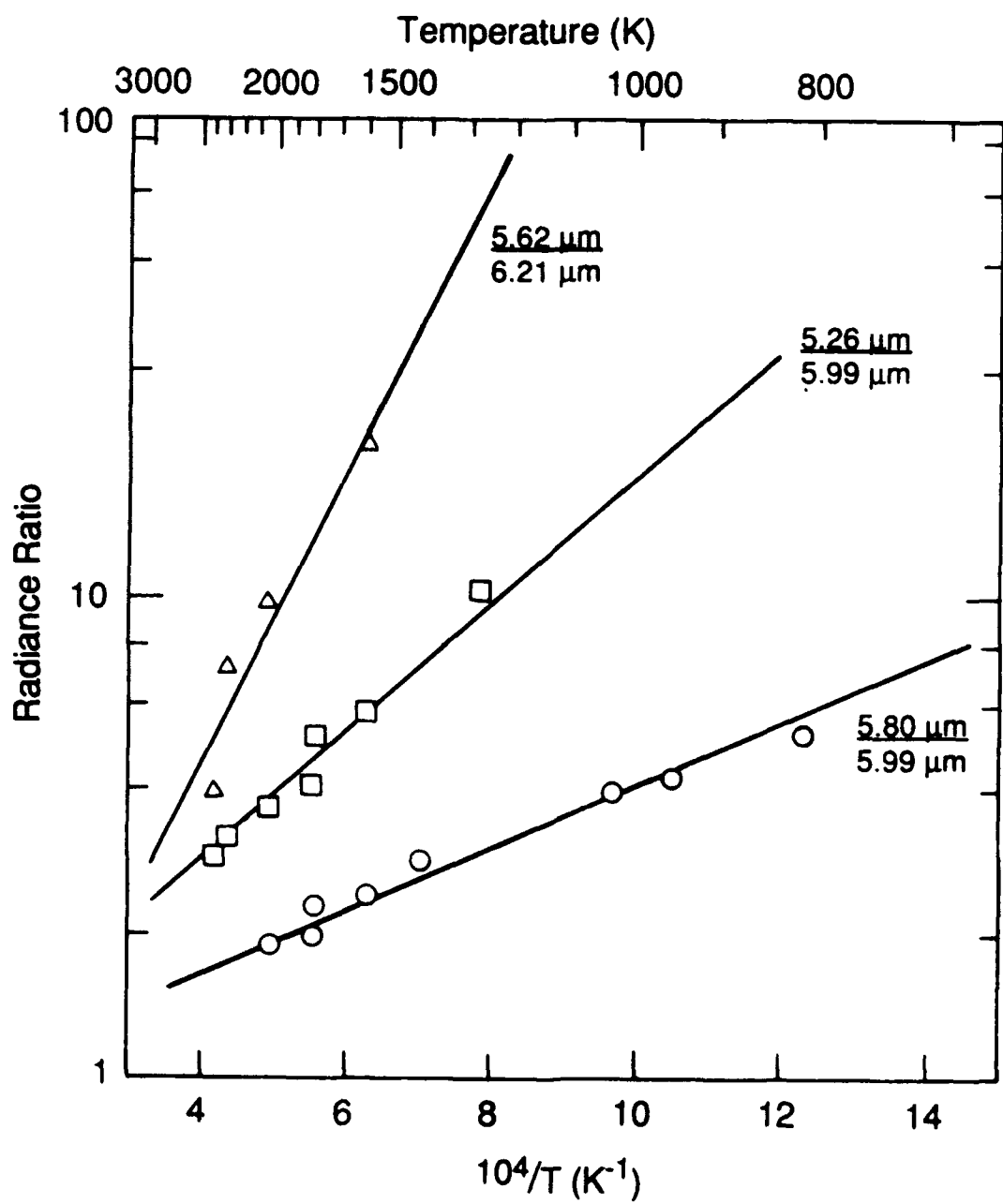


Figure 31

Dependence of NO(v) Radiance Ratios on Temperature

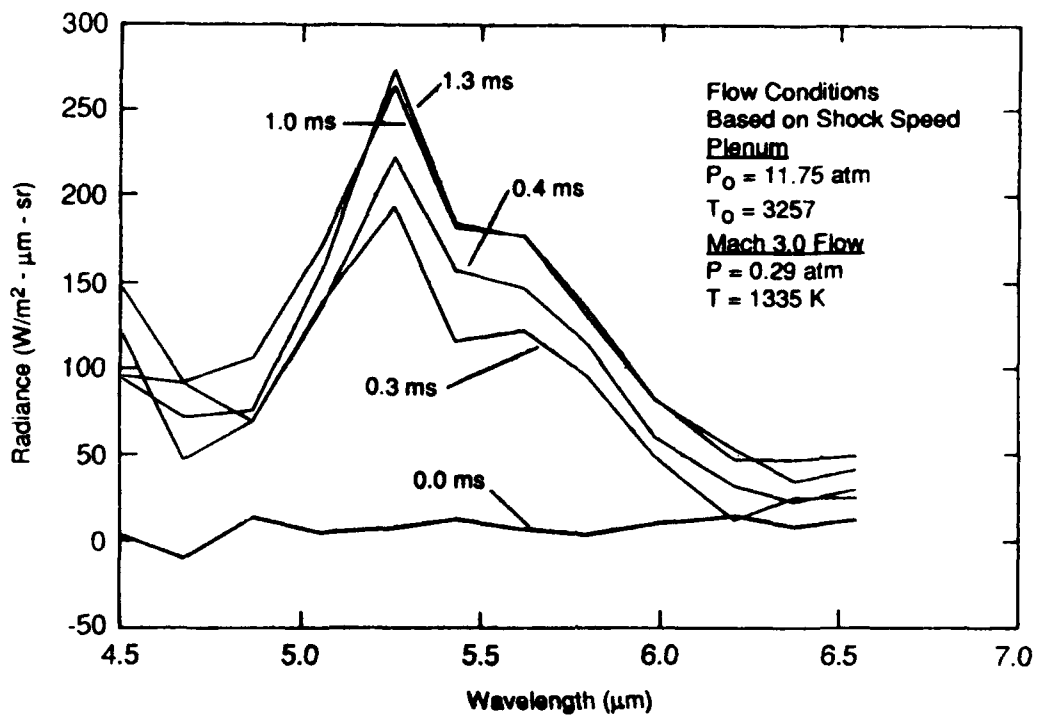


Figure 32

NO Spectra in the Shock Tunnel for Several Times During the Flow

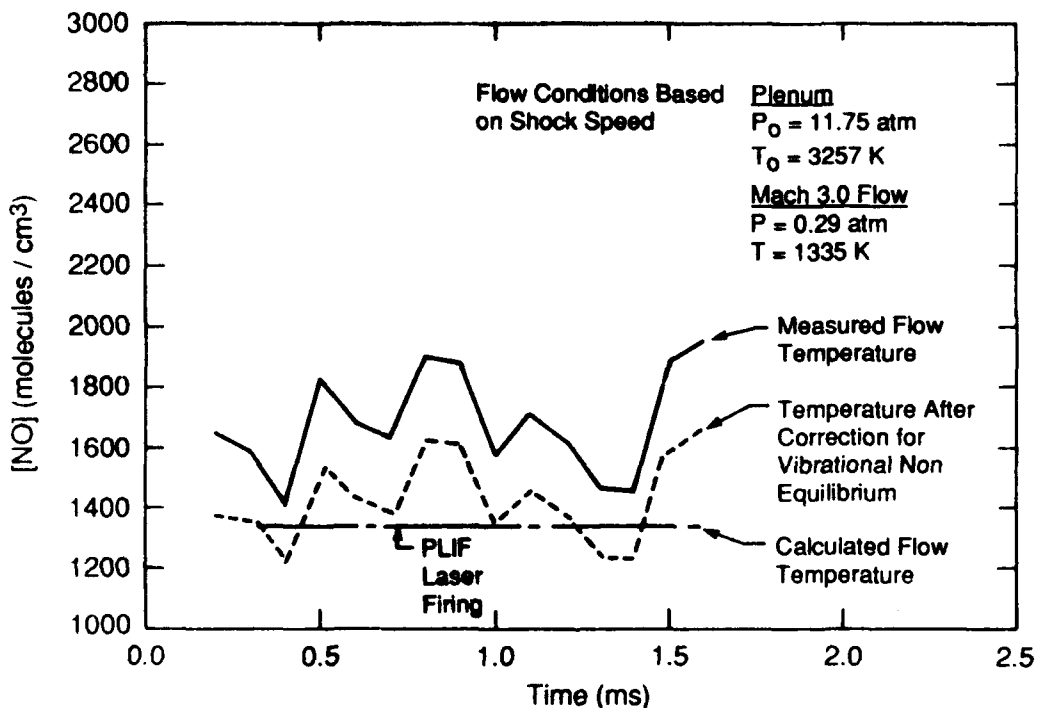


Figure 33

Temperature Measurements Based on NO Emission from a Mach 3.0 Flow

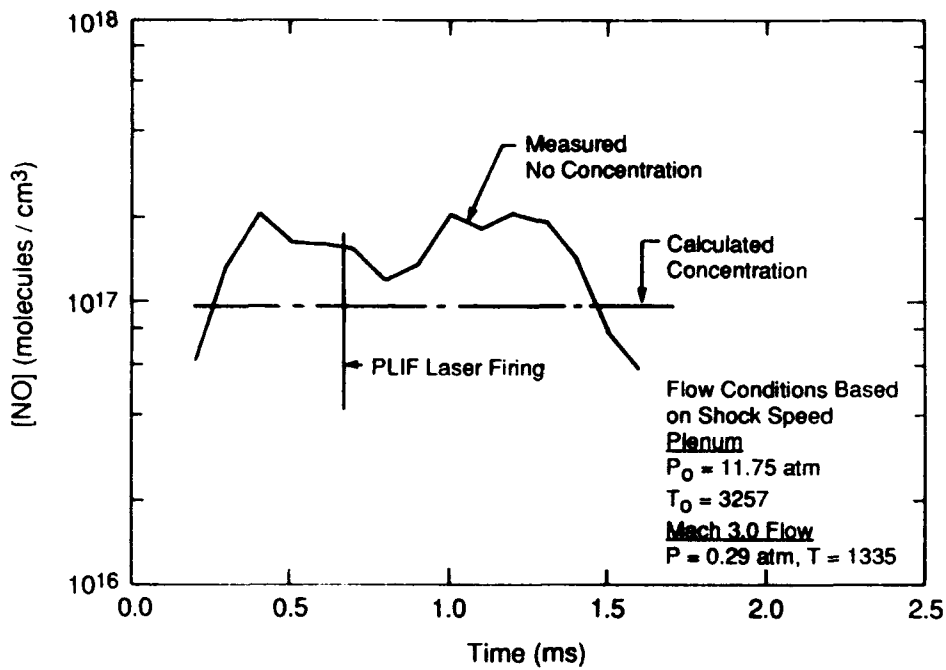


Figure 34

#### NO Concentration as Measured in the Shock Tunnel

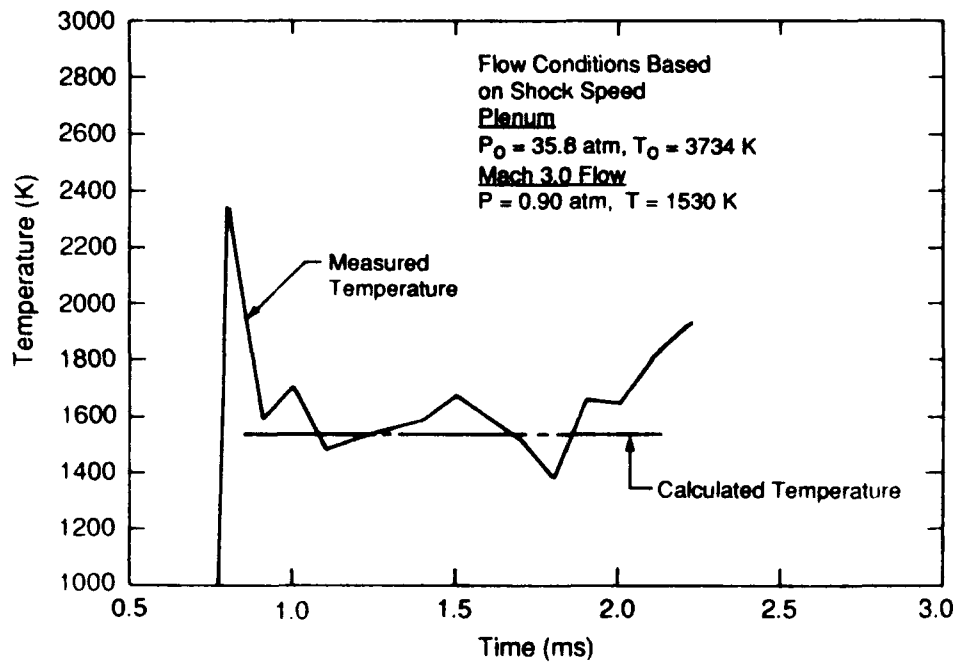
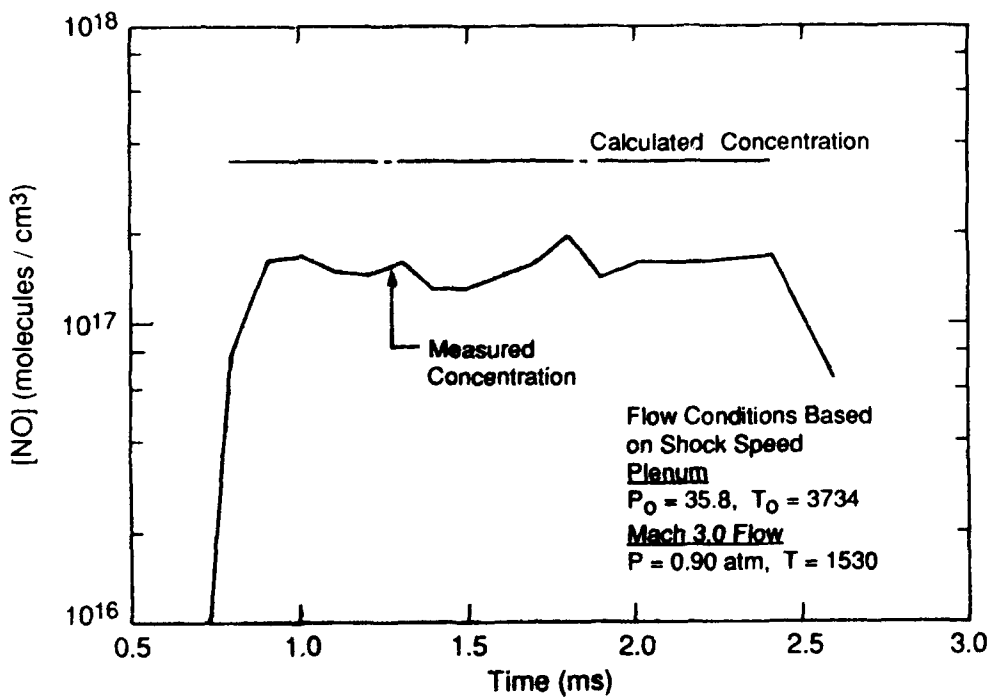


Figure 35

Flow Temperature from NO Radiation in the Mach 3.0 Flow Compared with an Idealized Computed Value



**Figure 36**

#### NO Concentration in the Shock Tunnel Based on Radiometer Measurements

were output to a separate data processing program. The previously described calibration constants and Eq. (15):

$$T = \frac{B_2 - B_1}{\ln \left( \frac{N_1 A_2}{N_2 A_1} \right)} \quad (15)$$

where:

- |           |   |   |
|-----------|---|---|
| T         | - | flow temperature                                |
| A, B      | - | calibration constants                           |
| N         | - | observed radiance                               |
| Subscript |   |   |
| 1,2       | - | denotes wavelength $\lambda_1$ or $\lambda_2$ . |

are used to determine the temperature of the flow. This temperature is then used to determine the number density of NO in the flow using the radiance observed at  $5.26 \mu\text{m}$ . Figure 32 illustrates a series of spectra observed for a particular shock tunnel experiment and the figure illustrates the time evolution of the NO spectral signal. This particular experiment included a significant background contribution from particulate in the flow (a problem which has subsequently been removed); our data processing corrects for this background by subtracting off an interpolated background using  $6.38$  and  $4.68 \mu\text{m}$  as end points. An added advantage to the continuous spectral coverage is this ability to determine background levels from particulate or other interfering radiators. Figure 33 illustrates the indicated flow temperature based on an average of the temperature predicted by ratioing  $5.26 \mu\text{m}$  to  $5.88$  and  $5.99 \mu\text{m}$  and ratioing  $5.43 \mu\text{m}$  to  $5.8$ ,  $5.99$ , and  $6.21 \mu\text{m}$ . The measured flow temperatures are consistently higher than those predicted using the shock speed derived conditions in the plenum. Vibrational nonequilibrium (see Subsection 3.4) can explain a 15 percent discrepancy in the observed and kinetic temperatures. Application of this factor makes the agreement of the calculated temperature, based on conditions in the plenum, and the radiometrically determined temperature quite good. However, the radiometric signal clearly indicates that the temperature in the Mach 3.0 flow is by no means constant. These temperature variations can very well be attributable to non-ideal shock reflection off the end wall and secondary reflections from the contact surface. The measured number density for this same shock condition is shown in Figure 34 and agrees within a factor of 2 with the ideally calculated value. Figures 35 and 36 illustrate results from a separate shock tunnel event. For this particular case, the pressure in the plenum is high enough that no correction for vibrational non-equilibrium is required and the agreement

between calculated and measured is quite good. However, the number density for NO as shown in Figure 36 is lower than expected.

Concurrent measurements of NO spatial distributions, in the same uniform flow region sampled by the infrared measurements, were made by planar laser-induced fluorescence (PLIF) using the pulsed laser excitation techniques described in detail in Subsection 4.6. These measurements, made at the flow time indicated in Figure 34, provide an instantaneous view of the spatial uniformity of NO in the flowfield, as well as estimates of NO number densities via both the observed fluorescence yields and the resonance absorption of the laser beam. PLIF images verify that the flow at the nozzle exit is spatially uniform, as expected. The observed attenuation of the laser sheet gives an estimated number density [NO]  $\sim 3.2 \times 10^{17}$  mole/cm<sup>3</sup>, the observed fluorescence yields are consistent with [NO]  $\sim 2.0 \times 10^{17}$  molec/cm<sup>3</sup>, and the NO infrared emission measurement yields  $1.5 \times 10^{17}$  mole/cm<sup>3</sup>.

In view of the large (factor of 2 to 3) uncertainties in absorption cross sections, laser/absorber spectral overlap, laser energy delivered to the flow, and quenching factors required to evaluate [NO] for the laser-based measurements, we consider these values to be in good agreement with the more quantitative value of [NO] obtained by infrared emission ( $\sim 1.5 \times 10^{17}$ ). This comparison illustrates the utility of line-of-sight passive emission as a quantitative support diagnostic for instantaneous flowfield imaging measurements.

This section has illustrated the utility of the NO infrared emission diagnostic; it offers a nonintrusive method of monitoring the flow's temperature in addition to providing a direct measure of the high temperature flow onset, stability, and duration. Clearly, obvious improvements such as a larger calibration data set and improved data reduction algorithms (such as determining the temperature via a least mean square fit of the spectra) could be produced. However, regardless of the implementation, this type of diagnostic provides a critical, nonintrusive means of evaluating the character of a high temperature flow. Idealized calculations of system performance can therefore be routinely verified using this diagnostic.

#### 4.5 OH Absorption Measurements

As a second line-of-sight diagnostic based on the optical response of a specific molecule, we performed an initial set of experiments and supporting calculations to quantify the use of resonance absorption as a means of monitoring the number density and rotational temperature of OH. The importance to combusting flows is that it is a direct indicator of both ignition and, at downstream flow locations, the degree of reaction completion.

Absorption measurements of OH in combusting systems require, in addition to an ultraviolet source which overlaps with the absorption features of OH, high source brightness due to the emission intensity from either chemiluminescent OH emission or thermally produced OH emission (OH A $\rightarrow$ X). Due to this source brightness constraint, we focused our efforts on a diagnostic using a 1 kW arc lamp as the source rather than the more traditional microwave discharge lamp. The potential increase in the source brightness is quite large as represented by irradiance on a plane 50 cm from the source. The arc lamp produces up to 10  $\mu\text{W}/\text{cm}^2\text{-nm}$  (550 mW/cm $^2\text{-nm}\text{-sr}$  at the source) near 300 nm while a microwave dis-

charge lamp was measured to emit approximately  $0.04 \mu\text{W}/\text{cm}^2\text{-nm}$  (or  $32 \text{ mW}/\text{cm}^2\text{-nm}\cdot\text{sr}$  at the source) in its stronger radiating lines. The arc lamp has the added advantage that its radiating area is smaller which makes it easier to accurately deliver the lamp energy along a well specified beam path.

The Appendix describes a spectral simulation which predicted absorption line widths for OH as a function of temperature and pressure and allowed the selection of a series of lines based on the line spacing. Table 8 lists the available lines in the OH 0-0 band on a criterion of  $0.6\text{\AA}$  line separation (line separation is considered from the center wavelengths of each line). These lines are the best choices for an absorption measurement that will use a broad band source and a monochromator to isolate the region around one line.

Table 8. OH 0-0 Band Lines with  $0.6\text{\AA}$  Separation

Line	Wavelength ( $\text{\AA}$ )	Einstein A Coefficients ( $\text{s}^{-1}$ )
R <sub>2</sub> 14	3071.145	$2.67 \times 10^5$
R <sub>2</sub> 4	3074.369	$2.3 \times 10^5$
R <sub>2</sub> 3	3077.028	$2.05 \times 10^5$
R <sub>2</sub> 1	3084.050	$1.2 \times 10^5$
R <sub>2</sub> 20	3089.008	$2.21 \times 10^5$
P <sub>1</sub> 5	3101.229	$4.3 \times 10^5$
R <sub>2</sub> 23	3104.348	$1.91 \times 10^5$
Q <sub>21</sub> 14	3115.077	$1.2 \times 10^4$

The Einstein A coefficients are included in Table 8<sup>16</sup> and may be used as a means of predicting the absorption for a specific experimental setup. Equation (16) defines the fractional absorbance per molecule for optically thin systems with the absorption line width and source line width modeled as centered triangles, Figure 37. The derivation for Eq. (16) is given in the Appendix:

$$A = \frac{1}{\Delta\lambda_s} \left[ 1 - \frac{1}{3} \frac{\Delta\lambda_a}{\Delta\lambda_s} \right] \ell \left( \frac{1}{8\pi c} \frac{g_i}{g_j} \right) \phi_j A_{ij} \quad (16)$$

$$\text{for } \frac{\Delta\lambda_a}{\Delta\lambda_s} \leq 1.0$$

where:

$\Delta\lambda_a$	-	absorption line width
$\Delta\lambda_p$	-	source line width
$\ell$	-	optical path length in absorbing media
$c$	-	speed of light
$g_i, g_j$	-	degeneracy of upper and lower states
$\phi_j$	-	relative rotational population
$A_{ij}$	-	Einstein A coefficient.

Equation (16) illustrates that absorption is proportional to the relative rotational population, and has a more complicated dependence on the absorption and source line widths. However, note that the effect of pressure as manifested in the line width of the absorber, will be relatively minor for systems where the absorption linewidth is significantly smaller than the

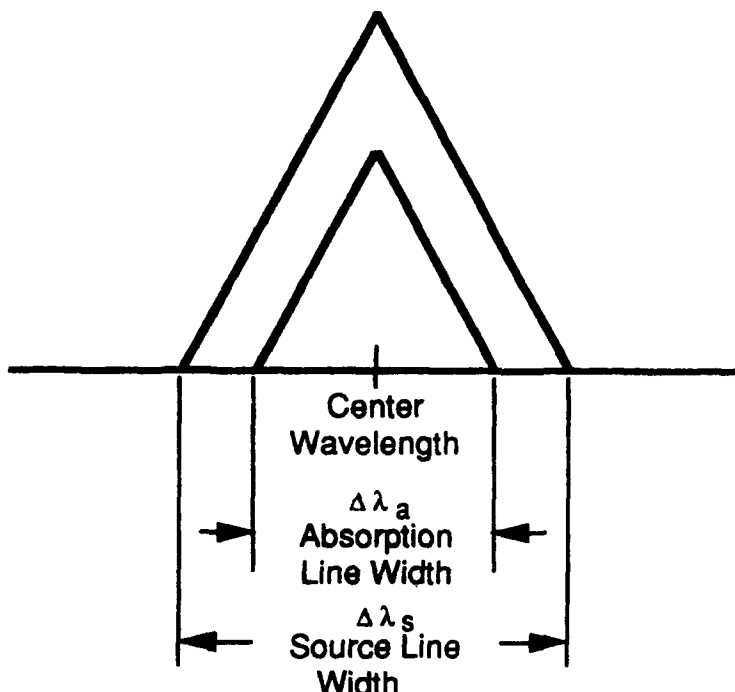


Figure 37

### Illustration of Absorption and Source Lines Modeled as Triangles

source linewidth. Equation (17) gives the ground state relative rotational population function for OH and is plotted as a function of temperature in Figure 38:

$$\phi_j = \frac{(2J+1)}{Q_r} e^{-BJ(J+1)hc/kT} \quad (17)$$

$$Q_r \approx kT/hcB \quad \text{for } T > 300 \text{ K}$$

where:

$J$  - rotational quantum number

$k$  - Boltzmann constant

$h$  - Planck's constant

$B$  -  $18.5 \text{ cm}^{-1}$  for OH.

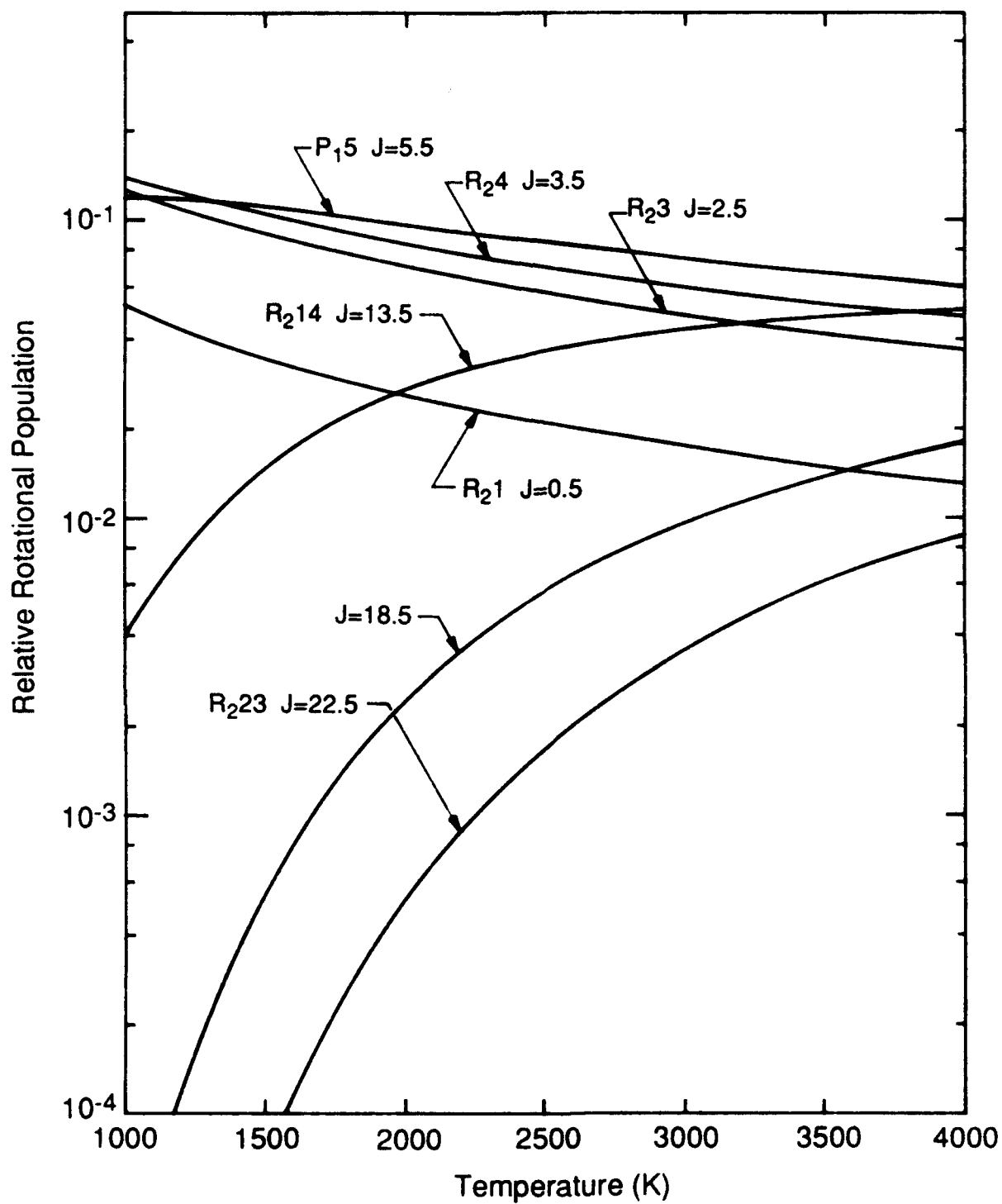


Figure 38

Ground State Partition Function for Selected OH Absorption Lines

This plot illustrates two critical features for isolated line measurements. First  $P_{15}$  is an excellent choice for one of the measurements since it is relatively insensitive to temperature and is highly populated over the temperature range of interest. Second, since a primary goal of single line measurements is to derive concentration and temperature information,  $R_{214}$  is an appropriate second choice. Clearly, the ratio of relative populations for  $P_{15}$  and  $R_{214}$  will be a reasonable measure of temperature. The primary disadvantage to the arc lamp system is that the spectral overlap must be controlled with a monochromator and the system sensitivity will to a large degree depend on the resolution of the monochromator (hence, the  $1/\Delta\lambda_s$  in Eq. (16)). Since we are using a monochromator as a means of producing a narrow line source, the ultimate limitation for the system will be the resolving power of the monochromator and the signal levels at these very high resolution settings.

A set of shock tube tests for this diagnostic using both an arc lamp (Oriel Model 66028) and a microwave discharge lamp (with  $\text{He}/\text{H}_2\text{O}$  mixture flowing through it) as the source were performed to evaluate the OH absorption system. These tests were performed using our 4 in. ID shock tube and a mixture of 1 percent hydrogen and 1 percent oxygen in argon. Initial results are summarized in Table 9 and indicate that the microwave lamp measurement is significantly more sensitive than the arc lamp system. The detection limits for the two systems, based on the observed measured noise and the experimentally defined cross sections, are also given in Table 9. The detection thresholds are all less than  $5 \times 10^{15} \text{ cm}^{-3}$  while the expected concentration is significantly higher. As an example, an  $\text{H}_2/\text{Air}$  system initially at 1300 K and stoichiometric conditions will produce approximately  $8 \times 10^{16} \text{ cm}^{-3}$  of OH. A note on the discrepancy between the calculated and experimentally observed cross

Table 9. OH Absorption at Approximately 30 atm and 1500 to 1600 K

	Cross Section	Detection Limit
Microwave Lamp System	$\sigma = 5.5 \times 10^{-18} \text{ cm}^2$	$1.5 \times 10^{15} \text{ cm}^{-3}$
Arc Lamp System	$\sigma = 1 \times 10^{-18} \text{ cm}^2$	$5.0 \times 10^{15} \text{ cm}^{-3}$
Calculated Arc Lamp System	$\sigma = 3 \times 10^{-18} \text{ cm}^2$	$8.0 \times 10^{14} \text{ cm}^{-3}$

sections for the arc lamp is in order. Two items contribute to this discrepancy. First, the assumed triangular shape is not a good approximation to the very pressure broadened line which we would expect at 30 atm. Second, and more important, the absorption and source lines may not have been perfectly centered for this experiment. This problem would be addressed by carefully monitoring, and adjusting, the monochromator wavelength immediately before a shock. A sample result for the arc lamp system is shown in Figure 39 and Figure 40 illustrates the optical train for the arc lamp measurements.

A note on these results is in order. The microwave discharge lamp measurement has demonstrated a superior cross section to that for the arc lamp. However, the detection threshold is proportional to a ratio of cross section to noise level. Our experience with microwave discharge lamps has demonstrated source related noise levels to be in the 8 to 10 percent range. The noise level inherent in the arc lamp is approximately 2 percent. By using a higher groove density grating, which allows increased slit widths on the monochromator, and with a redesigned optical setup between the lamp and the monochromator, the 2 percent noise level inherent in the arc lamp would become the limiting noise level for the system. The detection threshold could therefore improve to the stated value in Table 9 which is slightly superior to that for the microwave discharge lamp.

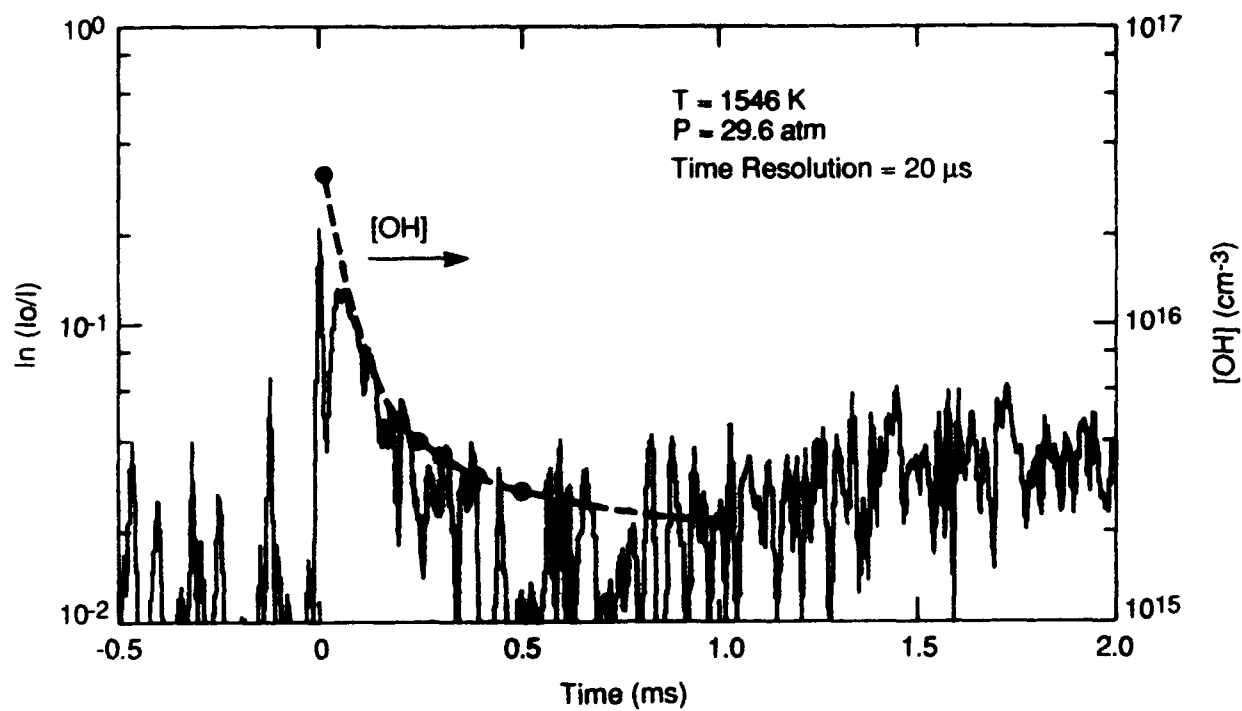


Figure 39

Measured Absorption for the Arc Lamp System and Predicted Number Densities of OH

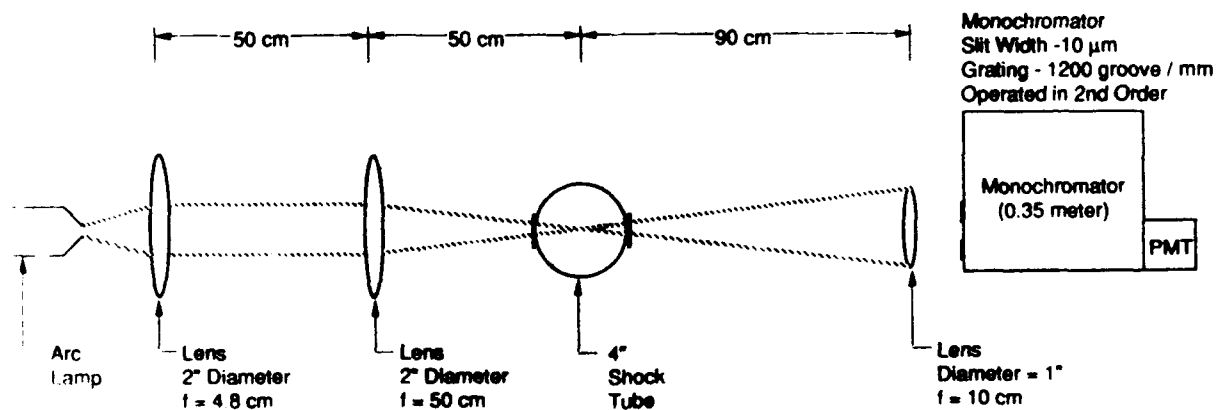


Figure 40

Schematic Diagram of Arc Lamp Measurement System

Finally, the results from this program allow an evaluation of line-of-sight absorption measurements in the high temperature reaction regions of a moderate scale combustor. Effective absorption measurements require the source radiance, as imaged in the measurement region, to be significantly brighter than thermal and chemiluminescent emission due to OH A-X transitions. As described in Subsection 4.6, an emission image taken downstream of the injector station contained a source radiance across the 7.6 cm length that was greater than  $500 \mu\text{W}/\text{cm}^2\text{-sr-nm}$ . This emission source intensity is greater than the intensity of the microwave lamp ( $320 \mu\text{W}/\text{cm}^2\text{-sr-nm}$ ). Since the maximum intensity produced by any imaging optical system cannot exceed the intensity of the source, absorption measurements using a microwave lamp as the source for this system will not work. However, the arc lamp is significantly brighter ( $5.5 \times 10^5 \mu\text{W}/\text{cm}^2\text{-nm-sr}$ ) and therefore can be an effective source for absorption measurements in the presence of strong OH emission. The problem of overcoming natural emission in the system is a common problem with high temperature and/or large scale devices. The criterion for successful absorption measurements is summarized by Eq. (18):

$$N_{\text{source}} > N_{\text{sys}} \ell \quad (18)$$

where:

$N_{\text{source}}$	-	source radiance $\mu\text{W}/\text{cm}^2\text{-sr-nm}$
$N_{\text{sys}}$	-	volumetric system radiance $\mu\text{W}/\text{cm}^3\text{-sr-nm}$
$\ell$	-	absorption path length.

Clearly, large scale devices and high emission intensity systems require very bright absorption measurement sources. As an example of the relationship of the necessary source brightness to system parameters, Figure 41 illustrates expected emission levels from a 7.6 cm path length (identical to the shock tunnel) with an OH concentration of  $10^{16}$  molec/cm<sup>3</sup>. Estimation of emission intensities from the OH A-state is simply due to the equilibrium thermal population. This figure clearly illustrates that absorption measurements using the arc lamp can be used to significantly higher temperatures than the microwave discharge lamp.

This section has discussed the initial details of a line-of-sight measurement system for monitoring OH concentration and rotational temperature. As discussed, the arc lamp is a sufficiently intense source to use in high temperature systems with path lengths of 8 cm or greater. A final instrument for this type of measurement would probably be a highly wavelength dispersive monochromator with dual output slits for monitoring two discrete regions of the spectrum simultaneously. This system would provide temporal information on the concentration and temperature of OH.

#### 4.6 Planar laser-Induced Fluorescence Measurements

This section describes the portion of the program devoted toward development and demonstration of Planar Laser-Induced Fluorescence (PLIF) techniques for measurements of concentration and temperature distributions in the shock tunnel flowfield. It begins with an overview of the technique and a description of the unique detector system developed for this contract. The second section describes details of the fluorescence approach used for measurements of the NO radical, including special considerations for quantitative

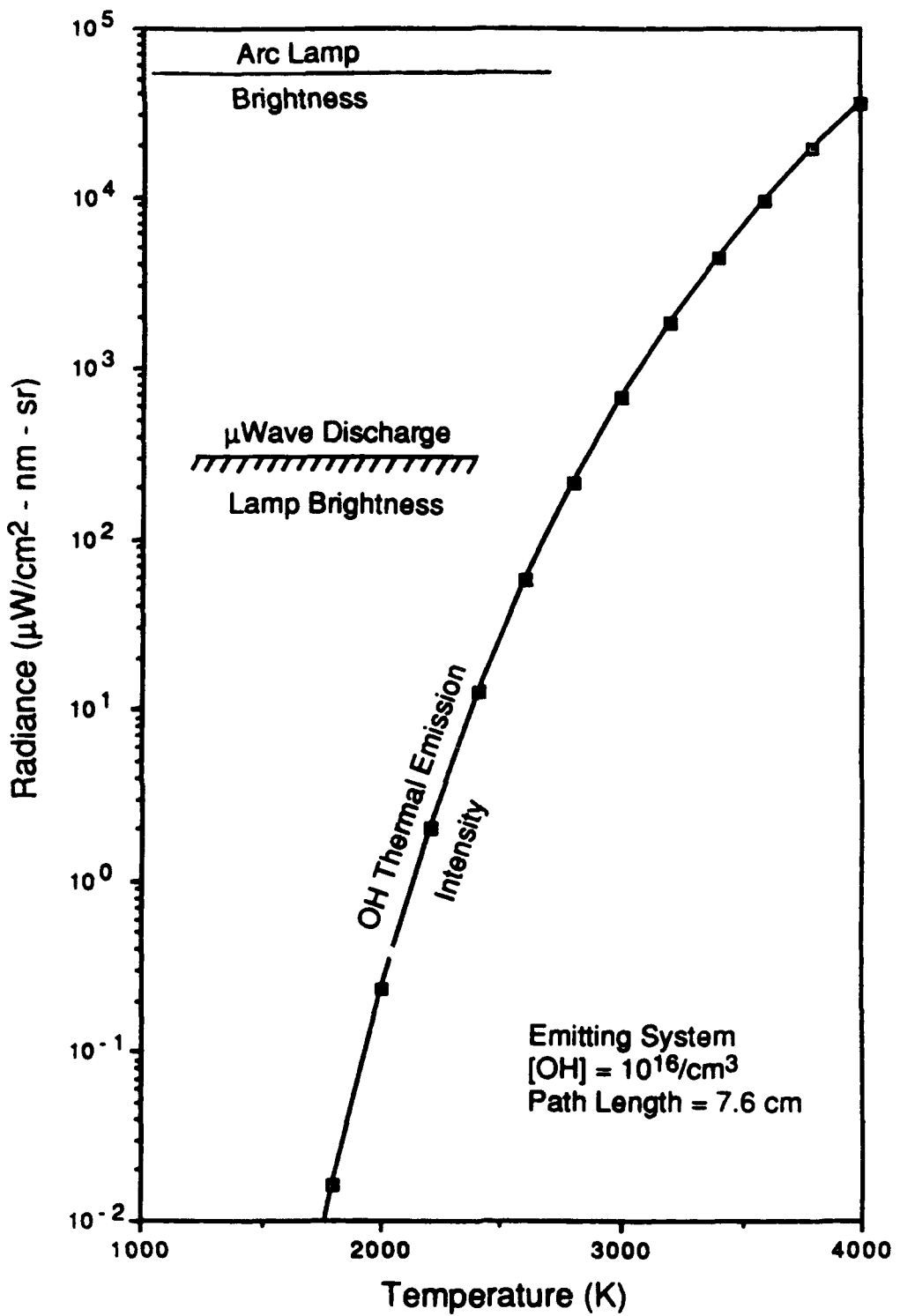


Figure 41

Comparison of Radiance from Thermally Excited OH( $A \rightarrow X$ ) with an Arc Lamp and Microwave Discharge Lamp

measurements in high temperature, compressible flowfields. Results of several PLIF experiments in the shock tunnel are presented and described. In the final subsection, details of the approach and results for OH fluorescence are discussed.

#### 4.6.1 Overview and Camera Description

A PLIF system consists of three basic components: a pulsed, tunable laser source; a two-dimensional detector array; and laser beam shaping optics. The detector system is interfaced to a data acquisition/image processing work station and timing electronics are required to synchronize the operation of the camera and laser. A generic setup is shown in Figure 42.

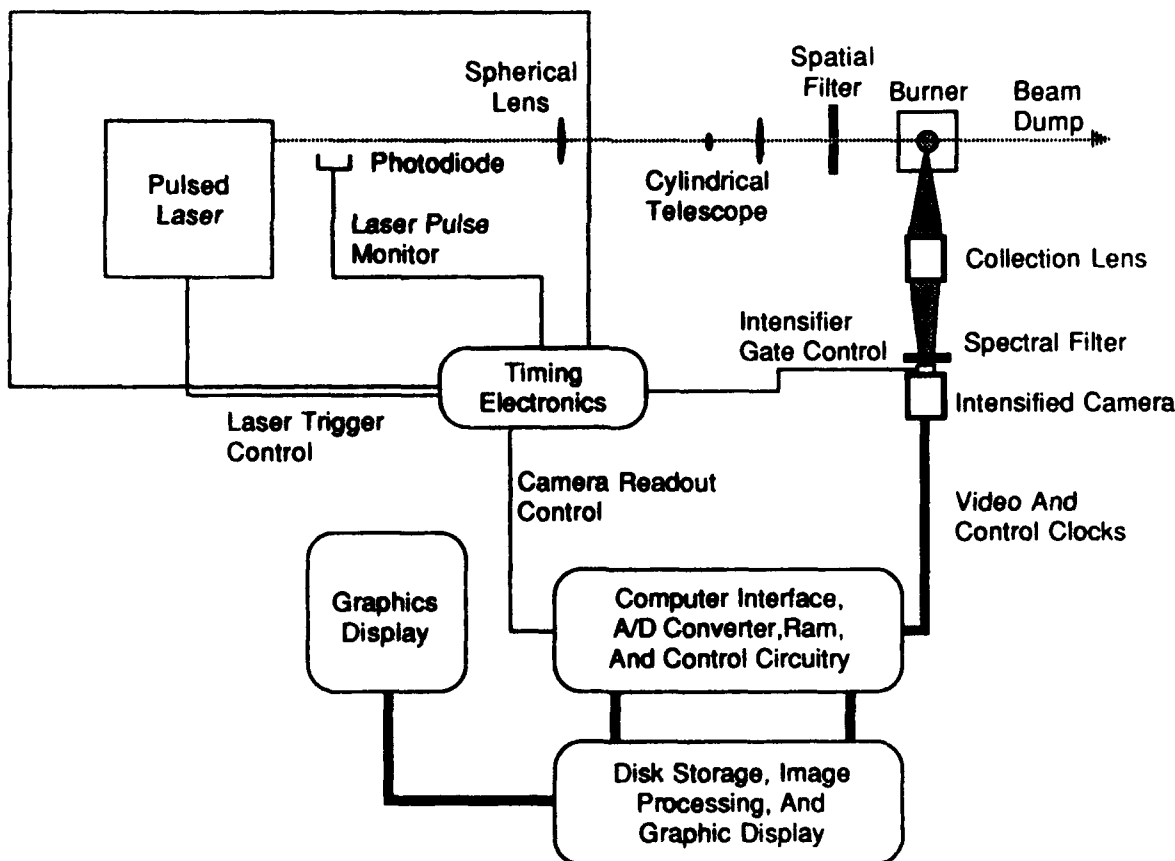


Figure 42

Typical PLIF Experimental Setup

The output from the laser is tuned in wavelength to correspond to a particular transition of a particular chemical species of interest. The beam is shaped into a thin sheet and focussed across the plane of interest in the flowfield. The fluorescence generated in the laser plane is imaged onto the detector array using appropriate collection and filtering optics. Since the laser pulse duration is typically on the order of 5 to 10 ns, the resultant image recorded at the detector array is an instantaneous record of the fluorescence distribution from the frozen flow. As described in Subsection 4.6.2, the fluorescence data can be reduced to yield the interrogated species' concentration ( $\text{cm}^{-3}$ ), mole-fraction (ppm), or temperature, among other parameters.

The fluorescence experiments in this program were accomplished using an excimer-pumped dye laser system. A Lambda-Physik FL3002 dye laser was purchased under the program and pumped with a PSI-owned Questek Model 2800 excimer laser. The dye laser permits continuous wavelength generation from  $\sim 320$  nm to over 1000 nm. With the addition of BBO ( $\beta$ -Barium Borate) doubling crystals, the UV coverage was extended to below 220 nm. For the fluorescence applications explored in this program, the UV capability of the laser system was the most relevant. A summary of the pulse energies available from the laser system is shown in Figure 43, along with the approximate wavelength location of important transitions of the atomic and molecular species of interest in hydrogen combustion applications.

The imaging detector system constructed under this program consisted of a high-resolution, intensified, CCD array photodetector. This detector (camera) was interfaced to a Compaq

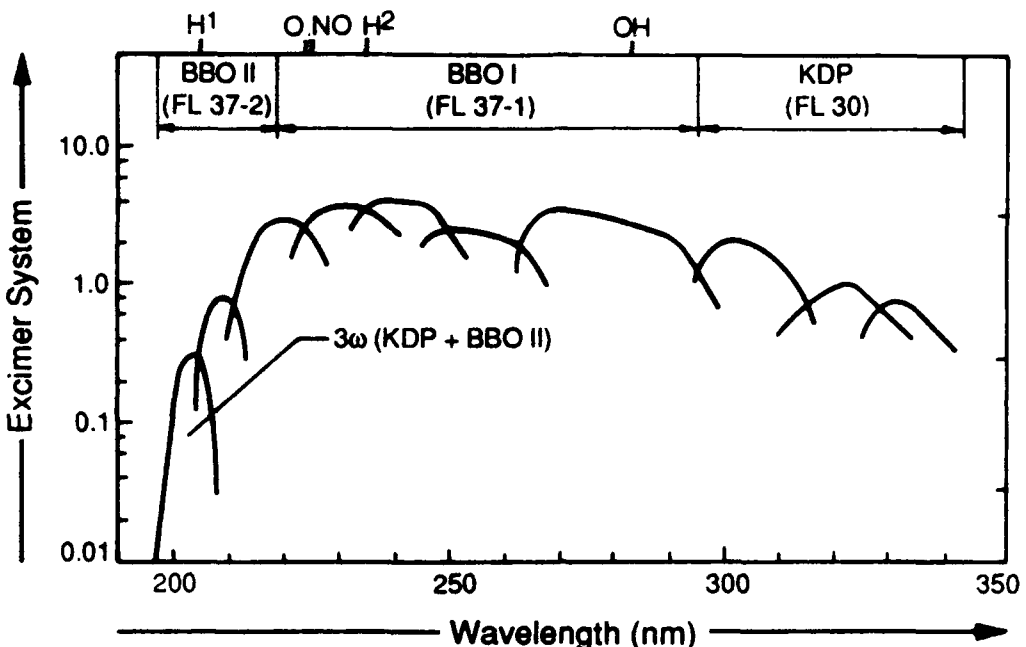


Figure 43

#### Typical Pulse Energies Available From Frequency-Doubled Excimer-pumped Dye Lasers

Model 286e personal computer using a commercially available frame grabber manufactured by Data Translation (Model DT2853). The frame grabber digitized the image on command from an external trigger, thus ensuring synchronization with the pulsed laser and transient shock tunnel flow. For synchronization with the tunnel flow, both the laser and the intensified camera system were triggered using a signal from the first pressure transducer in the shock tube. The PLIF measurement time could be adjusted with internal delays to occur anytime during the tunnel test time.

Fluorescence originating from the laser-excited plane in the flowfield was collected by a Nikon f=105 mm, F/4.5 UV-Nikkor lens and focused through sets of Schott glass filters (depending on the particular experiment) onto the photocathode of an ITT F4111 intensifier

tube. The filters eliminated elastic scattering of the laser sheet from windows and walls within the tunnel. The intensifier was mechanically attached to the camera body and optically connected to the CCD detector array via a tapered fiber-optic bundle.

The CCD array was provided by Phillips (Model NXA1061 array with SSIS video module). The array itself is capable of producing 244 lines each of 604 elements, for a total of 147,376 discrete samples of the fluorescence. The output of the camera is digitized by the frame grabber to fill a buffer of 244 x 512 elements, for a total of 124,928 digitized samples (each sample is digitized to 8 bit accuracy). The readout time of the array is 16.67 ms. The time resolution of the measurement, however, is determined by the length of time in which the fluorescence signal is present, which is defined by the laser pulse duration to be on the order of 10 ns. The intensifier is gated on and off in 1  $\mu$ s, providing discrimination against emitted light from the reacting flowfield itself.

The video output of the CCD array actually consists of two fields, each containing 244 lines of data. In normal video operation, the frame-grabber interlaces these fields to form a composite video image consisting of 488 x 512 elements. For the single-shot experiments in the shock tunnel, only one field contains valid data. The second field contains only integrated dark current and is ignored in data reduction and display. Calibrations of this and similar intensifier tubes at PSI have shown that the gain of the intensifier is sufficient to allow detection of a single photo-electron from the intensifier photocathode. This is the highest sensitivity which can be obtained from any photodetector and permits detection of extremely weak PLIF signals.

The rationale for this choice of detector and data acquisition system is based on the desire to create a high-resolution, sensitive, and inexpensive stand-alone imaging system. A complete survey of the various imaging options is far beyond the scope of this report, but a few salient points are worth noting. First and foremost is the great cost savings associated with using a video format data acquisition system. Because many manufacturers exist for such systems, there is a wide variety of capabilities to choose from and the costs are low compared to other stand-alone imaging systems. The Phillips array is a frame-transfer CCD array combining low noise, high resolution, and high sensitivity. Significantly, it is also available with a fiber-optic faceplate which is coupled to the output window of the intensifier tube via a two-to-one imaging fiber bundle. This fiber-fiber coupling scheme results in approximately one order of magnitude higher transmission efficiency than a lens coupling system.

The PSI-designed intensified camera is a unique and high performance system in several ways. The CCD array sensor, as discussed above, is state-of-the-art, and offers higher resolution, higher sensitivity, and lower noise than arrays available in many prefabricated camera systems. Unlike many commercially available intensified cameras, the PSI design is optimized for scientific, radiometric use with TTL controlled gate and gain features ideally suited to computer control. Finally, no other commercially available system offers the combination of fiber-optic coupling with a detachable intensifier tube. This is an important convenience feature, allowing the same camera to be used with or without the intensifier, with intensifiers of varying spectral response, as well as allowing the intensifier to be easily replaced in the event of a tube failure.

The gain of the intensified camera system is adjustable in two distinct ways: the intensifier gain and the camera gain. The intensifier gain adjusts the voltage across the micro-channel plate (MCP) of the intensifier. The camera gain adjusts the gain of the video preamplifier in the Phillips CCD readout board. The effect of the intensifier gain is to increase the number of photons incident on the CCD detector and is thus a relatively noise-free gain. (Of course, shot-noise generated at the photocathode of the intensifier also experiences gain and the shot-noise-limited signal-to-noise ratio cannot be increased by increasing the intensifier gain.) Hence, it is desirable to take as much gain as possible at this stage.

The camera gain adjust will increase the detector voltage input to the frame-grabber A/D converter. Camera readout noise, intensifier shot-noise, and fixed-pattern variations will also experience gain at this step. The primary purpose of the camera gain is to take the available signal from the CCD array and map it onto the full range of the A/D converter in the frame-grabber. In this manner, the available dynamic range of the converter is fully utilized.

The responsivity of the intensified camera system was measured against the known responsivity of a photodiode at  $\sim 310$  nm using a propane-air torch as a source of UV light (from bright OH A-X chemiluminescence). Figure 44 is a plot of the number of intensifier photoelectrons corresponding to each A/D level in the digitized image as a function of the intensifier control voltage at an optimized camera gain voltage of 4.87 volts. This responsivity can be converted to an absolute photon responsivity by dividing by the quantum efficiency of the intensifier photocathode at the detected wavelength. The wavelength-

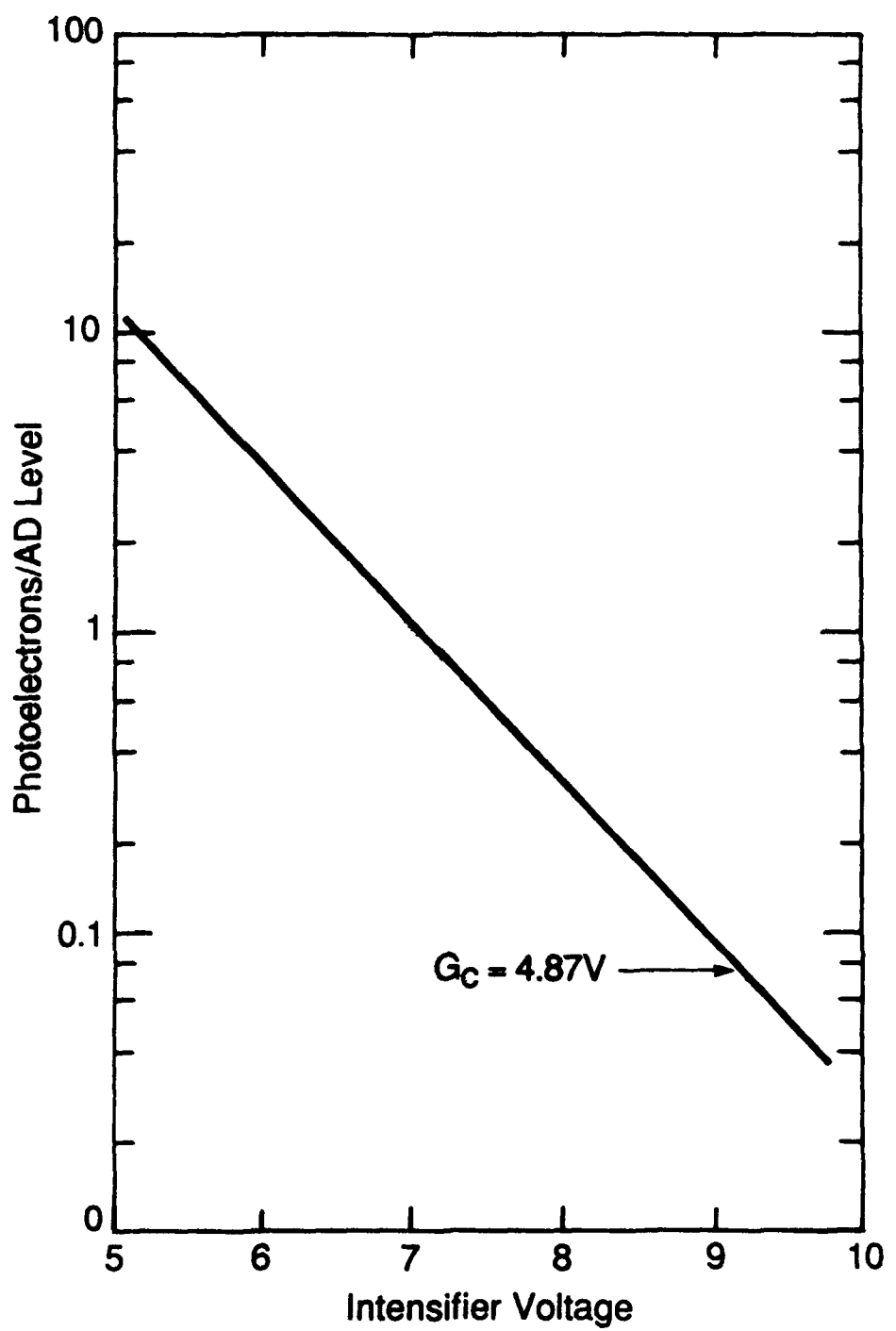


Figure 44  
Responsivity of Intensified Camera System

dependent quantum efficiency is given in Figure 45. Conveniently, the quantum efficiency of the intensifier peaks between 200 and 400 nm, the typical PLIF detection wavelengths.

An extensive software library was created, permitting externally triggered frame acquisition, processing, and display. The raw PLIF images are corrected for the integrated dark current during the exposure period, spatial variations in the responsivity of the detector array, and nonuniformities in the laser excitation sheet in order to yield the true fluorescence distribution. The reduced images are typically displayed using a false-color encoded lookup table which maps each A/D level to one of over 16 million available colors on the image display. Typically, groups of 10 A/D levels (0-9, 10-19, etc.) are displayed with the same

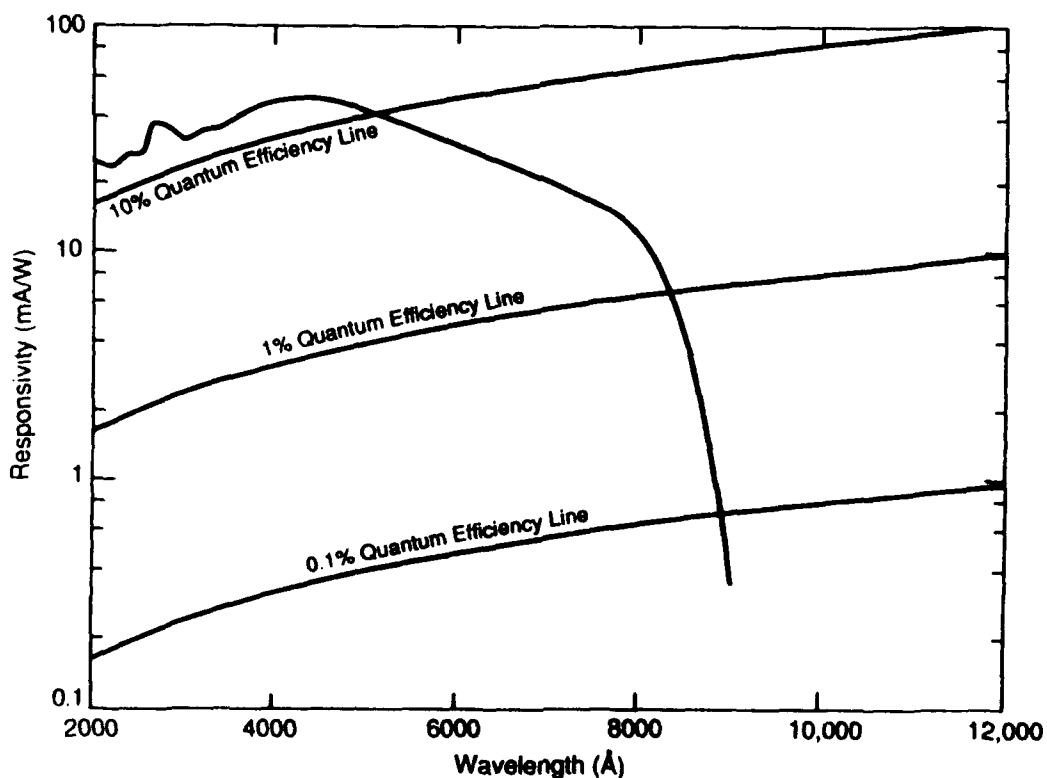


Figure 45

Quantum Efficiency of Intensifier as a Function of Wavelength

color. In all cases, the images are displayed along with their appropriate lookup table, providing a linear reference map of signal levels.

#### **4.6.2 Laser-Induced Fluorescence of NO and OH**

Acquisition of meaningful fluorescence images in any environment requires a carefully developed strategy for laser excitation and data interpretation. In this section, we present the details of the strategies developed in this program for quantitative OH and NO PLIF measurements. Most of the concepts for interpreting LIF signals in compressible, reacting flowfields are first introduced in Subsection 4.6.2.1 which focusses on details of NO fluorescence.

In contrast to the bulk of PLIF diagnostic development, which has been carried out in isobaric, atmospheric pressure flames and flows, the diagnostic strategies developed in this program are tailored to yield meaningful information over a broad range of temperatures (250 to 3000 K), pressures (0.1 to 2 atm), and directed velocities (0 to 200,000 cm/s). Any given PLIF image may traverse regions of widely varying properties. In order to interpret the resulting fluorescence distribution, we must consider variable absorption line widths, velocity-dependent Doppler-shifts of the absorbing lineshape, and pressure- and temperature-dependent energy transfer within the probed molecule. As we will show, careful selection of the excitation and detection strategy can adjust the measurement sensitivity to these varying parameters.

The principal species studied in this program were NO and OH. As has been discussed previously, NO is a logical choice due to its relatively high concentration in the reflected-shock-heated free-stream air. This provides an essentially constant mole-fraction constituent of the air flow (in the absence of fuel-injection) and allows interrogation of temperature (and, ultimately, velocity) fields. We have used it primarily as a measure of the base flow characteristics without injection in both the qualitative (i.e., position and angle of key shocks) as well as quantitative (temperature distributions) sense. The OH radical is a key intermediate in hydrocarbon and hydrogen combustion. In the near injector region, it indicates the position of the stoichiometric fuel/air interface where reactions are occurring. Further downstream, the OH radical is a stable, equilibrium species in the high temperature combustion product gases and can be used to infer the extent of the fuel burning and spreading.

In general, we can express the fluorescence signal viewed by each pixel on the detector array as:

$$S_F = (I_\nu B) \cdot (F_y) \cdot (f_B N_t V_c) \cdot \left[ \eta \frac{\Omega}{4\pi} \right] \quad (19)$$

where:

- $I_\nu$  = laser spectral fluence
- $B$  = Einstein B coefficient for absorption
- $F_y$  = fluorescence yield
- $f_B$  = Boltzmann population fraction
- $N_t$  = species number density

$V_c$	=	collection volume
$\eta$	=	filter transmission, detector responsivity, etc.
$\Omega$	=	collection solid angle of imaging system.

The first parenthetical term is the probability that an absorption event will occur. It depends on the local laser energy (which, in general, varies across the laser sheet) and the Einstein B-coefficient (which is constant for a selected transition). The second parenthetical term is the probability that an absorption event will result in a fluorescence photon. In general, it is the ratio of the radiative decay rate over all possible decay rates of the laser excited state. The exact form of the expression for the fluorescence yield thus depends on the particular strategies employed for a given molecule and will be discussed in the following sections for NO and OH. The third parenthetical term is the number of absorbing molecules in the volume defined by the intersection of the pixel field of view and the laser sheet thickness. The Boltzmann fraction,  $f_B$ , expresses the fraction of the total molecular population,  $N_t$ , resident in the isolated energy level (or levels) accessed by the laser. For a given level,  $f_B$  depends only on fixed spectroscopic parameters and the local gas temperature. The final term is the efficiency with which the fluorescence photons, emitted into all directions, are collected by the imaging optics and focussed onto the detector array.

Equation (19) is the basic formula used to reduce the fluorescence data collected during this program to concentration, mole-fraction, or temperature. In the following sections, the terms in Eq. (19) are expanded and tailored for the specific approaches developed here.

4.6.2.1 NO Fluorescence. The approach for laser-induced NO fluorescence pursued in this program can best be understood by reference to Figure 46, a partial energy level diagram for NO. The figure shows schematically the ground  $X^2\Pi$  electronic state and the first excited electronic state,  $A^2\Sigma^+$ . In the ground electronic state, the first seven vibrational levels are shown. Each vibrational level also contains a manifold of rotational levels which are shown schematically in  $v'' = 0$ .

The vertical arrow at the figure left represents the energy available from a photon near 226 nm (derived from the laser). The laser wavelength is tuned to correspond to the energy of a transition from an isolated rotational level in the ground vibrational level of the lower

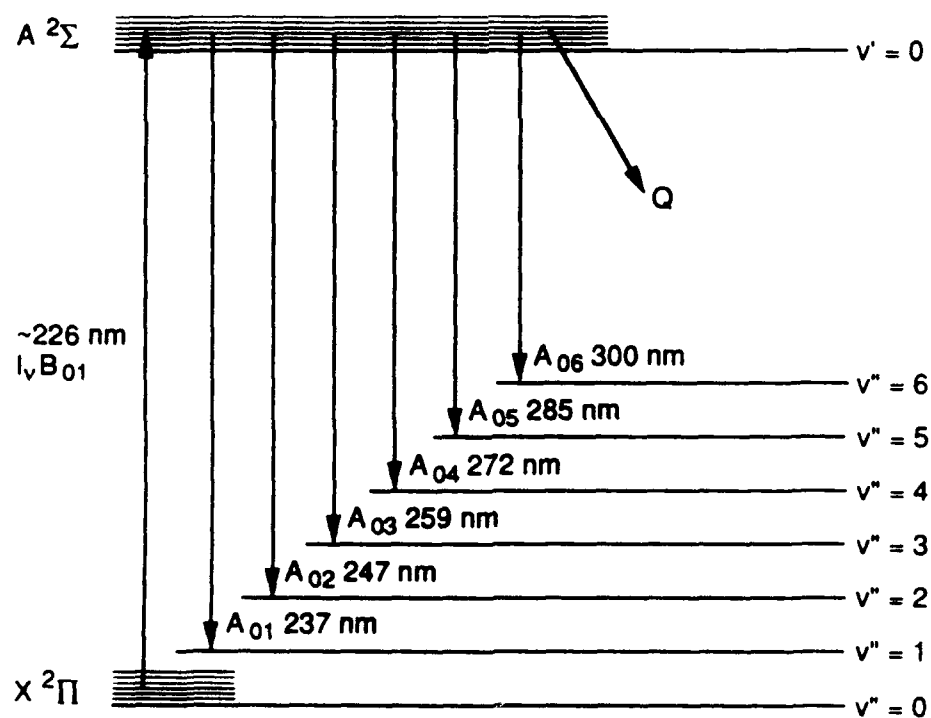


Figure 46

Schematic Energy Level Diagram Showing Important Processes in  
Laser-Induced NO Fluorescence

electronic state upward to an isolated rotational level of the ground vibrational level in the upper electronic state. These rotational transitions are conventionally referred to as (0,0) band transitions, denoting the vibrational quantum numbers of the upper and lower state, respectively.

Molecules elevated to the upper electronic state may transfer to nearby rotational levels or back to the ground electronic state (the latter process is termed quenching) by collisions with neighboring molecules. The quenching rate is denoted by  $Q$ . Spontaneous radiative decay competes with the collisional decay through all the allowed transition pathways from the excited state, giving rise to the fluorescence signal. Transitions from the upper electronic state to the various vibrational levels in the lower state are denoted by  $A_{(0,i)}$ , where  $i$  represents the quantum number of the lower vibrational level.

Transitions on these off-diagonal bands shift the fluorescence to longer wavelengths and permit spectral isolation of the weak fluorescence from the laser wavelength. The total effective radiative transfer rate is given by:

$$A_{\text{eff}} = \sum_i (T_{\lambda i} A_{(0,i)}) \quad (20)$$

where  $T_{\lambda}$  is the filter transmissivity at wavelength  $\lambda$ . The relative overlap of the filter transmission curve (Acton Research Corporation 254 filter + 2 mm Schott UG-5 filter glass) is shown schematically in Figure 47, where the relative height of the arrows indicates the relative transition strength,<sup>17</sup> and the solid line is the measured filter transmission. The effective radiative rate is only about 5 percent of the total radiative rate, but strong rejection

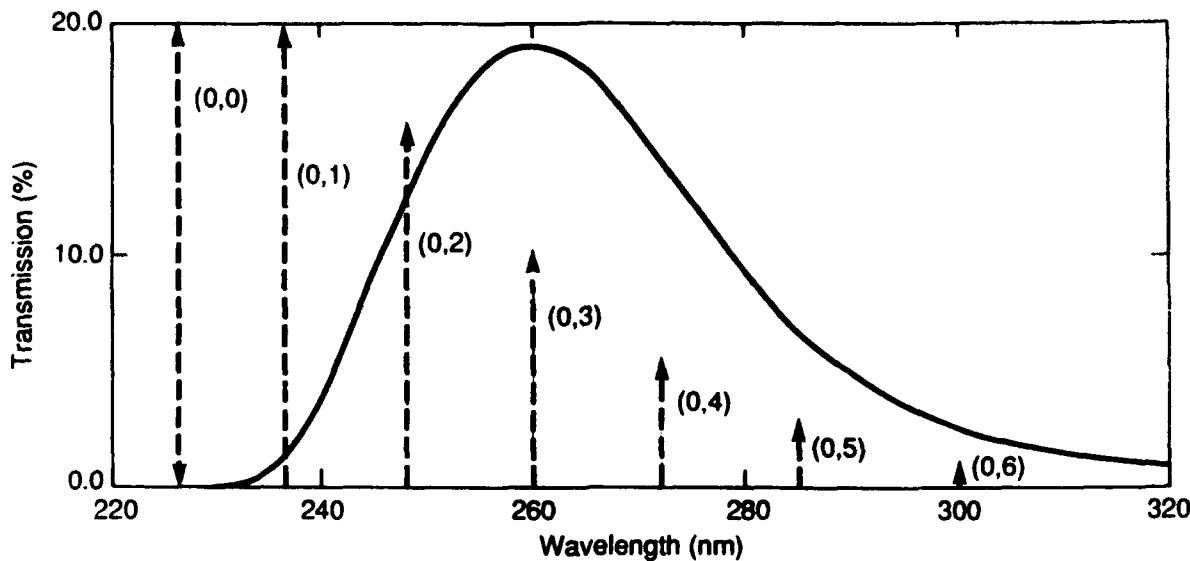
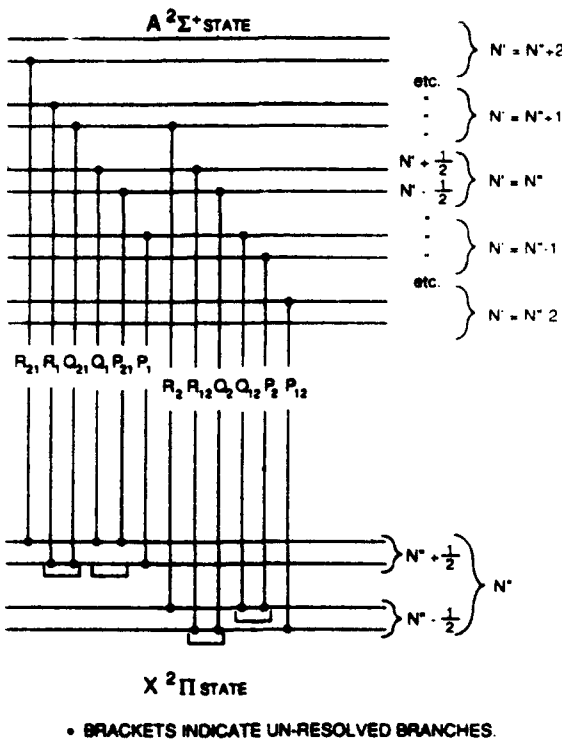


Figure 47

#### Effective Radiative Transition Rate for NO Fluorescence Strategy

of the laser wavelength is important in practical measurements. As we will demonstrate, imaging of the NO fluorescence all the way to the steel tunnel floor was possible without scattering interference from the directly impinging laser sheet.

Details of the rotational level structure in the upper and lower electronic states, along with the convention used throughout this work in labelling the rotational branches is shown in Figure 48. Each rotational level of the upper state is spin-split into two components labelled  $N' + 1/2$  and  $N' - 1/2$ , where  $N'$  refers to the rotational quantum number. Each rotational level in the lower state is split by a coupling of the electronic spin and orbital angular momentum and each spin-orbit level is further split by lambda-doubling, resulting in four levels for each  $N''$ . The spin splitting in the upper state is less than 3 GHz for the highest  $N''$  transitions used in this work which is less than the transition Doppler width.<sup>18</sup> Hence,



**Figure 48**

**Rotational Branches of NO A-X Transitions**

transitions originating from the same lower level and terminating in each of the two spin components of the upper state are unresolved and are grouped together with brackets in Figure 48. The transition labelling employed here follows that used by Earls<sup>19</sup> for intermediate Hunds' case in the ground electronic state.

For this NO excitation/detection strategy, the fluorescence yield may be written as:

$$F_Y = \frac{A_{eff}}{A_{v'=0} + Q} \quad . \quad (21)$$

In general, the quenching term is written as:

$$Q = \sum_i (N_i \sigma_i v_i) \quad (22)$$

where:

$N_i$  = number density of collision partner  $i$

$\sigma_i$  = cross section

$v_i$  = mean molecular velocity.

The sum is over all available quenching partners and the cross-sections may vary with the upper state rotational level. For NO in air flows, however, two important simplifications are valid. Firstly, neither the effective radiative transition rate nor the quenching rate is a function of rotational quantum level in NO A  $^2\Sigma^+$ .<sup>20</sup> Hence, the effective radiative transition rate is determined only by the collection filter transmission function and is not a function of pressure- and temperature-dependent energy transfer rates in the upper manifold. Secondly, for air flows, the sum in Eq. (22) is dominated by the large O<sub>2</sub> cross-section, which is independent of temperature over the range of temperatures studied here.<sup>21</sup>

Hence, we may express the quenching term as:

$$Q = \text{constant} \cdot P \cdot T^{-1/2} \quad (23)$$

where we have gathered together the temperature and pressure dependencies of  $N_i$  and  $v_i$ .

For the nominal 0.3 atm, 1400 K air free-stream flows, the total NO quench rate is approximately  $7 \times 10^7 \text{ s}^{-1}$  and scales with temperature and pressure according to the above.

In combustion or other water vapor-laden flows, the large, temperature dependent cross-section of H<sub>2</sub>O would have to be included in the calculation of the overall quench rate.<sup>21,22</sup>

The total radiative transfer rate from v' = 0 is 5 x 10<sup>6</sup> s<sup>-1</sup> so that, for pressures greater than 0.1 atm, A<sub>v'=0</sub> < < Q. Hence, the fluorescence yield may be written as:

$$F_y = \frac{A_{eff}}{Q} \sim \frac{T^{1/2}}{P} . \quad (24)$$

Using the ideal gas relation:

$$N_t = \chi_i P/RT \quad (25)$$

where  $\chi_i$  = the mole-fraction of NO in the air flow. Gathering together the pressure and temperature dependence of the fluorescence yield and NO number density, we can express the fluorescence equation presented as Eq. (19) as:

$$S_F = \text{constant} \cdot \chi_i \cdot T^{-1/2} \cdot f_{B(T)} \quad (26)$$

where the constant is a function of laser pulse energy, spectroscopic parameters, and fluorescence collection efficiencies. Variations in the fluorescence signal within an image are only a function of mole-fraction variations (due to chemical reactions) or temperature (with or without chemical reactions).

Equation (26) is an important result for the present study. Recall that NO is formed with  $\chi_i \sim 2$  to 5 percent in the high temperature, high pressure reflected shock plenum. For the convective time from the nozzle throat to the PLIF image planes near the primary injectors, the NO is chemically frozen at this super-equilibrium level as the gas expands. Thus, the

PLIF image plane contains (in the absence of fuel injection and burning) a constant mole-fraction of NO with bulk fluid temperature variations due to the Prandtl-Meyer expansion over the rear-facing step, recompression shock from the tunnel floor, and other flow features. *Bulk pressure variations will not influence the PLIF signal.*

The temperature sensitivity of the fluorescence signal may be tuned by selecting various ground state rotational levels and exploiting the varying temperature dependence of the Boltzmann population fraction. For example, by choosing a level which increases in population fraction by  $\sim T^{1/2}$ , the PLIF image will be sensitive only to variations in the mole-fraction of NO. Changes in the mole-fraction reflect the results of chemical reactions in the flowfield. The resultant image will not be sensitive to bulk temperature and pressure variations caused by the compressible flow physics; rather, it will reveal variations due to chemistry. Alternatively, a rotational level may be chosen which accentuates the temperature dependence of the fluorescence signal. For the NO PLIF measurements in this work, the NO mole-fraction was essentially constant over most of the image and this latter strategy was selected in order to maximize our sensitivity to the fluid dynamic temperature variations in the image plane.

Temperature, pressure, and flow velocity may also indirectly affect the excitation fluorescence excitation efficiency, the first parenthetical term in Eq. (19). The formally more accurate expression for the excitation efficiency (or rate, with units  $s^{-1}$ ) is:

$$\text{Pump Rate} = B \int_{\omega} I(\omega) g(\omega) d\omega \quad (27)$$

where  $g(\omega)$  is the absorption lineshape function. Since the probability of transition must be unity over an entire transition lineshape:

$$\int_{\omega} g(\omega) d\omega = 1 \quad . \quad (28)$$

In writing Eq (28), we have assumed that the laser spectral fluence is a "top-hat" profile in frequency, broader than and constant over the entire absorption lineshape so that

$$I_B = B \int_{\omega} I(\omega) g(\omega) d\omega \quad . \quad (29)$$

This situation is illustrated in Figure 49. In the figure,  $\omega_A$  is the center frequency of the absorption lineshape with full-width at half-maximum (FWHM) of  $\Delta\omega_A$ . Similarly, the laser bandwidth is shown as  $\Delta\omega_L$  centered at  $\omega_L = \omega_A$ . In actuality, the laser spectral fluence exhibits a different functional form, usually assumed to be a Gaussian with a FWHM  $\Delta\omega_L$ .

As long as the laser bandwidth substantially exceeds the absorption lineshape bandwidth, the assumption of Eq. (29) is a reasonably valid one. As the absorption lineshape broadens, this assumption becomes less accurate, although, even for equal bandwidths, the product of the laser lineshape and absorption lineshapes in the wings of the profiles contributes a small portion to the entire functional product. Typically, the assumption is reasonable as long as

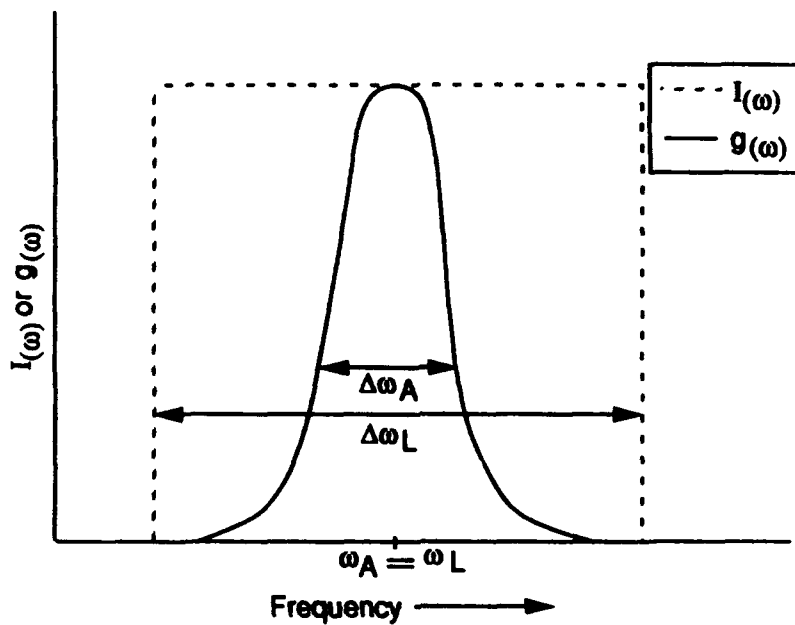


Figure 49

#### Schematic Diagram of Top-Hat Laser Profile and Absorption Lineshape Overlap

the laser bandwidth is on the order of or larger than the absorption linewidth. If the absorption linewidth begins to exceed the laser linewidth, however, the excitation efficiency and, hence, the fluorescence signal, becomes sensitive to changes in the absorption lineshape in the flowfield.

Under most conditions relevant to this study and supersonic combustion in general, the absorption lineshapes will be described by a Voigt function, containing contributions from the Doppler (thermal) broadening mechanisms as well as collisional broadening mechanisms. The Doppler width is easily calculated using the formula:

$$\Delta\omega_D = 2 \left[ \frac{2k T \ln 2}{mc^2} \right]^{1/2} \omega_A \quad (30)$$

and is a function of temperature alone. The collision width reflects the local collision environment and is more difficult to calculate. It is dependent on the composition of the surrounding gas, the overall gas pressure, and temperature. The pressure and temperature dependence is usually separated by expressing the collision width as:

$$\Delta\omega_c = \frac{1}{2\pi c} \sum_i \gamma_i P_i \quad (31)$$

where  $\gamma_i$  is the temperature-dependent broadening parameter and  $P_i$  is the partial pressure of species i. The sum is over all available collision partners. To first order, the temperature and pressure scaling of the collision width is the same as the electronic quenching.

The total absorption linewidth is approximately:

$$\Delta\omega_A \approx [\Delta\omega_D^2 + \Delta\omega_c^2]^{1/2} \quad (32)$$

Thus, the absorption lineshape will expand or contract with temperature and pressure variations in the flowfield. If the laser bandwidth is comparable to or smaller than the absorption bandwidth, the fluorescence signal will also vary with temperature and pressure due to changes in the excitation efficiency expressed in Eq. (27).

Lastly, the absorption lineshape may be shifted in frequency by changes in pressure or velocity. The pressure shift is given by:

$$\Delta\omega_s = \beta \Delta\omega_c \quad (33)$$

where, for NO,  $\beta = -0.303$ .<sup>23</sup> The velocity shift is given by:

$$\Delta\omega_v = \frac{u}{c} \omega_A \quad (34)$$

where  $u$  is the component of the velocity vector aligned with the laser beam propagation direction.

Table 10 summarizes these linewidths and shifts. In the case of the absorption linewidths, the largest values expected in the flow are reported. For the shifts, the maximum variation across an image is given. In each case, the absorption linewidths and shifts are small compared to the laser linewidth so that the excitation efficiency is not a function of pressure or temperature. In colder, higher pressure flows, however, the absorption linewidth and collisional shifts will be much larger and may be an important factor in interpreting the PLIF images.

In order to identify well isolated transitions to be used in the shock tunnel experiments as well as to calibrate the dye laser wavelength, a series of excitation scans were conducted in a static cell, according to the setup shown in Figure 50. The laser light was directed through a cell (unfocused) in which various pressures of air and NO could be introduced. The laser was operated at repetition rates between 10 and 60 Hz. Fluorescence was collected with a Hamamatsu R/955 PMT and averaged over 10 to 30 laser pulses using a SRS Gated Integrator and Boxcar Averager. The laser scan time was adjusted so that the laser

Table 10. Linewidths and Shifts for NO Fluorescence

$\Delta\omega_L$	=	0.75 cm <sup>-1</sup>
$\Delta\omega_C$	=	0.067 cm <sup>-1</sup>
$\Delta\omega_D$	=	0.22 cm <sup>-1</sup>
$\Delta\omega_S$	~	0.01 cm <sup>-1</sup>
$\Delta\omega_V$	~	0.04 cm <sup>-1</sup>

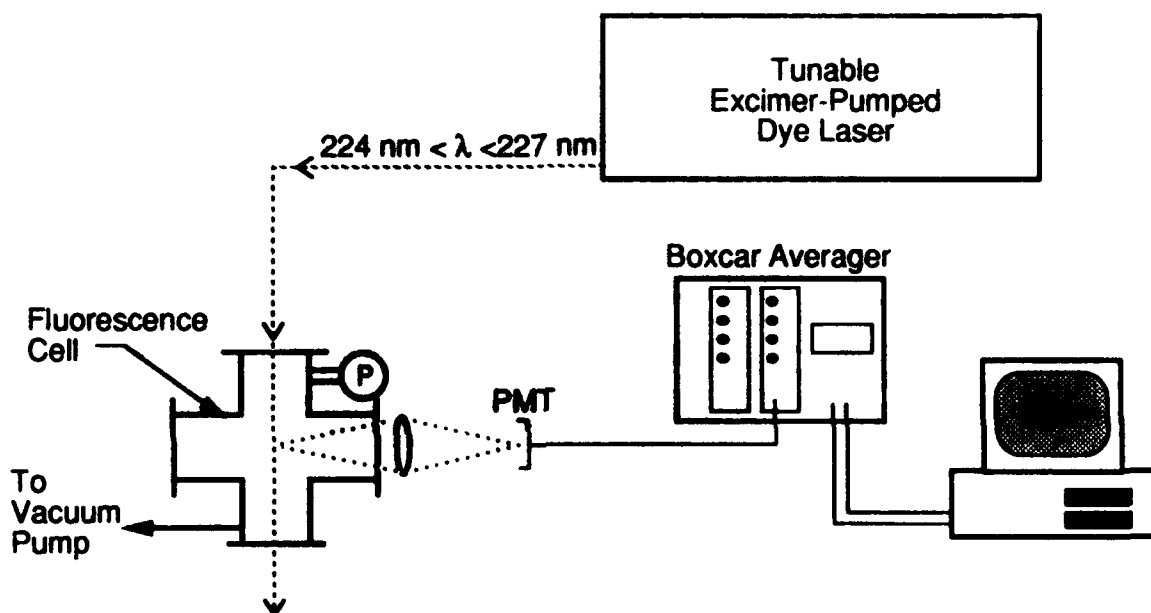


Figure 50

Experimental Setup for Pulse Laser Excitation Scans

wavelength was stationary during the 1 to 3s integration time of the boxcar averager. The averaged fluorescence signal was recorded on a laboratory computer.

An example of the data obtained in these experiments is shown Figure 51, a portion of a room temperature excitation scan taken at P < 1 torr in a sealed cell. The P<sub>12</sub> bandhead at 227 nm is labelled, along with portions of the P<sub>2</sub> (P<sub>22</sub> + Q<sub>12</sub>), Q<sub>2</sub> (Q<sub>22</sub> + R<sub>12</sub>), and R<sub>2</sub>

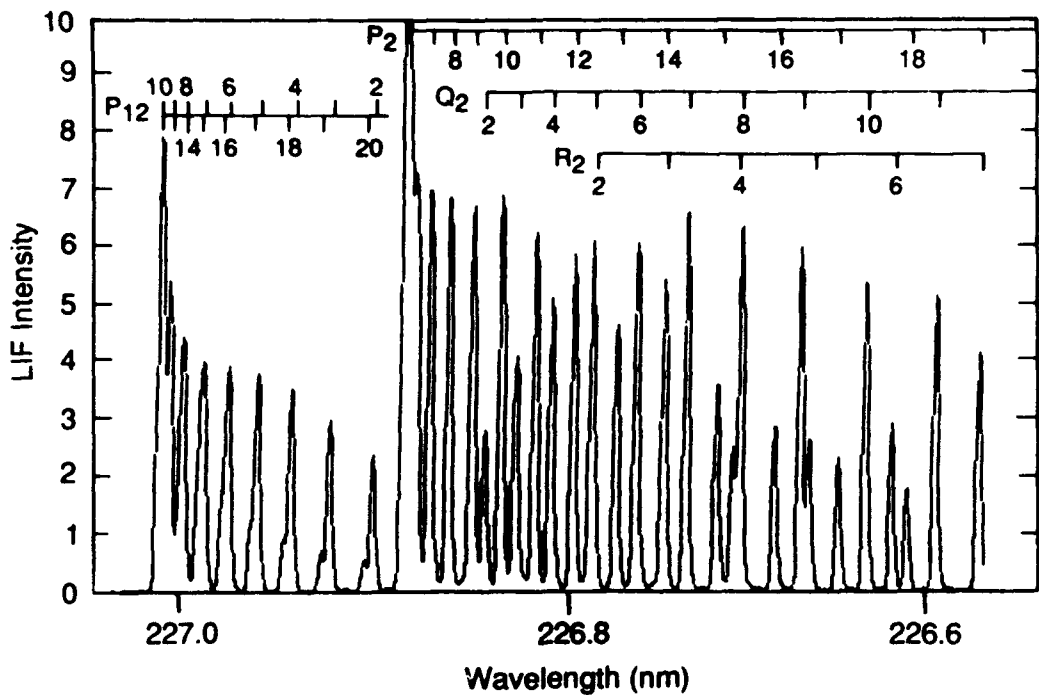
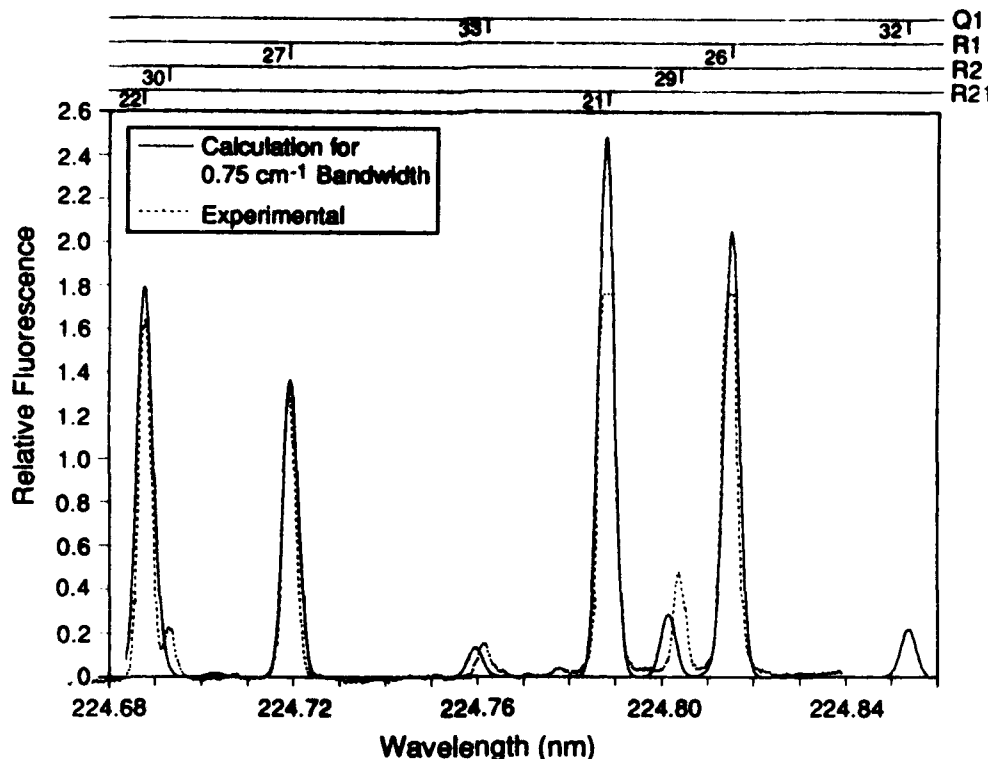


Figure 51

#### Room Temperature NO Pulsed Laser Excitation Scan

branches. The linewidths of these fluorescence features are largely determined by the laser linewidth since the inherent Doppler width at 300 K is  $\sim 0.1 \text{ cm}^{-1}$ . A more detailed portion of the spectrum is shown in Figure 52, showing the region between 224.68 and 224.84 nm. The figure shows room temperature data in the dashed line along with a predicted spectrum for a  $0.75 \text{ cm}^{-1}$  bandwidth Gaussian laser profile. The spectral agreement for the lower  $N''$  values is excellent because the computer simulated spectrum uses observed line positions where available. At higher rotational quantum numbers, the spectral simulation code predicts transition wavelengths using a Dunham coefficient expansion which is accurate to about 1/3 of the convolution linewidth. From the fit, and a similar fit taken with 1 atm background air pressure to check for possible saturation effects, the mean laser bandwidth was determined to



**Figure 52**

**NO Excitation Scan Detail - 300 K.**

be  $0.75 \text{ cm}^{-1}$ , in good agreement with the dye laser specifications. Similar scans were taken throughout the A-X system in order to verify the transition accessed by the laser.

In the calibration experiments, the laser was tuned to the  $Q_2(7)$  transition at 226.72 nm and focussed into a  $2.7 \text{ cm} \times 0.1 \text{ cm}$  sheet across the central plane of the flow at the exit of the expansion nozzle. In this region, we expect a uniform temperature, pressure, and velocity flow with a particular (to be determined) concentration of NO. The PLIF image through the viewing window was  $6.3 \times 4.8 \text{ cm}$  and showed a fluorescence ribbon, uniform in the flow direction, with a decreasing intensity along the ribbon. The decrease in intensity was due to absorption of the laser beam as it traversed the NO-laden gas. This laser

absorption was reflected in the fluorescence distribution by its impact on the laser excitation efficiency. The absorption for a unit frequency interval is described by Beer's Law<sup>24</sup>:

$$(I/I_0)_\omega = \exp [-k_\omega P_i L] \quad (35)$$

where:

$(I_0)_\omega$  = incident laser intensity at frequency  $\omega$

$k_\omega$  =  $k g(\omega)$ ,  $k$  = line strength of transition

$P_i$  = partial pressure of absorbing species.

To calculate the observed fluorescence attenuation resulting from this absorption effect, it is necessary to calculate the absorption at discrete frequencies under the overlapped laser spectral bandwidth and absorption bandwidth so as to determine the integrated reduction in the laser excitation efficiency at a given increment in path length. Figure 53 shows the results of such a calculation for an 8 cm path length with an assumed NO number density of  $3.2 \times 10^{17} \text{ cm}^{-3}$  at 1400 K and 0.3 atm. The relative PLIF signals at the top and bottom of the 4.8 cm image are shown as well. Since the flow temperature and pressure are reasonably well known from shock speed calculations, this procedure can be used to fix the NO number density with *no knowledge of the absolute magnitude of the PLIF signal itself, nor any details of the quenching environment.*

The absolute magnitude of the PLIF signal at the top of the image, where the laser absorption effect is minimal, provides the more usual means of determining the NO mole-fraction or, since the pressure and temperature across the image are constant, number

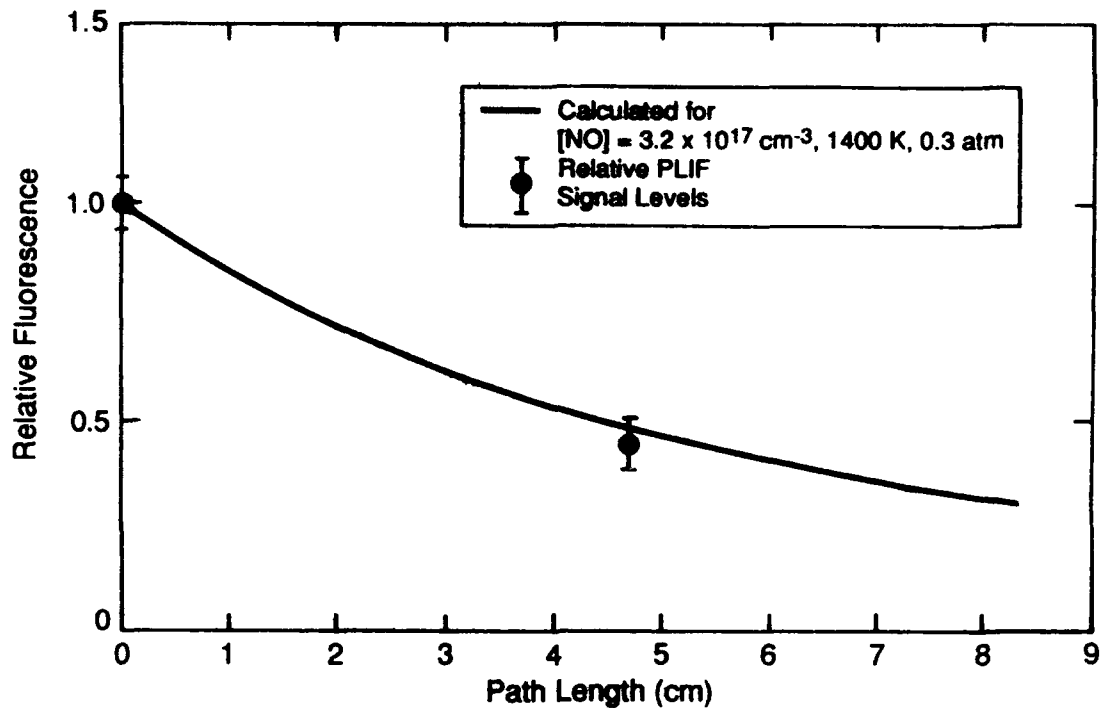


Figure 53

Calculated and Measured Fluorescence Attenuation at Nozzle Exit Plane

density. Using the absolute photometric calibration of the detector system, the maximum PLIF signal levels at the top of the image correspond to about 2800 photons/pixel. Using Eq. (19), the measured laser energy distribution, and spectroscopic and energy transfer parameters developed above, this photon flux corresponds to an NO number density approximately  $2 \times 10^{17} \text{ cm}^{-3}$ , in excellent agreement with the laser attenuation measurement.

As discussed earlier, both of these measurement are in excellent agreement with the independent NO emission measurement as well as calculated reflected shock plenum conditions and NO production there. We take this agreement to indicate that our models of the NO fluorescence process are valid and that our procedure for absolute and relative data reduction is sound.

The remaining measurements of NO PLIF distributions were made in the first PLIF imaging station downstream of the rear-facing step (see Figure 65). In each case, the field of view (limited by the clear aperture of the laser access window on the top of the tunnel) was 3.8 x 2.9 cm. Two representative PLIF images are presented in Figures 54 and 55. Note that the photographic reproduction of the PLIF image varies somewhat between the two figures, although the field of view is the same. In these and all PLIF images in this report, the bottom of the image corresponds to the bottom of the flow tunnel. Also, the color lookup table used to map the digitized A/D levels to display colors is different between the two images. The scale of color mapping to the 256 level A/D range is indicated in each figure and the fluorescence intensity mapping is linear.

In Figure 54, the flowfield consists of the simple expansion over the step with no injection, as described in Figure 23. In this series of experiments, the laser was tuned to the  $Q_{22} + R_{12}(7)$  transition at 226.72 nm. The  $N'' = 7$  level has a negative temperature dependence over the range in the flow so that the temperature sensitivity of the PLIF image is enhanced. The left side of the image is defined by the upstream edge of the laser sheet which does not correspond to the edge of the imaged region. In initial testing, the tunnel apparently moved a few millimeters during firing and it was not possible to exactly position the fixed camera with respect to the tunnel.

The absolute signal levels in the free stream (at the upper left corner of the image) correspond to the nominal flow condition of 1500 K, 0.3 atm, and  $\sim 1 \times 10^{17} \text{ cm}^{-3}$ . The fully expanded flow is in the lower left corner of the image and the signal levels there are



Figure 54

NO PLIF Distribution Without Injection

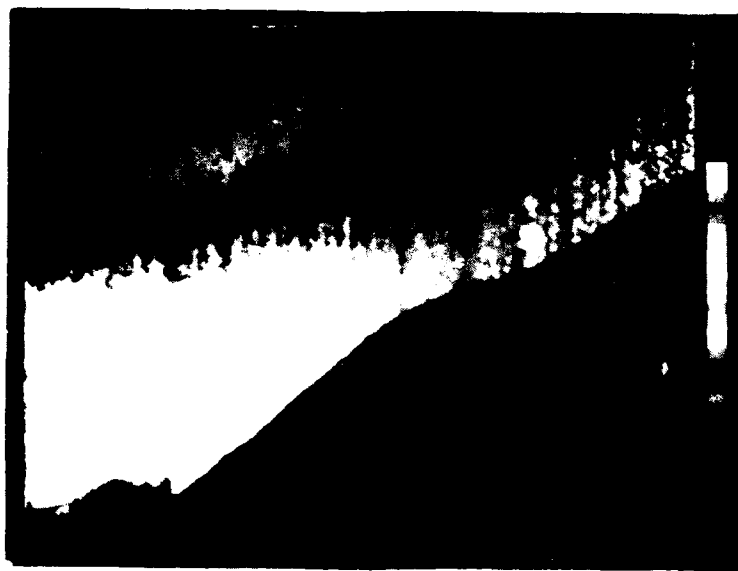


Figure 55

NO PLIF Distribution With Injection

approximately 1.5 times greater. The recompression shock is clearly visible, initially straight, then curving slightly through the non-uniform flow region. The signal level across the recompression shock is about 33 percent of the level in the fully expanded flow due to the higher temperature there, and about 60 percent of the signal level in the free-stream.

The dark band across the center of the image was a persistent feature in each of the images acquired during this first series of PLIF experiments and was not expected from our flowfield predictions. It was subsequently determined that this band was due to a cloud of particulate remaining from the shock tube driver fabrication which was lifted as a jet along the tunnel floor during early flow times. The fluorescence signal is diminished where the particulate jet occurs due to extinction of the fluorescence as it propagates across the flow toward the imaging detector. The laser sheet is undoubtedly diminished somewhat, as well, but since the extinction path length for the laser is much smaller than that for the fluorescence ( $\sim 1$  cm versus  $\sim 4$  cm), the effect is reduced and fluorescence can be viewed below the jet. Cleaning of the tunnel and a change in operational procedures removed this effect and subsequent data are free from this interference.

Figure 55 is an image of the same plane in the flow, now with helium injection. In this image, the  $R_{11} + Q_{21}(13)$  transition was excited, providing slightly higher signal levels while preserving the temperature sensitivity. In this image, free from particulate interference, the contours of the Prandtl-Meyer expansion fan, made visible by the decreasing temperature are clearly visible. The fan lines terminate beyond the left side of the image at the downstream edge of the step. The highest signal levels, again, occur in the fully

expanded flow at the lower left portion of the image. A portion of the raw fluorescence image near the center of the image was saturated during the experiment. This was due to the relatively higher laser energy in the central part of the sheet. During the correction procedure for the laser energy variation, these data were naturally corrupted since their actual signal levels were beyond the maximum level of the A/D converter. The vertical stripes at this location reflect the small variations in laser sheet intensity imposed upon the artificially constant signal data and should be ignored. This nonideal image performance is a typical consequence of the single-shot nature of the shock tunnel experiments.

The injection substantially modifies the remainder of the downstream flowfield. Rather than a recompression shock, the injectant gas sets up a strong bow shock in the flow. The fluorescence signal across the bow shock immediately decreases due to the higher temperature there. Along the flow streamlines, it decreases further, eventually disappearing, as the NO mixes with the helium injectant. Downstream of the bow shock, the NO is no longer a constant mole-fraction constituent of the gas and the PLIF image reflects the combined effects of temperature variations and mixing. In this region the PLIF image is a qualitative visualization of the injectant mixing. Interestingly, the lower left corner of the image reveals a sharp boundary between the expanded flow (high signal levels) and the entrainment of the injectant gas into the recirculation zone (low signal levels).

A summary of the temperature dependent PLIF signal in three experiments without injection and one experiment with injection is presented in Figure 56. In the figure, the calculated fluorescence signal dependence with temperature for the two transitions employed is plotted

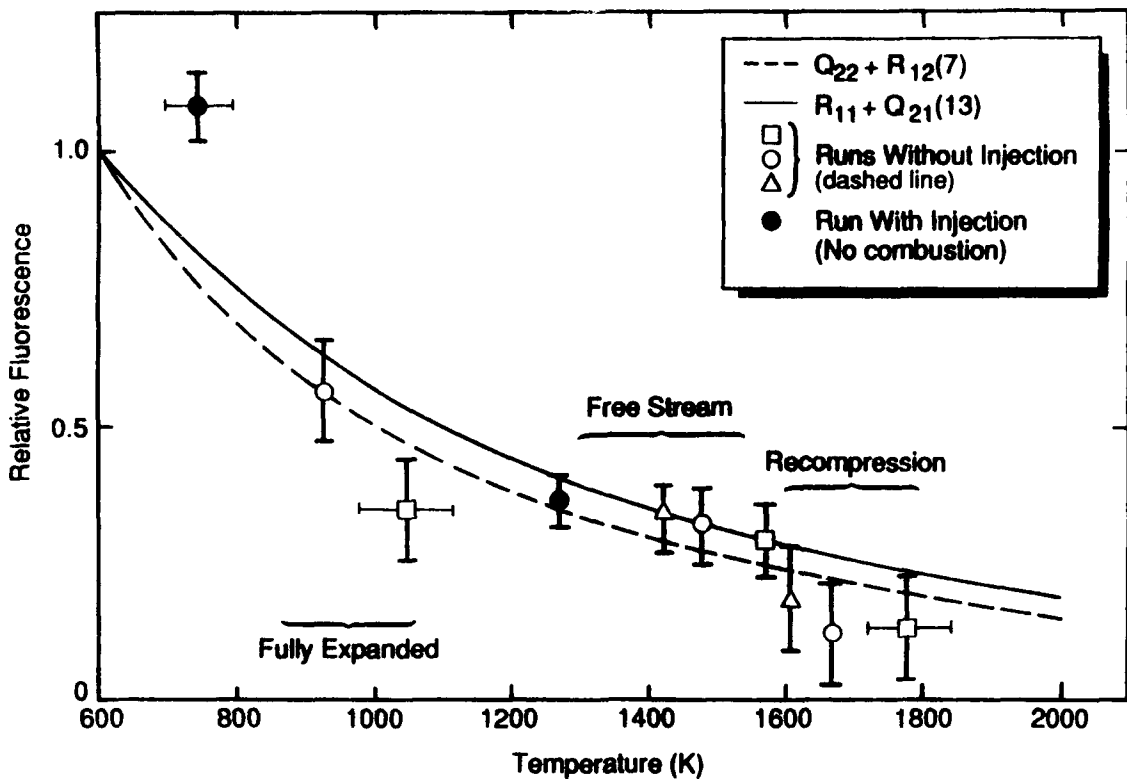


Figure 56

#### Comparison of Predicted and Measured NO PLIF Signal Variations With Temperature

as the dashed and solid lines. The open symbols show the typical signal levels from the three uniform flow regions of the flowfield with no injection: free stream, fully expanded, and recompression. The closed symbols show the typical signal in the two uniform flow regions of the flowfield with injection: free stream and fully expanded. The data points could be placed on this figure in several ways. If the exact temperature were known anywhere in the flowfield, the data points corresponding to that region, say, the free stream, could be fixed on the appropriate model curve. In the current experiments, however, the uncertainty in the free stream temperature is several hundred degrees, so we choose to plot the PLIF data points assuming that the ratio of the temperatures in the various regions

predicted by the simple inviscid model was exact, but the absolute value of the temperatures was uncertain. The open symbols were plotted to give the best agreement with the curve in all three regions of the flow and generally predict a free stream temperature approximately 1500 K, some 100 K higher than the nominal NO emission temperature. The closed symbols suggest a free stream temperature of 1300 K. As discussed in Subsection 4.4, variations in the apparent flow temperature of this amount were common and our procedure seems reasonable.

The angle of the expansion fan in the PLIF data is 19.5 degrees, identical to the calculated angle of 19.5 degrees. Although the postbow shock data reflects mixing and temperature effects, it is likely that the flow immediately downstream of the bow shock has not substantially mixed with the injectant flow. The signal ratio across the shock from the fully expanded flow indicates a temperature of 1700 K. This is a somewhat higher ratio than in the experiments with no injection, but is reasonable since the strength of the bow shock (as reflected by the flow turning angle) is stronger.

The NO PLIF temperature data is in agreement with the trends predicted by the model, but the existing database is too small to justify strong claims regarding the ultimate accuracy of our approach. In the experiments without injection, the signal levels in the fully expanded region and the recompression region are somewhat lower with respect to the free stream flow than expected. This is at least in part explained by the laser sheet extinction in the particulate jet. In the single experiment with injection, the fully expanded temperature, as measured by the PLIF data, appears lower than we would expect ( $\sim 550$  K). At this point,

it is not clear whether this discrepancy is systematic or a random error in this individual measurement. The overall trends of the data, however, are correct and the PLIF image clearly reveals structure of the flow that could not otherwise be observed and strongly demonstrate the potential for quantitative PLIF measurements in high temperature, high pressure, supersonic flows.

**4.6.2.2 OH Fluorescence.** The strategy developed for OH fluorescence measurements is summarized in Figure 57, partial energy level diagram for OH. The figure shows schematically the ground  $X^2\Pi$  ground electronic state and the first excited electronic state,  $A^2\Sigma^+$ . Note that the electronic states in OH are the same structure as those of NO. Thus, the spin-splitting and rotational transition labelling are similar and will not be repeated here. Embedded vibrational and rotational energy levels are indicated.

The vertical arrow at the figure left represents the energy available from a photon near 283 nm. The laser wavelength is tuned to correspond to a transition from an isolated rotational level in the ground vibrational level of the lower electronic state upward to an isolated rotational level of the first excited vibrational level in the upper electronic state. These rotational transitions are conventionally referred to as (1,0) band transitions, denoting the vibrational quantum numbers of the upper and lower state, respectively.

Once in the upper electronic state, various collisional processes transfer population to other rotational levels ( $R_{(N)}$ ) or to the ground vibrational level ( $V_{(N)}$ ) within the upper electronic state. Collisional quenching ( $Q_{(N)}$  and  $Q'$ ) can remove population completely from both

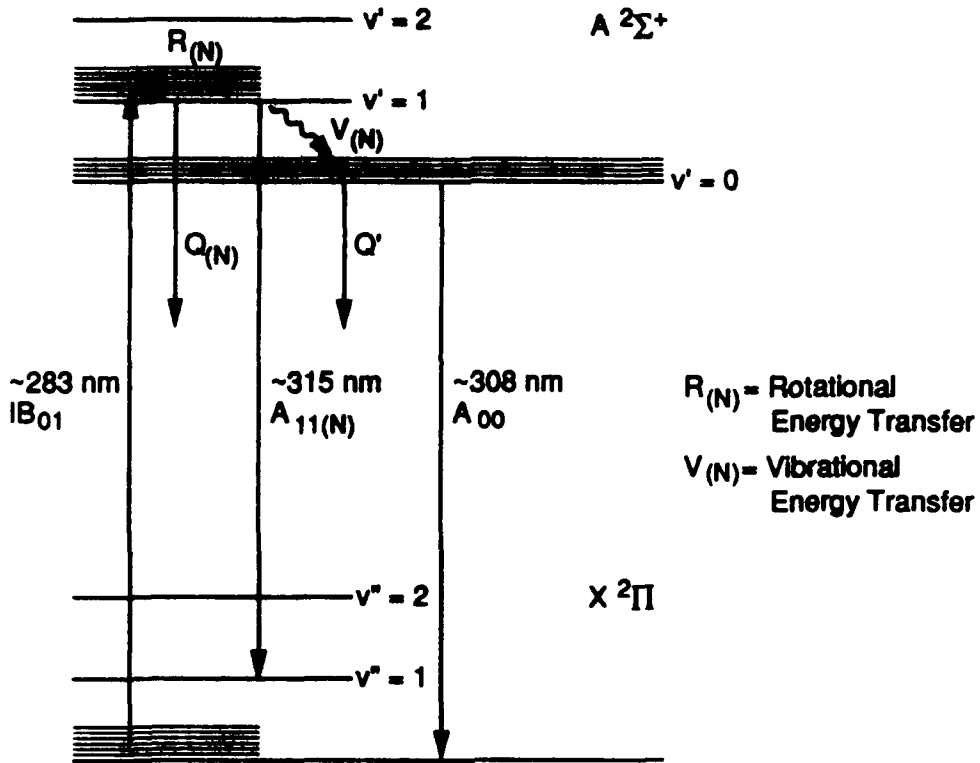


Figure 57

Schematic Energy Level Diagram Showing Important Processes in Laser-Induced OH Fluorescence.

vibrational levels in the upper state. The fluorescence signal is collected from radiative transitions from the (1,1) band near 315 nm and the collisionally populated (0,0) band near 308 nm with rates  $A_{11}$  and  $A_{00}$ . As with the NO fluorescence strategy, the laser excitation wavelength is well separated from the fluorescence collection band and can be efficiently filtered with combinations of Schott glass (typically 2 mm UG-5 and 1 mm WG-320). The collection filter transmission is plotted with a sketch of the (1,1) and (0,0) emission bands in Figure 58.

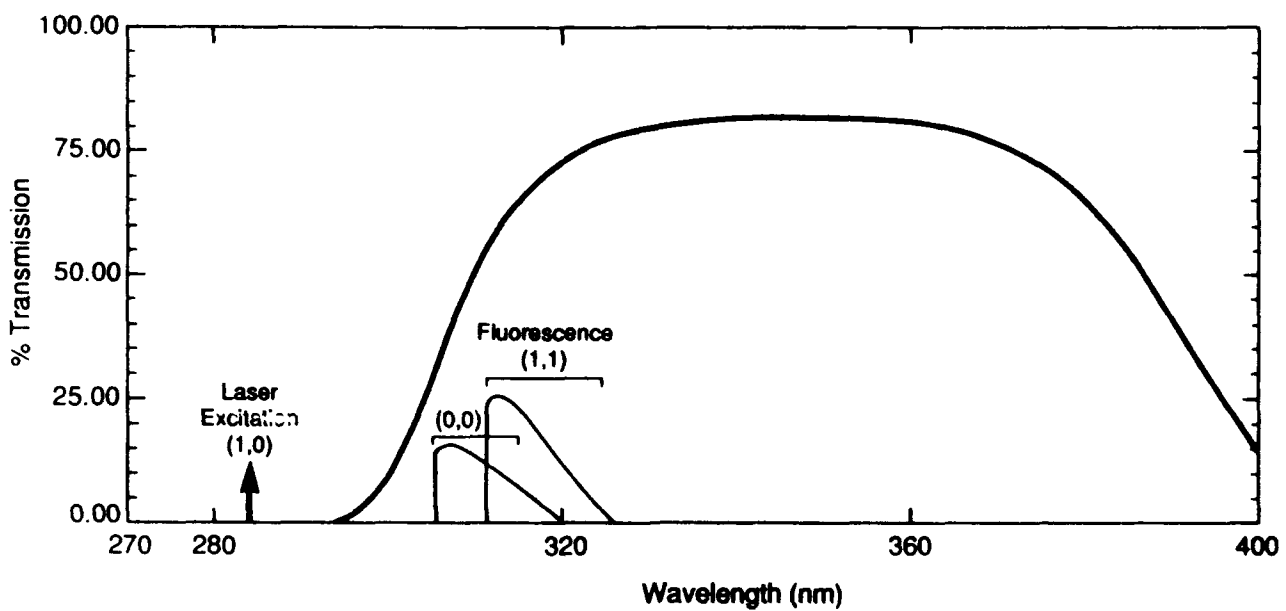


Figure 58

### OH Fluorescence Collection Filter Transmission Efficiency.

The energy level diagram of Figure 57 shows the relevant kinetic processes which must be understood in order to calculate the fluorescence yield. They are defined as follows:

$Q(N)$	=	quenching rate of laser-excited $v' = 1$ level
$R(N)$	=	rate of rotational energy transfer within $v' = 1$
$V(N)$	=	rate of vibrational energy transfer from $v' = 1$ to $v' = 0$
$Q'$	=	rate of electronic quenching from $v' = 0$
$A_{11}(N)$	=	radiative rate for $(1,1)$ band
$A_{00}$	=	radiative rate for $(0,0)$ band.

The  $(N)$  subscript indicates that the rate is a function of the initial  $N$ -level excited by the laser. Fortunately, the kinetics of the  $A^2\Sigma^+$  state in OH in hydrogen and hydrocarbon/air

flame environments are reasonably well understood. Crosley and co-workers<sup>25-29</sup> have completed numerous, detailed studies and have determined many relevant kinetic rates. Thus  $R_{(N)}$ ,  $V_{(N)}$ ,  $Q_{(N)}$ , and  $A_{vv''}$  are known for a variety of conditions. We use these results to guide the calculation of the fluorescence yield that is important for interpreting OH PLIF data using this approach.

For our excitation/detection strategy, the fluorescence yield is determined by writing coupled four-level rate equations and assuming steady-state populations. This results in a yield of the following form:

$$F_y = \frac{T_\lambda A_{11(N)} + T_\lambda A_{00} N_0/N_1}{Q_{(N)} + V_{(N)}} \quad (36)$$

where:

$$\begin{aligned} T_\lambda &= \text{filter transmission at } \lambda \\ N_0/N_1 &= \text{fractional population in } v'=0. \end{aligned}$$

The first term in the numerator is the rate of radiative emission from the  $v' = 1$  state multiplied by the appropriate filter transmission at the wavelength. The second term is the rate of radiative emission from the  $v' = 0$  state multiplied by the filter transmission at this wavelength and multiplied by the fractional population which resides in this level at steady-state. The derivation of Eq. (36) assumes that  $Q$  and  $V >> A$ . Since  $A_{00} = 1.5 \times 10^6 \text{ s}^{-1}$ ,  $A_{11} = 8.5 \times 10^5 \text{ s}^{-1}$ ,  $Q \sim 5 \times 10^8 \text{ s}^{-1}$  and  $V_{(N)} \sim 0.5 Q$ , this assumption is valid for pressure greater than about 0.01 atm.

In order to use Eq. (36), we have made several assumptions about the role of energy transfer. For simplicity, we have assumed a frozen rotational distribution in the excited state, a reasonable assumption for the relatively high N-levels accessed in this work.<sup>25</sup> The rate of vibrational energy transfer (VET) from  $v' = 1$  to  $v' = 0$  is dependent on the initial  $N'$  level excited in the A state. This rate varies linearly with the  $N'$  level and its dependence on  $N'$  has been reported as the ratio of population in  $v' = 0$  to  $v' = 1$ .<sup>27</sup> (Upward vibrational energy transfer is assumed to be negligible). The  $N$ -dependent A-coefficients for the initially excited level in the upper state are tabulated in Ref. 30. For the population transferred to  $v' = 0$ , we rely on the observation that the rotational distribution in  $v' = 0$  is nearly thermal and independent of the initial  $N'$  level in  $v' = 1$ .<sup>28</sup> The value of  $A_{00}$  at  $N' = 5$  is a good average value for excitation of any  $N'$  in  $v' = 1$ .

Lastly, we must estimate rates of electronic quenching from  $v' = 1$  and  $v' = 0$  in the excited state. As discussed in the previous section, these rates will in general depend on the quenching partner composition, temperature, and flow pressure. Unlike NO, the quenching rates for OH depend on initial rotational and level accessed by the laser and will be different for the directly pumped  $v' = 1$  level and the collisionally populated  $v' = 0$ . Reported values for the quenching rates in the rotational manifolds of both vibrational levels comprise an incomplete data set. (In fact, absolute rates of  $N$ -dependent quenching in  $v' = 1$  have not reported for H<sub>2</sub>O, the dominant quencher in most reacting flow environments.) Some data exist, however, for the  $v' = 0$  level which allowed us to estimate the rates of quenching in  $v' = 0$  and  $v' = 1$ .

Given that the rotational distribution in  $v' = 0$  following vibrational transfer is nearly independent of the initial N pumped, it is sufficient to select a single value of quenching to characterize this state. We use the typical value of  $5.6 \times 10^8 \text{ s}^{-1}$  reported by Crosley.<sup>14</sup> For excitation to  $v' = 1$ ,  $v' = 0$  is populated only by VET, so the contribution to the total fluorescence yield is weighted by the amount of transfer, i.e., by the ratio  $N_0/N_1$ , which is dependent on the initial N' excited in  $v' = 1$ . These values have been reported by Smith and Crosley.<sup>27</sup>

Estimating the quenching rates from  $v' = 1$  is more problematic. We assume a N-dependence which is identical to that in  $v' = 0$  and scale the typical values for  $v' = 0$  accordingly. Given room temperature cross-sections for H<sub>2</sub>O, a dominant quencher in most flames (10% variation between N = 0 and N = 5), we can construct a linear function to encompass the required rotational levels. This gives the required N dependence. To obtain absolute quenching rates, the quenching cross sections are normalized to N = 0 and multiplied by the average Q of  $5.6 \times 10^8 \text{ s}^{-1}$  of  $v' = 0$ . This analysis is valid if the rate of quenching from  $v' = 1$  is nearly equal to the quenching rate from  $v' = 0$ . This assumption is supported by the work of Copeland, Wise, and Crosley<sup>28</sup> in their measurements of total cross sections for removal from  $v' = 1$  by H<sub>2</sub>O at room temperature. Recent results<sup>31</sup> suggest that the N dependence at elevated temperatures may be less pronounced than in the room temperature data. But, this variance is small and we neglect it in favor of the more complete room temperature data set.

The discussion above relates to our ability to determine the relative fluorescence yield between any two excitation transitions. Of more concern, however, is our ability to absolutely determine the fluorescence yield for any given transition under any given condition. It appears that, in the absence of *a priori* knowledge of the chemical composition and temperature of the flow, the characteristic value we assume for the quench rate is only valid to within a factor of two or so. This also relates to our ability to relate relative signals within an image to relative OH distributions. Studies which have examined the variation in the total quench rate from  $v' = 0$  in flame environments,<sup>32-34</sup> generally conclude that, across most hydrocarbon and hydrogen flame environments, the local environment in which OH(X) is likely to be found in significant concentrations is chemically and thermally similar. Evidently, the chemical reactivity of OH(X) state mediates the potential variation in the quench rate. Of particular relevance to the present study is the observation that the largest variations can occur in fuel rich hydrogen flames, where the large relative velocity of the light H<sub>2</sub> molecule enhances the quench rate by as much as a factor of 2. Hence, the total quench rate is independent of temperature and chemical composition in essentially all regions of the reacting flowfield except fuel rich zones where it may increase as much as a factor of two. We will assume the same argument applies to the other energy transfer processes in the fluorescence yield and express Eq. (37) as:

$$F_y = \frac{A_{\text{eff}}}{\text{constant} \cdot P} . \quad (37)$$

Combining Eq. (27) with Eq. (19), we can express the temperature, pressure, and number density dependence of the OH fluorescence signal as:

$$S_F = \text{constant} \cdot f_B \cdot N_{OH} \cdot P^{-1} . \quad (38)$$

In cases where the flowfield is nominally at constant pressure, a useful strategy for quantitative measurements would be to choose the  $N^*$  level so that the temperature dependence of the Boltzmann population fraction is minimized over the range of interest. In this limit, the fluorescence signal is only proportional to the OH number density:

$$S_F \sim N_{OH} . \quad (39)$$

Since we have assumed constant, or nearly constant, pressure, the variations in number density must be due to chemical reactions rather than bulk fluid dynamics.

Alternatively, in strongly pressure-varying flows, a  $N^*$  could be chosen so that:

$$f_B \sim T \quad (40)$$

and:

$$S_F \sim N_{OH} \cdot \frac{T}{P} \sim x_{OH} . \quad (41)$$

As with the NO excitation strategy developed earlier, variations in the PLIF distribution within an image would be related to chemical reactions alone.

For the experiments in this study, the OH was confined to the injectant H<sub>2</sub>/air interface downstream of the injector bow shock. This portion of the flowfield is nearly constant pressure, so we elected to pursue the first strategy outlined above. Figure 59 is a plot of the calculated fluorescence signal as a function of temperature for four well-populated rotational

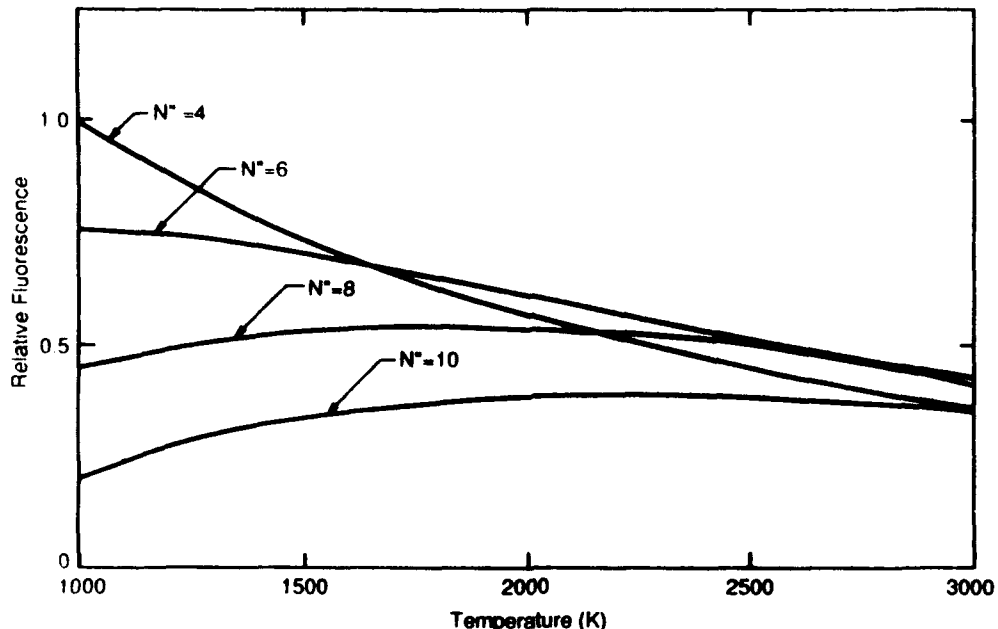


Figure 59

#### Temperature Dependence of OH Fluorescence for Constant OH Number Density

quantum levels at flame temperatures assuming a constant number density. For example, transitions originating from  $N'' = 8$  are essentially insensitive to temperature from 1500 to 3000 K. Practically, the selection of the optimum rotational transition will be governed by the combined consideration of temperature insensitivity, spectral isolation of the transition, and total transition strength.

This OH fluorescence strategy is in principle subject to the same temperature, pressure, and velocity-dependent line width effects discussed in detail in connection with NO fluorescence. Again, the OH lineshape under near atmospheric pressure combustion conditions is described, to first order, by a Voigt lineshape. In contrast to NO lineshapes, however, the

OH lineshape contains a significantly smaller collisional contribution. Hence, collisional shifting and fluorescence signal diminution due to pressure broadening are not significant at pressures below 5 atm. Table 11 summarizes the relevant lineshapes and shifts for the maximum values encountered in this study. In this case, the laser bandwidth was not measured exactly but was taken from the Lambda-Physik product literature. In view of the agreement between this product literature and our measurements at 226 nm, this value should be close to the actual bandwidth. The collisional shift to width ratio is taken from Ref. 35. As with the NO fluorescence, these effects are not significant in the present study.

Wavelength calibration experiments were again undertaken, using an atmospheric pressure propane-air torch as a convenient source of OH at high temperature. A portion of such a scan is shown in Figure 60. The principal branches are labelled. Figure 61 is a more detailed excitation scan of the wavelength region between 283 and 283.5 nm. In Figure 61, the laser excitation scan is shown as the solid line and a simulated spectrum is shown as the dashed line. For this study, the well isolated  $Q_1(7)$  line was selected for excitation, offering high signal strength and a minimum temperature dependence over the expected range of conditions in the reacting flowfield.

Table 11. Linewidths and Shifts for OH Fluorescence

$\Delta\omega_L$	~	$0.5 \text{ cm}^{-1}$
$\Delta\omega_C$	~	$0.015 \text{ cm}^{-1}$
$\Delta\omega_D$	~	$0.3 \text{ cm}^{-1}$
$\Delta\omega_s$	~	$0.002 \text{ cm}^{-1}$
$\Delta\omega_v$	~	$0.1 \text{ cm}^{-1}$

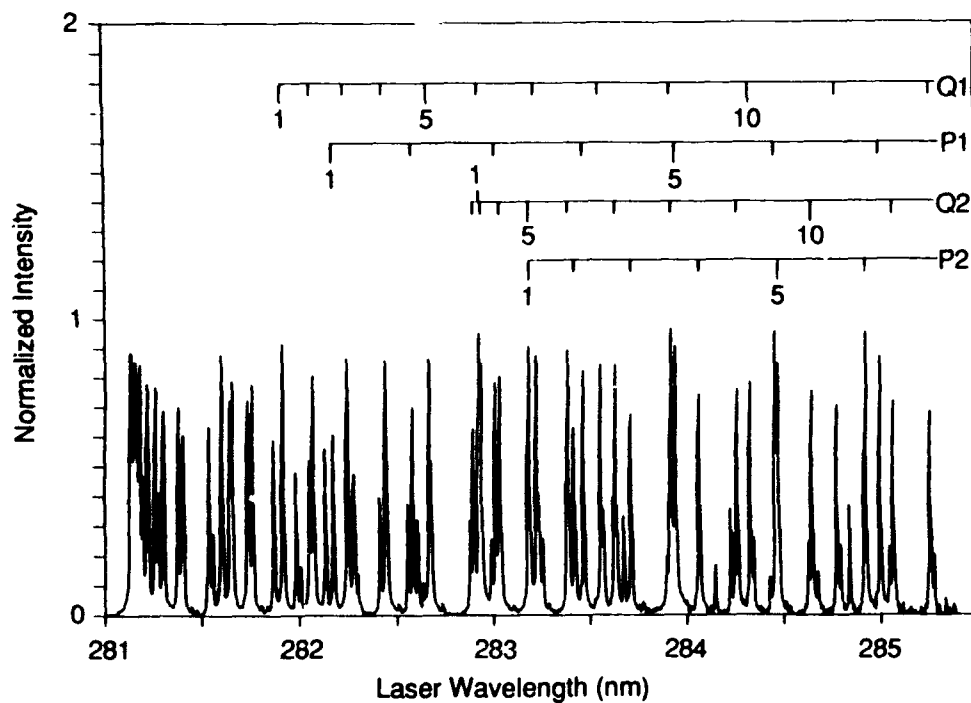


Figure 60

**Flame Temperature OH (1,0) Band Excitation Scan**

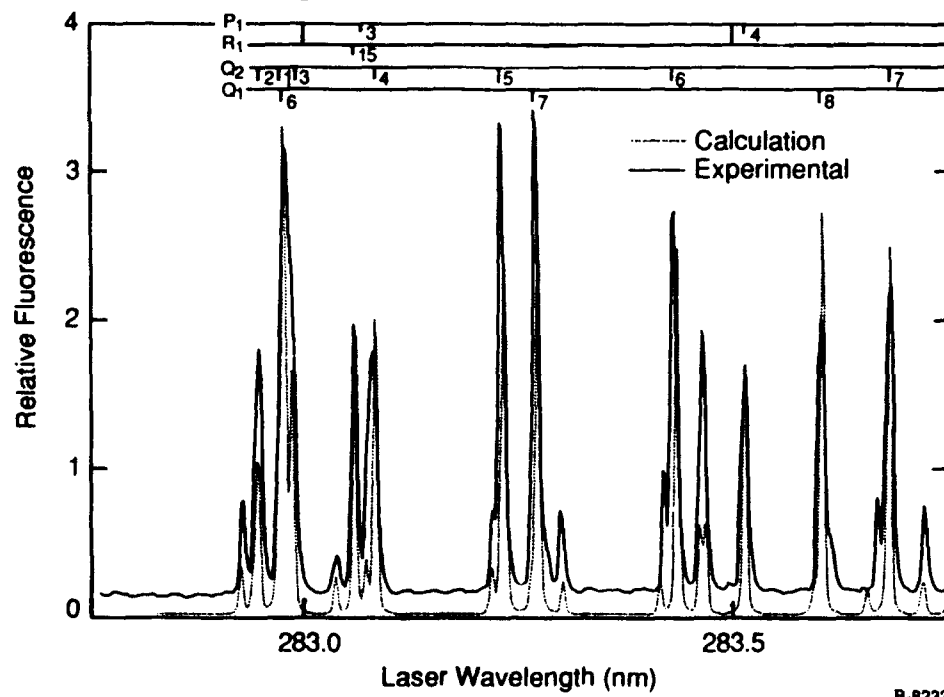


Figure 61

**OH (1,0) Band Excitation Scan Detail**

B-8233



Figure 62

Instantaneous OH Distribution in  $H_2$  Injector Near Field, Injector 1

The first OH PLIF experiments were conducted in the same flow plane as the NO PLIF experiment shown in Figure 55. Approximately 2 mJ of laser energy was delivered in the 3 cm sheet. An example image is shown in Figure 62. The peak fluorescence intensities in this image correspond to approximately 50 photons per pixel. Using the spectroscopic parameters developed above and assuming a nominal flow pressure of 0.5 atm and a temperature of 2500 K, this corresponds to a peak OH concentration of  $\sim 10^{15} \text{ cm}^{-3}$ , or about 100 ppm. This is several orders of magnitude below equilibrium OH number densities for stoichiometric  $H_2$ /air mixtures - we are clearly viewing the ignition zone of the hydrogen jet. In this near-field region of the jet, the OH is confined to the mixing layer between the injectant hydrogen and the hot air behind the bow shock. A low-level "cloud" of OH surrounds the bright central filament and appears to extend upstream to the shock boundary.

Ignition takes place rapidly and the existence of large scale mixing features (on the order of the jet diameter) can be seen in the shear layer, even at these relatively large convective Mach numbers. A low level of OH is visible in the recirculation zone upstream of the nozzle as well. Finally, a low level of OH is visible underneath the jet in the lower right side of the image due to entrainment of air by axial vorticity in the flow.

In the next experiment, the excitation laser sheet and camera were moved downstream to image the OH distribution in the vicinity of the second injector station (see Figure 65). Figure 63 shows two PLIF images taken with the same field of view as Figure 62. The OH-laden plume from the first injector impinges on the second injector plume near the right side of the image. The second injector is angled at 60 degrees to the flow, where the first is at

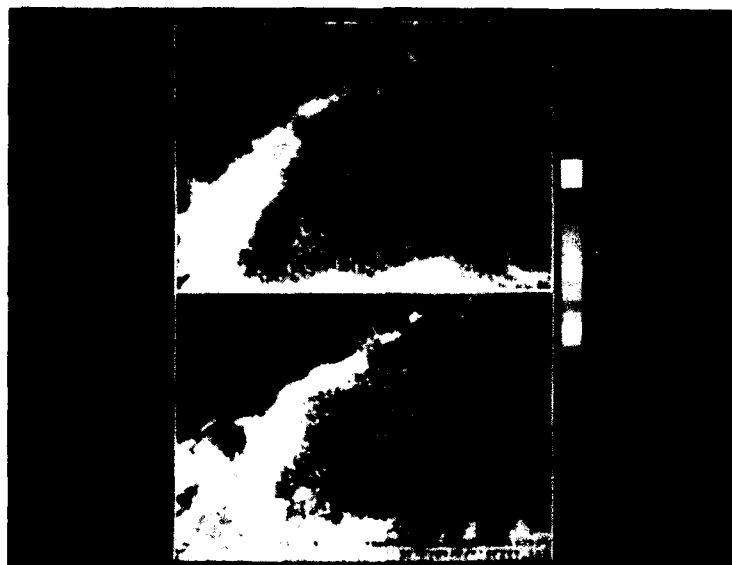


Figure 63  
OH PLIF Images at Second Injector Station

30 degrees. Thus, the plume from the second injector penetrates into the free stream flow more quickly. A similar filament of high OH levels is evident, marking the boundary between the injectant gas and the hot air. A puzzling feature in both images of Figure 62 is the apparently high levels of OH on the tunnel floor. While some trapping of OH in the hot tunnel boundary layer (where the flow stagnates) is expected, it is not physically reasonable that high OH concentrations exist *directly over the injector along the central plane sliced by the laser sheet*. We believe the signal level in this portion of the image is due to out of plane chemiluminescent or thermal emission from the spreading plume which is integrated by the detector during the  $\sim 1\mu\text{s}$  gate of the intensifier.

The emission interference hypothesis is lent credence by the image in Figure 64. In this final PLIF experiment, the laser sheet and camera were moved  $\sim 23$  step heights

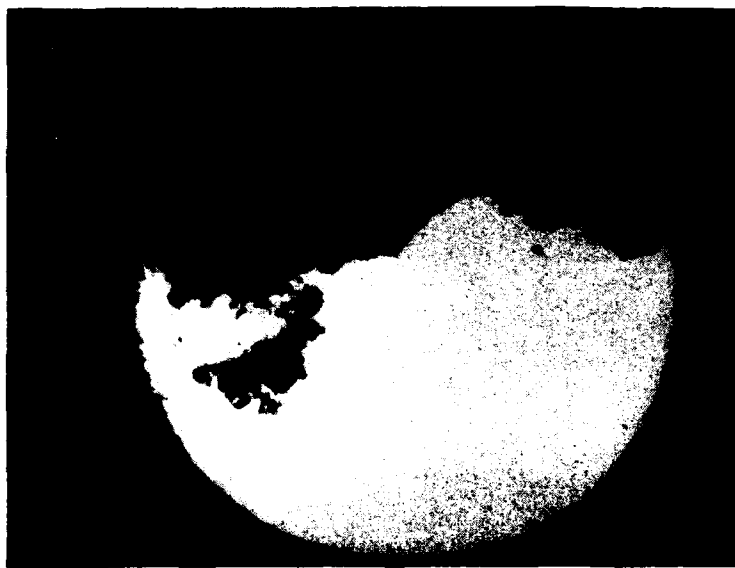


Figure 64

OH Image 23 Step Heights Downstream of Step

downstream of the rear-facing step (over 50 injector jet diameters). The laser sheet was the same size as the earlier images (limited by the laser access window diameters), but the camera was positioned so as to view the entire 9 cm tunnel height through the 10 cm circular windows. Hence, the expected PLIF image would be a 3.8 cm ribbon across the image height. As Figure 64 dramatically displays, no such ribbon is observed and almost half the image is completely saturated.

The image in Figure 64 is clearly a detector-saturated view of the OH chemiluminescence from the reacting jet plume. Since this emission occurs at the exact wavelengths over which the fluorescence signal is collected, it is not possible to spectrally reject it entirely. As a check on this hypothesis, we note that the saturation level of the detector at this gain corresponds to 250 photons. The emission can be related to the population in the OH A-state using the expression:

$$S_F = \eta \cdot \frac{\Omega}{4\pi} \cdot V_c \cdot N_A [T_\lambda A_{00} + T_\lambda A_{11}] \quad (42)$$

where the terms are the same as in Eq. (19), except that the collection volume,  $V_c$ , now includes the entire emitting volume viewed by an individual pixel. An upper bound on this dimension is the tunnel width of 7.5 cm multiplied by the projected pixel area.

Inverting Eq. 63 and solving for  $N_A$  gives:

$$N_A \geq 6 \times 10^8 \text{ cm}^{-3} . \quad (43)$$

Assuming the OH X-state number density is 1% of the total number density at this point in the flow (this is less than equilibrium for a stoichiometric H<sub>2</sub>/air mixture at these temperatures), we can use the Boltzmann relationship to calculate the effective electronic temperature that this measurement suggests, assuming an equilibrium between OH (A) and OH (X):

$$\frac{N_A}{N_X} = \frac{g_A}{g_X} \cdot \exp \left[ \frac{-E_0}{kT} \right] \quad (44)$$

$$T \approx 3000 \text{ K} . \quad (45)$$

This temperature is only ~ 200 K above the adiabatic flame temperature for a stoichiometric mixture of H<sub>2</sub> and air initially at 1000 K. Since it is well known that OH A-state is formed in super-equilibrium concentrations in flames, we conclude the observed emission intensities are consistent with thermal population of OH(A) in the supersonic flame.

As an emission image, Figure 64 can be used to infer the spreading rate of the fuel plume. The most straightforward method for reducing the emission interference, however, is simply using a faster-gating intensifier tube. Commercially available tubes can be gated to ~ 10 ns, reducing the emission signal by a factor of 100 while not effecting the LIF signal. This would reduce the saturated emission signal in Figure 64 to ~ 2 A/D levels, below the minimum color displayed. Emission interference such as this is likely to be an issue in larger facilities where the out of plane path lengths are large and the local flame temperatures

are high. The 10 ns gate would raise the temperature at which equilibrium OH concentrations would saturate the detector with A-state emission to 4000 K. We are currently fabricating such a detector in support of another program. Higher laser energy will also help to drive the fluorescence above the emission background. These data were taken with only  $\sim$  2 mJ of pulse energy. Using a Nd:YAG-pumped system, we can easily generate an order of magnitude more pulse energy. The faster gating camera combined with the more powerful laser will reduce the relative emission/fluorescence signal levels by a factor of 1000.

In summary, the OH PLIF experiments in the reacting flow shock tunnel were used to study details of the near field injector/main flow interactions. The point of ignition of the fuel stream was readily observed as well as characteristic large scale structures in the mixing layer. The large scale structures warped the instantaneous position of the bow shock, which appeared to wrap around the dynamic jet flowfield. Further downstream, the OH chemiluminescence interfered with the weak fluorescence image. Nevertheless, information on the spreading and burning of the fuel jet can be extracted from the images, as discussed in Section 5.

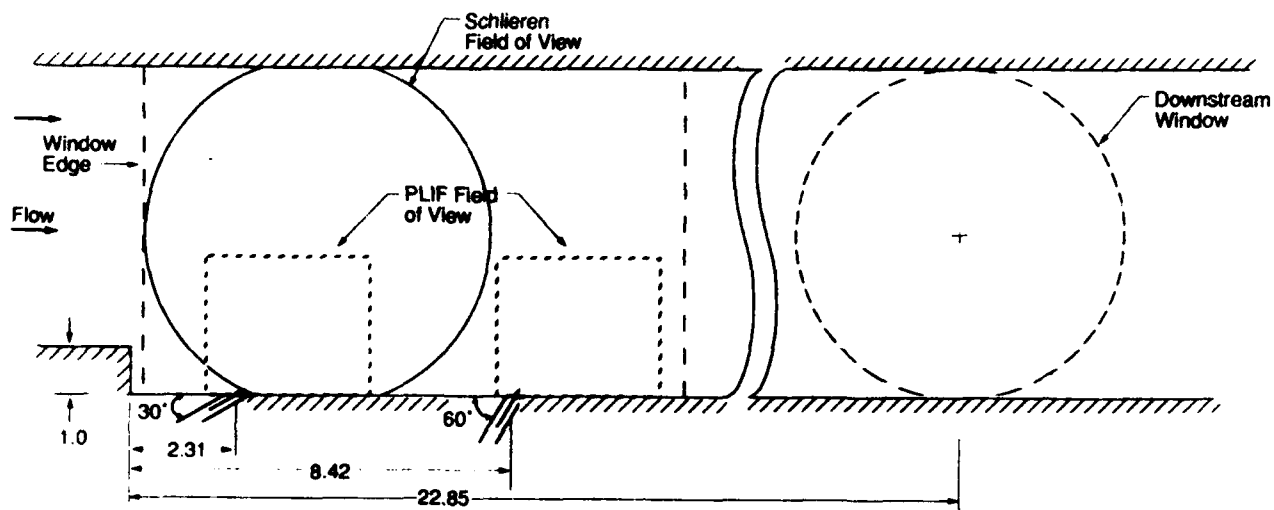
## 5. DISCUSSION OF RESULTS

The previous sections have focused on the design and performance of the shock tunnel and the details of optical diagnostics used to probe the high enthalpy mixing/combusting flows. This section will summarize the results from the initial tests using the shock tunnel and the array of optical diagnostics which were developed for this program. In several cases these results are first-of-their-kind measurements in high temperature flows of this scale.

As previously discussed in the section describing the measurement of NO temperature and concentration, a reference measurement for determining the flow duration and temperature is extremely useful. This measurement routinely determines the beginning and end of the high temperature flow and can be used to quantify the flow temperature. As shown in Figures 33 and 35 the variation of flow temperature can be as large as 200 deg during the experimental test time.

Figure 65 illustrates the optical access regions for the Schlieren, PLIF, and OH emission imaging measurements. Included in this figure is the position of the rearward facing step and the injector tubes and locations. Comparison of the various images is possible given the location of these viewing areas.

A comparison of the Schlieren image of the recompression shock and the NO PLIF image of this same feature shows that each technique very clearly images the shock location, Figure 66. The comparison also shows the fundamental difference between the spatially



Notes - 1. Dimensions are in Step Heights (step height = 1.27 cm)  
 2. Injector Tubes are 0.48 cm Diameter

Figure 65

**Optical Access Stations and the Relative Locations of the Rearward Facing Step and the Injector Tubes**

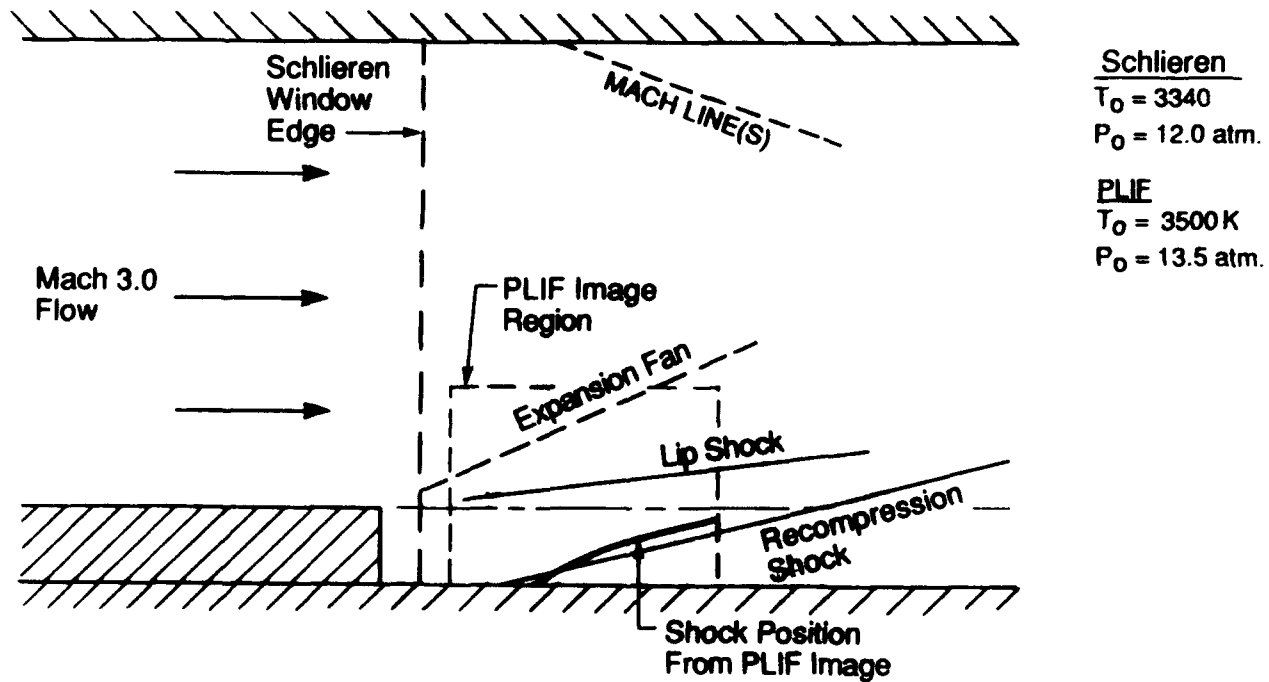


Figure 66

**Overlay of Schlieren and PLIF Images of the Recompression Shock After the Rearward Facing Step**

resolved PLIF image and the schlieren image. The shock in the schlieren photograph appears to be feathered and this result can be attributed to the path length integration across the flow field which is inherent in standard Schlieren measurements. For the PLIF image the position of the shock at the centerline of the tunnel is determined since measurement volume is defined by the intersection of the laser sheet and the imaging area. As expected this shock does not show the "feathering" of the Schlieren image.

A more exciting comparison is given by Figure 67 which compares schlieren and NO PLIF results for helium injection. The schlieren results clearly show the bow shock which is on the centerline of the tunnel and is due to the hydrogen injectant plume. In addition the

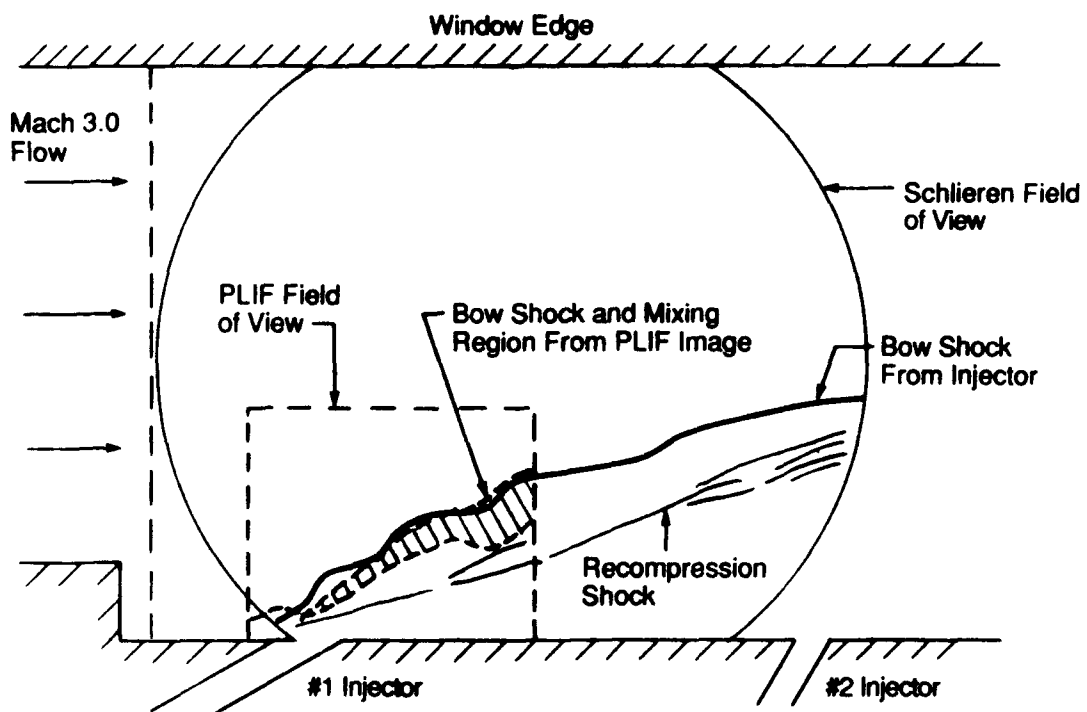


Figure 67

Comparison of Schlieren and PLIF Images of Helium Injectant into the Flow Behind a Rearward Facing Step

Schlieren image also shows the recompression shock that is unaffected by the injector away from the tunnel centerline. It is interesting to note the waviness of the bow shock in the Schlieren image which is an indicator that the position of the shock front varies slightly over time. A comparison of the bow shock and mixing region as determined by the NO PLIF image illustrates that once again the two diagnostics are in very good agreement in terms of the spatial location of the of the bow shock. In addition, since the PLIF image is from the tunnel centerline, it definitively shows the bow shock to be centered in the tunnel; this was postulated but not proven by the Schlieren image. Finally, both images show that the bow shock does not meet the tunnel wall which implies that the recirculation zone may extend to the base of the injector. The PLIF image also defines the edge of the unmixed jet in the flow and shows that it too is a wavy interface indicating probable fluctuations in its position.

Finally a comparison of reacting and nonreacting flow images is possible by overlaying the OH image, with an adjusted color scale to display the OH bearing regions, and the NO image that was previously discussed (Figures 55 and 62 respectively) as shown in Figure 68. The OH bearing regions clearly are on the periphery of the jet or in the mixing regions between the jet and the bow shock. This comparison illustrates that the combusting and non-combusting flows are qualitatively similar. Two other points are of interest when examining the OH fluorescence image. The appearance of OH very near to the injector outlet on the leading edge of jet with a distinct separation from the low levels of OH in the recirculation zone indicates (preliminarily but not conclusively) that the combustion is thermally initiated instead of being seeded with OH radicals which help start the combustion process. This radical "pool" is more typical of lower temperature combustion devices which rely on flame

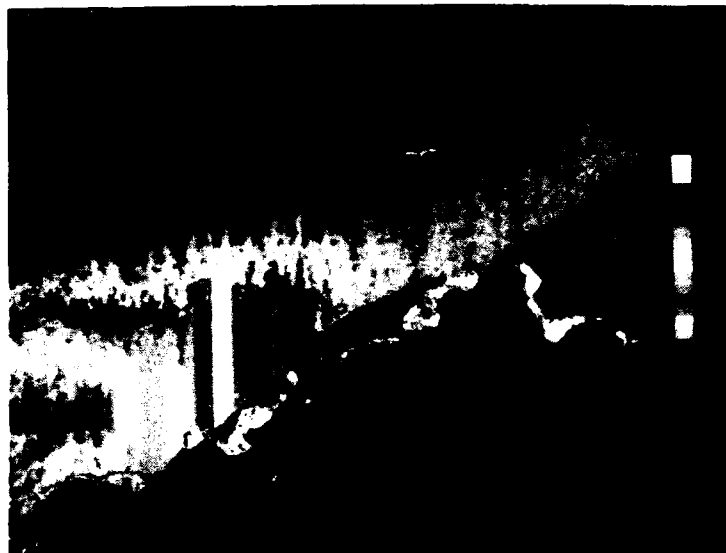


Figure 68

Comparison of PLIF Images of Helium Injection and Hydrogen Injection Behind a Rearward Facing Step. The white region is the OH bearing region from the OH PLIF image

holders (or recirculation zones) to produce steady combustion. The image alone does not allow this interpretation since it is possible that a continuous zone of OH is present between the two zones at a concentration just below the detection threshold. However, the ignition time for the jet can be approximated by comparing the ignition length (1.1 cm) to the exit velocity of the jet (1200 m/s) to yield a time of approximately  $10 \mu\text{s}$ . Given the very high temperatures behind the bow shock, this result is not unreasonable and therefore further substantiates the view that the combustion in this device is thermally initiated and maintained.

Figure 64 shows an emission image from the downstream window illustrated in Figure 65 and illustrates the spreading of the combustion zone after the injector station. This image is sensitive to emission from the OH A-X transition and therefore will represent both

chemically and thermally populated OH A-state radiation. The image illustrates that 17.5 step heights downstream of the center of the injection zone, combustion has spread across 55 percent of the tunnel height (3.85 step heights). This implies a spreading rate of 0.22 which in turn indicates that for the reaction to reach the opposite tunnel wall a length of approximately five tunnel heights is required. Two other interesting notes are appropriate for this image. First, the image shows a wavy interface which is apparently the beginning of the reaction zone and a pocket of low OH emission levels is contained in the otherwise saturated zone of the image. The implication is that a significant degree of spatially non-uniformity exists both at the reaction zone interface and within the region which is nominally combusting. Finally, pressure measurements which were made in this region of the shock tunnel along the top wall, for all the combusting tests, did not indicate a significant difference between the combusting and non-combusting flows. Clearly, optical measurement methods are a superior method of monitoring combustion in the near injector zone.

## 6. CONCLUSIONS

This report has described an experimental effort which both developed a high enthalpy flow facility and successfully applied optical diagnostic measurement techniques to the non-reacting and reacting flow field. A shock tunnel was designed, assembled, and verified to produce Mach 3.0 flows with stagnation pressures and temperatures of 12.0 to 50 atm and 3000 to 4000 K. Schlieren, NO infrared emission, and NO and OH PLIF were developed and demonstrated on the high enthalpy reacting flow facility. The NO emission measurements indicated a fluctuating temperature field (approximately 10% of the mean value). These fluctuations were not inferred by pressure measurements in the facility plenum and flow section. The NO and OH PLIF images were shown to be useful in describing both temperature and mixing properties of the flow field (using NO) and as direct means of identifying reaction zones (using OH). The OH PLIF images were particularly useful in identifying combustion zones which were not measurable using conventional wall pressure measurements. Thermal and chemiluminiscent emission from OH were shown to significantly affect diagnostic strategies in large, high temperature flow facilities. Absorption measurements require the use of an exceptionally bright source while the emission interference in OH PLIF measurements at the high combustion temperatures possible in scram jet flows dictates the use of exceptionally short camera gate widths (10 ns). Combustion results from this work indicate prompt ignition of the hydrogen jet (approximately 10 ns) and a flame spreading rate of 0.22 was observed. Therefore, the duct length required, given the injector configuration described in the report, for the reaction to spread across the entire flow is approximately five duct heights.

In addition to the direct conclusions just enumerated, the program has demonstrated the effectiveness of advanced diagnostic methods for monitoring scramjet processes. These results represent the first application of a range of optical diagnostics to a medium scale pulsed reacting flow facility. The benefits from these types of measurements to the development of high-speed flight vehicles can range from an evaluation of flow quality to direct assessments of the injection and mixing region that is critical to scramjet performance. Future work, using nonintrusive measurements, will undoubtedly contribute greatly to scramjet and/or high-speed flight combustor development.

## 7. REFERENCES

1. Liepmann, H.W. and Roshko, A., Elements of Gasdynamics, John Wiley and Sons, Inc., New York, 1965.
2. Gaydon, A.G. and Hurle, I.R., The Shock Tube in High-Temperature Chemical Physics, Reinhold Publishing Corporation, New York, 1963.
3. Mirels, H., "Boundary Layer Growth Effects in Tubes," Proceedings of the Eighth International Shock Tube Symposium, Chapman and Hall, London, 1971.
4. Mirels, H., "Shock Tube Test Time Limitation Due to Turbulent-Wall Boundary Layer," AIAA Journal 2, 1, pp. 84-93, 1964.
5. Momtchiloff, I.N., Taback, E.D., and Buswell, R.F., "Kinetics in Hydrogen-Air Flow Systems. I: Calculation of Ignition Delays for Hypersonic Ramjets," Ninth Symposium (International) on Combustion, Academic Press, New York, 1963.
6. Parker, T.E., Allen, M.A., and Rawlins, W.T., "Supersonic Combustion: Enhanced Ignition, Mixing, Flame Holding, and Diagnostic Concepts," Final Report, PSI TR-759, March 1988.
7. Kee, R.J., Miller, J.A., and Jefferson, T.H., "CHEMKIN: A General-Purpose, Problem-Independent, Transportable, FORTRAN Chemical Kinetics Code Package, Report SAND 80-8003, Sandia Laboratories, Albuquerque, NM, 1980.
8. Teare, J.S., "Semi-Annual Progress Report Reentry Physics (REP) Program," Contract AF 04(694)-690, July 1966.
9. Cohen, L.S., Coulter, L.J., and Egan, W.J., "Penetration and Mixing of Multiple Gas Jets Subjected to a Cross Flow," AIAA J. 9(4), 718 (1971).
10. Billig, F.S., "Current Problems in Non-Equilibrium Gas Dynamics SCRAMJET Engines," presented at AIAA Professional Study Seminar on Gas Dynamics, Buffalo, NY, June 1989.
11. Roshko, A. and Thonke, G.T., "Observations of Turbulent Reattachment Behind an Axisymmetric Downstream-Facing Step in Supersonic Flow," AIAA Journal, V. 4, No. 6, 1966.
12. Stein, A., "Supersonic Flow Separation on a Backward Facing Step," Report No. AS-66-18, AFOSR Grant 268-66, 1966.

13. Sirleix, M., Mirande, J., Deleny, T., "Basic Experiments on the Reattachment of a Supersonic Stream," Royal Aircraft Establishment, Library Translation No. 1196, 1965.
14. Hortzaiker, J.R., "An Experimental Investigation of the Affect of the Approaching Boundary Layer on the Separated Flow Behind a Downstream Facing Step," National Aerospace Laboratory (The Netherlands), NLR TR 700334.
15. Rawlins, W.T., Fraser, M.E., and Miller, S.M., "Rovibrational Excitation of Nitric Oxide in the Reaction of O<sub>2</sub> with Metastable Atomic Nitrogen," J. Phys. Chem. 93, 1097 (1989).
16. Dieke, G.H. and Crosswhite, H.M., "The Ultraviolet Bands of OH Fundamental Data," J. Quant. Spectrosc. Radiat. Transfer 2, 97 (1962).
17. Piper, L.G. and Cowles, L.M., "Einstein coefficients and Transition Moment Variation for the NO (A <sup>2</sup>S<sup>+</sup> - X <sup>2</sup>P) Transition," J. Chem. Phys. 85(5), 2419 (1986).
18. Timmerman, A. and Wallenstein, R., "Doppler-Free Two-Photon Excitation of Nitric Oxide with Frequency-Stabilized CW Dye Lasers," Opt. Comm. 39(4), 239 (1981).
19. Earls, L.T., "Intensities in <sup>2</sup>P - <sup>2</sup>S Transitions in Diatomic Molecules," Phys. Rev., 48, 423 (1935).
20. I.S. McDermid and J.B. Laudenslager, "Radiative Lifetimes and Electronic Quenching Rate Constants for Single-Photon-Excited Rotational Levels of NO (A <sup>2</sup>S<sup>+</sup>, v' = 0)," J. Quant. Spectrosc. Radiat. Transfer 27(5), 483 (1982).
21. G.A. Raiche and D.R. Crosley, "Temperature Dependent Quenching of the A <sup>2</sup>S<sup>+</sup> and B <sup>2</sup>P States of NO," J. Chem. Phys. 92(9), 5211 (1990).
22. R.J. Cattolica, T.G. Mataga, and J.A. Cavolowsky, "Electronic Quenching and Vibrational Relaxation of NO A <sup>2</sup>S (v' = 1 and v' = 0) by collisions with H<sub>2</sub>O," J. Quant. Spectrosc. Radiat. Transfer 42(6), 499 (1989).
23. M.G. Allen and S.J. Davis, "Velocity Measurements in High Temperature Gases Using Laser-Induced NO Fluorescence," Final Report for USAF Systems Division Contract No. F33615-90-C-209, PSI TR-1108 (1991).
24. M.P. Lee and R.K. Hanson, "Calculations of O<sub>2</sub> Absorption and Fluorescence at Elevated Temperatures for a Broadband Argon-Fluoride Laser Source at 193 nm," J. Quant. Spectrosc. Radiat. Transfer, 36(5), 425 (1986).

25. G.P. Smith and D.R. Crosley, "Quantitative Laser-Induced Fluorescence in OH: Transition Probabilities and the Influence of Energy Transfer," 18th Symposium (Int.) on Combustion (Pittsburgh: The Combustion Institute), 1511 (1981).
26. D.R. Crosley and G.P. Smith, "Rotational Energy Transfer and LIF Temperature Measurements," Combustion and Flame 44, 27, (1982).
27. G.P. Smith and D.R. Crosley, "Vibrational Energy Transfer in A  $^2\Sigma^+$  OH in Flames," App. Opt. 22(10), 1428, (1983).
28. R.A. Copeland, M.L. Wise, and D.R. Crosley, "Vibrational Energy Transfer and Quenching of OH (A  $^2\Sigma^+$ , v' = 1)," J. Phys. Chem. 92, 5710 (1988).
29. N.L. Garland and D.R. Crosley, "On the Collisional Quenching of Electronically Excited OH, NH, and CH in Flames," 21st Symposium (Int.) on combustion (Pittsburgh: The Combustion Institute), 1693 (1986).
30. I.L. Chidsey and D.R. Crosley, "Calculated Rotational Transition Probabilities for the A-X System of OH," J. Quant. Spectros. Radiat. Transfer 23, 187 (1980).
31. J.B. Jeffries, K. Kohse-Hoinghaus, G.P. Smith, R.A. Copeland, and D.R. Crosley, "Rotational-Level Dependent Quenching of OH (A  $^2\Sigma^+$ ) at Flame Temperatures," Chem. Phys. Lttrs. 152(2,3), 16-0 (1988).
32. D. Stepowski and M.J. Cottreau, "Study of Collisional Lifetime of Hydroxyl ( $^2\Sigma^+$ , v'=0) Radicals in Flames by Time-Resolved Laser-Induced Fluorescence," Combustion and Flame 40, 65 (1981).
33. M.C. Drake and R.W. Pitz, "Comparison of Turbulent Diffusion Flame Measurements of OH by Planar Fluorescence and Saturated Fluorescence," Experiments in Fluids 3, 283 (1985).
34. R.S. Barlow and A. Collignon, "Linear LIF Measurements of OH in Nonpremixed Methane-Air Flames: When Are Quenching Corrections Unnecessary?," AIAA Paper No. 91-0179, 29th Aerospace Sciences Meeting, January (1991).
35. B. Shirinzadeh, D.M. Bakalyar, C.C. Wang, "Measurement of Collision-Induced Shift and Broadening of the Ultraviolet Transitions of OH," J. Chem. Phys. 82, 2877 (1985).

## Appendix

### OH Absorption

#### OH(0,0) Theoretical Considerations

Characteristics of the OH(A-X) spectrum at shock temperatures and pressures impact the choice of appropriate rotational lines with which the absorption measurements will be made. In addition, knowledge of relative strengths of rotational lines and their respective line widths is necessary in order to ascertain the optimal source and detector arrangement.

In this Appendix we discuss theoretical issues relating to the OH(A-X) spectrum under shock conditions. To resolve these issues, we simulated an OH spectrum; the treatment of which is discussed herein.

This simulation also provided a database for the practical aspects relating to the source and detector choice for the absorption measurements.

#### OH Spectrum Simulation

In an absorption measurement, the fractional transmission  $I/I_0$  is related to the absorption coefficient  $k_\omega$  via Beer's law:

$$I/I_0 = \exp(-k_\omega l)$$

where:       $l$       =      pathlength of absorption  
 $k_{\omega}$       =      absorption coefficient  
 $I/I_0$       =      fractional transmission.

Clearly, the absorption coefficient is a measure of the fractional transmission since:

$$-\ln(I/I_0)/l = k_{\omega}$$

A plot, then of absorption coefficients versus wavelength, is in effect a simulated absorption spectrum. The absorption coefficient is given by:

$$k_{\omega} = K_{ji} Y(\omega)$$

where:

$K_{ji}$       =      the line strength of the transition ( $E_i > E_j$ ), and  
 $Y(\omega)$       =      the line profile which accounts for broadening.

$Y(\omega)$  is normalized so that  $\int_{\omega_1}^{\omega_2} Y(\omega) d\omega = 1$ . At any given frequency within the line,  $\omega_1 < \omega < \omega_2$ .  $Y(\omega)$  is best described by a Voigt profile, which is a convolution of the Gaussian distribution induced by Doppler effects with the Lorentzian distribution caused by collisional effects. The exact Voigt profile can be calculated through extensive computations but it is a level of detail which is not supported by the needs of the present task. Instead, we have chosen to simulate a stick spectrum based on absorption coefficients in line center and impose on these lines reasonable linewidths based on Doppler and collisional linewidths of OH under specific conditions of temperature pressure.

### Absorption Coefficient Determination - The OH Stick Spectrum

As mentioned, the absorption coefficient  $k_{\omega} = K_{ij}Y(\omega)$ . Since we have chosen to ignore details of the line shape, we set  $Y(\omega) = 1$ .  $K_{ji}$  is the line strength of the transition, which depends on the population of the  $j^{\text{th}}$  level as well as the oscillator strength for the transition.  $K_{ji}$  is related to the population and oscillator strength by:

$$K_{ji} = \frac{\pi e^2}{m_e c^2} (N_j f_{ji} - N_i f_{ij})$$

where  $N_j f_{ji}$  and  $N_i f_{ij}$  account for stimulated absorption and emission, respectively. Since the system is in thermodynamic equilibrium,  $N_i$  and  $N_j$  are related by the Boltzmann relation and the oscillator strengths are related by:

$$g_i f_{ij} = g_j f_{ji} .$$

Substitutions give:

$$K_{ji} = \frac{\pi e^2}{m_e c^2} N_j f_{ji} \left( 1 - e^{-hc\omega_0/kT} \right) .$$

Since  $e^{-hc\omega_0/kT} \ll 1$  in most cases, we can simplify this expression to:

$$K_{ji} = \frac{\pi e^2}{m_e c^2} N_{J''} f_{J''J'} ,$$

where  $f_{J''J'}$  is the oscillator strength and  $N_{J''}$  is the population in  $J''$ . Recognizing that  $\pi e^2 / m_e c^2$   $f_{J''J'}$ , equals the Einstein B coefficient, we make the replacement:

$$K_{ji} = N_j B_{0,0}$$

Relative B coefficients for the OH(0,0) have been tabulated by Chidsey and Crosley.<sup>1</sup> The frequency of each rotational transition is given by Dieke and Crosswhite.<sup>2</sup> Lastly, we obtain relative populations,  $N_j$ , from the Boltzmann relation:

$$\frac{N_j}{N_T} = \frac{(2J+1) e^{-E_j/kT}}{Q_R},$$

where  $E_j$  is the term energy,  $Q_R$  is the rotational partition function which can be approximated as  $kT/hcB_v$  where  $B_v$  is the rotational constant of the species in vibrational level  $v$ . Relative populations are calculated for each rotational level using:

$$N_j(\text{rel}) = (2J+1) e^{-E_j/kT}.$$

Finally, we can calculate the relative absorption coefficient,  $k_\omega(\text{rel})$ :

$$k_\omega(\text{rel}) = B_J'' J' (2J+1) \exp[-E_J/kT]$$

as a function of wavelength, which gives a stick spectrum. The relative intensities of the observed lines are due to both concentration and temperature effects as can be seen by comparing the simulated OH spectrum at 1000 K versus 6000 K (Figures A-1 and A-2). The assigned rotational transitions of the OH(A-X) spectrum are shown in Figure A-3.

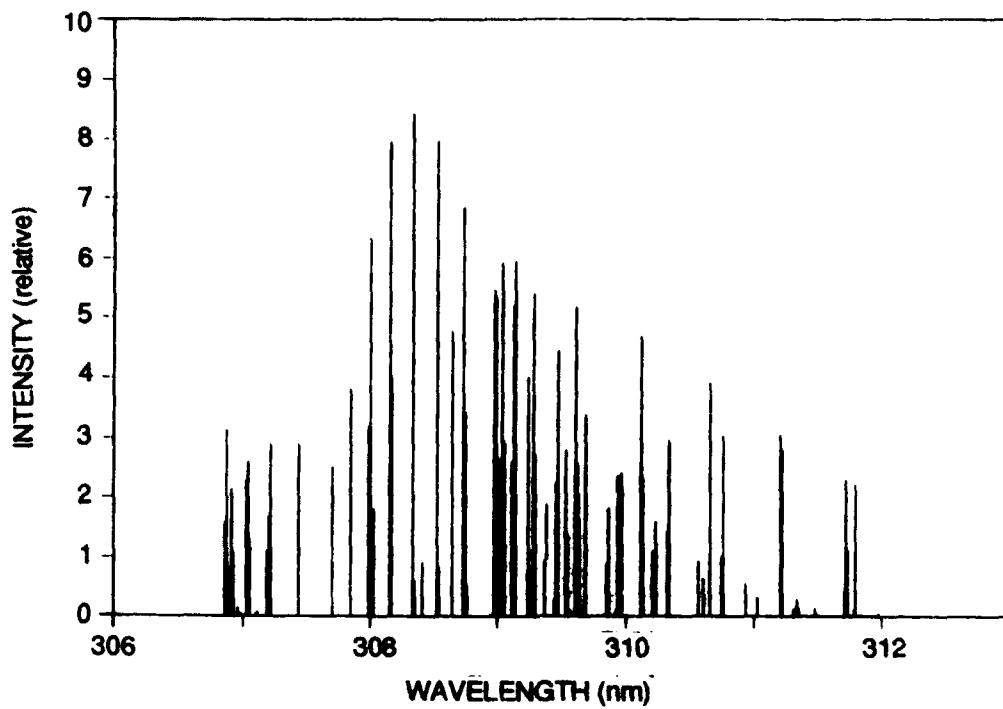


Figure A-1

OH Stick Spectrum for 1000 K

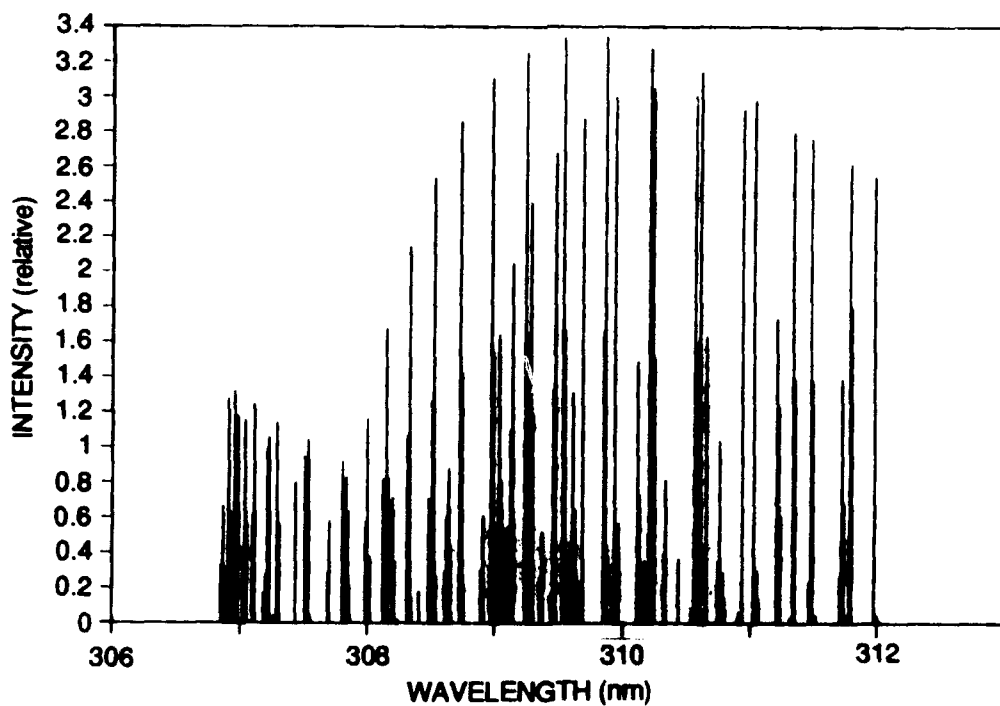


Figure A-2

OH Stick Spectrum for 6000 K

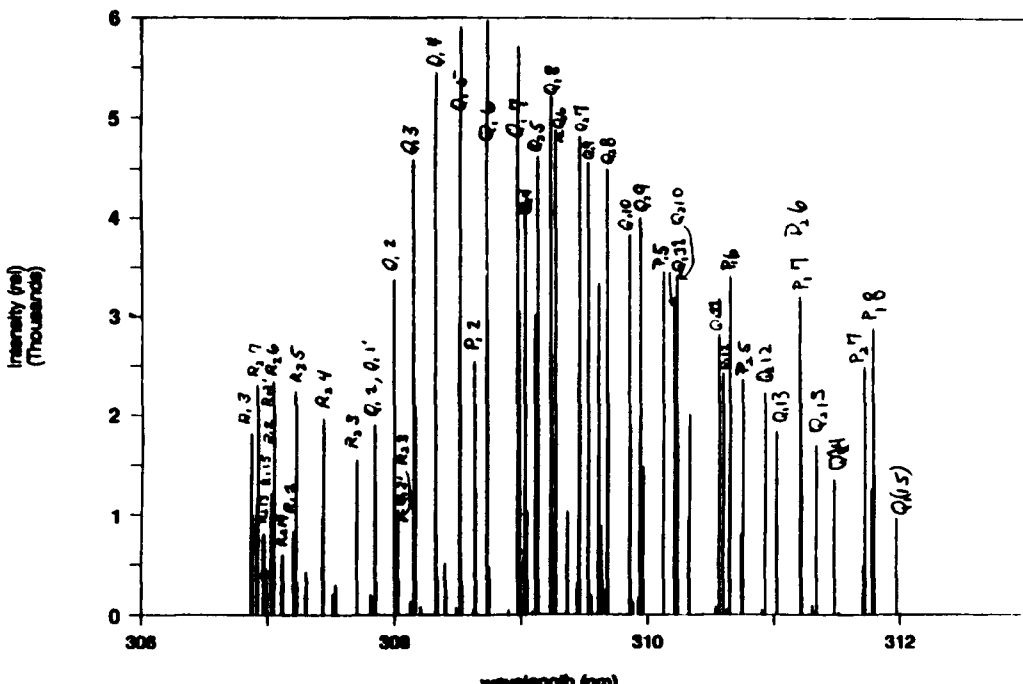


Figure A-3

### OH(A-X) Rotational Line Assignments

#### Absolute Absorption Coefficients

As a further note, relative absorption coefficients can be placed on an absolute, absorption per molecule, basis. The oscillator strengths  $f_{J''J'}$  for a given rotational line is related to the band oscillator strength,  $f_v$ , via:

$$f_J = \left( \frac{f_v}{4} \right) \left[ \frac{S_J}{(2J''+1)} \right] T_J ,$$

where  $S_J$  is the theoretical line strength, and  $T_J$  is the vibrational rotation-correction factor.

Band oscillator strengths  $f_v$  as a function of rotational line have been experimentally determined by Rouse and Engleman<sup>3</sup> from line absorption measurements in a high temperature ( $\approx 1500$  K) furnace.

### Concentration and Temperature Sensitivity

A system in thermodynamic equilibrium has a population distribution given by the Boltzmann fraction which can be written as:

$$\frac{N_{J''}}{N_T} = \frac{2J''+1}{Q} \cdot e^{-BJ(J+1)/kT} ,$$

where:

$N_{J''}$  = number density in rotational level  $J''$

$Q$  = molecular partition function

$E_t$  = total term energy of state pumped.

The extent of a rotational line absorption will depend on the temperature and concentration in that rotational level  $J''$ . Clearly when making a concentration measurement using absorption, we would like the temperature dependence on that measurement to be minimal. We can calculate the  $J$ -level at which the temperature dependence is minimized by differentiating the Boltzmann fraction with respect to temperature. Setting the result equal to zero, and solving for  $J$ , gives:

$$J = 0.83 \sqrt{\frac{T(K)}{B(cm^{-1})}} ,$$

for OH,  $B = 18 cm^{-1}$  and at 2000 K,  $J' = 8.5$

### Linewidth Considerations

In temperature and concentration determinations using OH absorption measurements, isolated OH rotational lines greatly simplify data reduction. In order to locate isolated lines in the OH(A-X) spectrum, we manipulated the simulated OH spectrum by imposing theoretical linewidths on the rotational lines to check for overlap under various conditions of temperature and pressure.

Broadening of a rotational line is the result of both Doppler and collisional effects. The degree to which the line is broadened depends on their relative contributions. As mentioned, an exact treatment is found by using a Voigt profile. For our purposes, where we are unconcerned about the details of line shape, we can estimate the worst-case linewidth of summing the calculated collisional and Doppler linewidths. As Figure A-4 shows, in most scenarios, either Doppler or collisional broadening will dominate. Obviously, in those cases where they are comparable, summing their values will overestimate the true linewidth of the line.

The OH stick spectrum was artificially "broadened" by imposing a triangle on each rotational line where the base of the triangle is given by twice the calculated linewidth. A triangle is a fairly good approximation of a Gaussian (Doppler broadened) profile. The collisional contribution to the Doppler broadened line will add population to the "wings," and as this contribution grows the line shape will approach a Lorentzian distribution. Although we do not account for this change of shape, since a triangle will be used throughout, we constrain

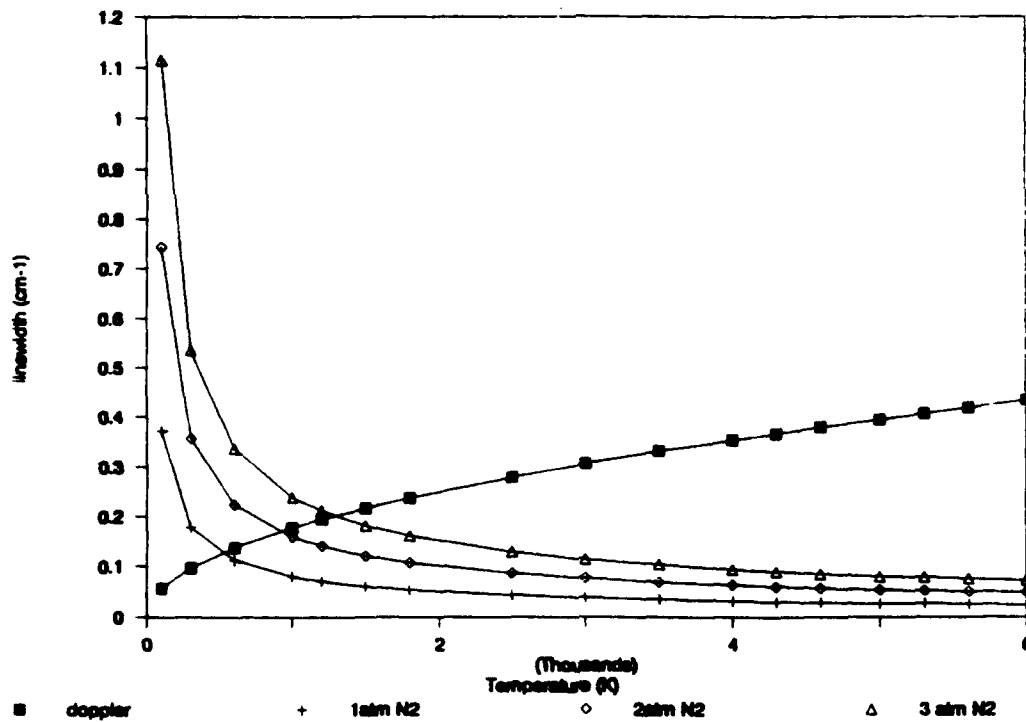


Figure A-4  
Doppler and Pressure Broadened OH Linewidths

our isolation criteria by stipulating that the separation between neighboring lines be 1.5 times our calculated linewidths.

### Doppler Linewidths

Doppler linewidths were calculated from the equation:

$$\Delta\nu_d(\text{cm}^{-1}) = 7.1623 \times 10^{-7} \left( \frac{T}{m_{\text{OH}}} \right)^{1/2} v_0 ,$$

where  $v_0$  is the frequency at line center and the molecular weight for OH is 17.007 amu.

### Collisional Linewidths

Collisional linewidths were calculated under shock conditions using the methodology and data of Hanson et al.<sup>4</sup> As outlined, the collisional linewidth is taken as the sum of the contribution from the individual broadening species. Each component of this sum is the product of a pressure independent broadening parameter and the partial pressure  $P_i$  of the species.

$$\Delta\nu_{\text{coll}} = \sum_i 2\gamma_i P_i .$$

Hanson observed collisional broadening to be dominated by the background gas used, Ar or N<sub>2</sub>, so we will follow suit in this analysis, and allow the partial pressure  $P_i$  to be equal to the total pressure of the background gas. The broadening parameter  $2\nu$  is dependent on temperature as well as the species used. Its dependence on temperature is commonly written as:

$$2\gamma_i = 2\gamma_0 \left( \frac{T_{\text{ref}}}{T} \right)^N ,$$

where  $2\gamma_0$  is a known quantity at the reference temperature  $T_{\text{ref}}$ . The exponent,  $n$ , will vary from 0.5 to 1.0, but is tabulated for both N<sub>2</sub> and Ar.<sup>4</sup> Measured values of  $2\gamma_0$  at 2000 K show a slight J dependence in the case of N<sub>2</sub> but not in Ar. Since N<sub>2</sub> also gives an overall larger  $2\gamma_0$  than Ar, we chose N<sub>2</sub> as the bath gas and used the maximum  $2\gamma_0$  at 2000 K in order to calculate  $2\gamma_0$  at temperatures ranging from 100 to 6000 K. The FWHM for collisional broadening,  $\Delta\nu_{\text{coll}}$ , was then calculated by multiplying the  $2\gamma_0$  values by the total pressure which we varied from 1 to 3 atm.

The results of the Doppler and collisional linewidth calculations are shown graphically in Figure A-4. Since the Doppler width is also dependent on frequency, an average Doppler width was used for this comparison. Wavelength dependent Doppler linewidths, however, are used in the simulated spectra.

### Results

Figures A-5 and A-6 show the increased linewidth due to pressure broadening upon increasing the background pressure from 1 atm (Figure A-5) to 30 atm (Figure A-6). Under the imposed shock conditions, the simulated spectra gave a plethora of suitable rotational lines. Spectra such as these enabled us to locate isolated lines in the OH spectrum. Clearly, we will not be limited in choosing rotational lines because of inherent overlap of neighboring lines due to broadening.

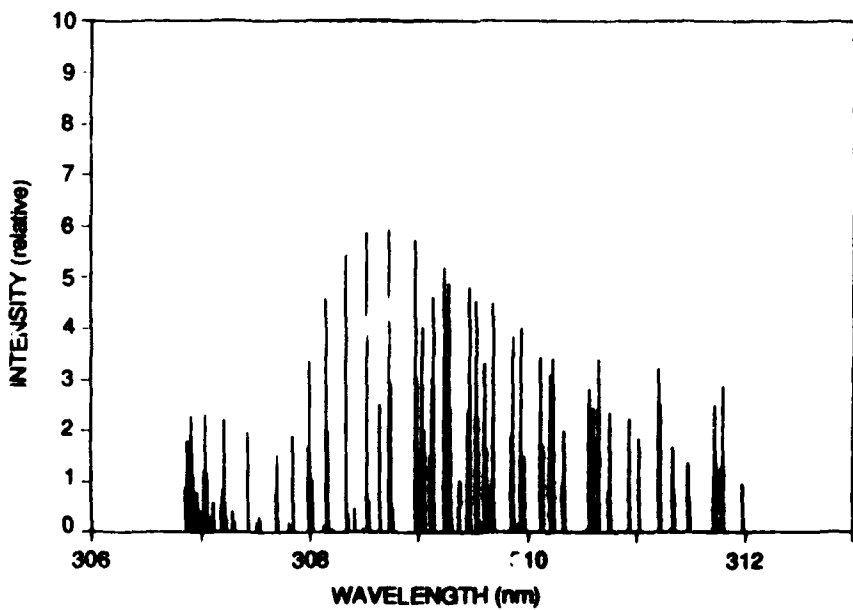


Figure A-5

Simulated OH spectrum for 2000 K and 1 atm with Pressure and Doppler Broadening

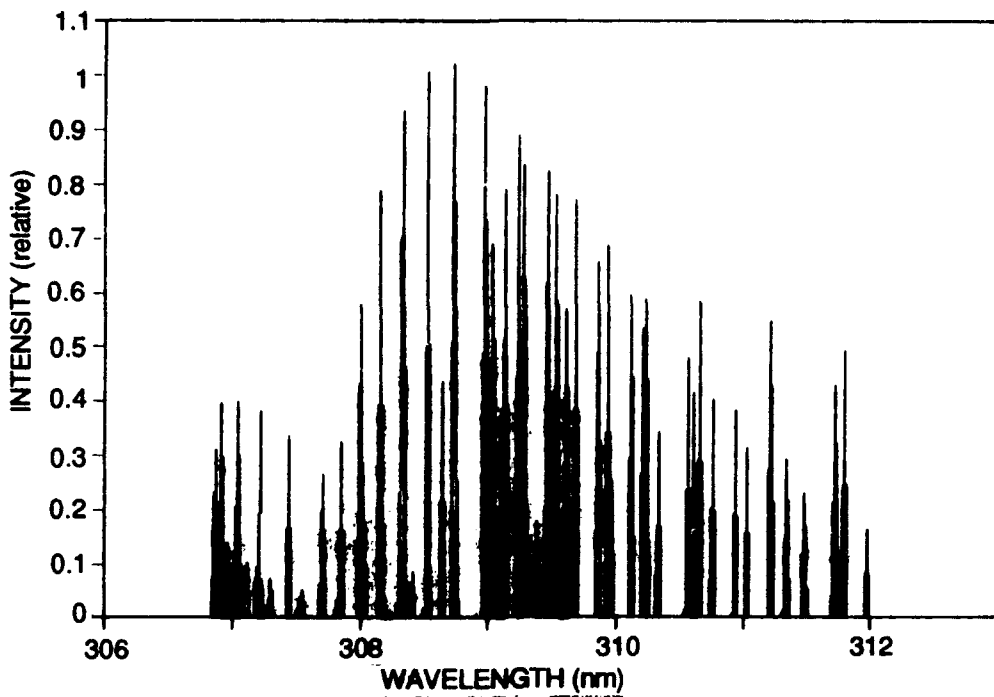


Figure A-6

Simulated OH Spectrum for 2000 K and 10 atm with Pressure and Doppler Broadening

Functional Dependence of Absorbance

Integrated Line Strength:

$$\int k_w dw = k_{ji}$$

$$k_{ji} = \frac{\pi e^2}{m_e c^2} N_i f_{ji}$$

$$f_{ji} = \frac{m_e}{8\pi^2 e^2} \frac{g_i}{g_j} \frac{1}{w_{ij}^2} A_{ij}$$

$$\therefore k_{ji} = \frac{1}{8\pi c} \frac{g_i}{g_j} \frac{1}{w_{ij}^2} N_j A_{ij}$$

where:

- $k_w$  - absorption coefficient as a function of wave number  
 $w$  - wave number  
 $k_{ji}$  - integrated line strength  
 $e$  - electron charge  
 $m_e$  - electron mass  
 $c$  - speed of light  
 $N_j$  - population in lower state  $j$   
 $f_{ji}$  - oscillator strength for transition from  $j$  to  $i$  state  
 $g_i, g_j$  - degeneracy of upper and lower state  
 $w_{ij}$  - wave number for transition from  $i$  to  $j$   
 $A_{ij}$  - Einstein A coefficient for  $i$  to  $j$  transition.

### Absorbance for Triangular Line Shapes (Derivation is valid for $\Delta\lambda_a \leq \Delta\lambda_s$ )

Note that the triangular line shape is a crude model of the gaussian absorption line shape.

The monochromator line shape, for a perfect system, is triangular:

$$A = \frac{\text{Energy Absorbed}}{\text{Incident Energy}} = \frac{\frac{2}{2} \int_{-\Delta\lambda_a}^0 I_0(\lambda) k_\lambda \ell d\lambda}{\frac{2}{2} \int_{-\Delta\lambda_s}^0 I_0(\lambda) d\lambda}$$

$$k(\lambda) = k' \left( \frac{2}{\Delta\lambda_a} \lambda + 1 \right) \quad \text{for } \frac{-\Delta\lambda_a}{2} < \lambda < 0$$

$$I_0(\lambda) = I' \left( \frac{2}{\Delta\lambda_s} \lambda + 1 \right) \quad \text{for } \frac{-\Delta\lambda_s}{2} < \lambda < 0$$

where  $k'$  and  $I'$  are the peak absorption and source intensity values and  $\lambda$  is considered relative to the center of the absorbing line.

**Integration Yields:**

$$A = k' \frac{\Delta\lambda_a}{\Delta\lambda_s} \left[ 1 - \frac{1}{3} \frac{\Delta\lambda_a}{\Delta\lambda_s} \right] \ell$$

Recall Line Strength,  $k_{ji}$ :

$$k_{ji} = 2 \int_{\frac{-\Delta\lambda_a}{2}}^0 k_\omega d\omega = 2 \int_{\omega_0}^{\omega_1} k_\omega d\omega$$

transforming  $k(\lambda)$  via  $\lambda = 1/\omega$ , integrating and assuming  $(\omega_0 - \omega_1)/\omega_0 \ll 1$ :

$$k_{ji} = k' \Delta\omega$$

where:

- $I_0(\lambda)$  - source radiation as a function of  $\lambda$   
 $k_\lambda$  - absorption coefficient as a function of  $\lambda$   
 $\lambda$  - wavelength  
 $\Delta\lambda_{a,s}$  - absorption and source line widths  
 $\Delta\omega$  - absorption line width in wave numbers.

Using Eqs. (A-1), (A-2) and (A-3):

$$\frac{A}{N} = \frac{\Delta\lambda_a}{\Delta\lambda_s} \left[ 1 - \frac{1}{3} \frac{\Delta\lambda_a}{\Delta\lambda_s} \right] \ell \left( \frac{1}{8\pi c} \frac{g_i}{g_j} \right) \phi_j A_{ij}$$

where:

- $N$  - total number density for the system  
 $\phi_j$  -  $N_j/N$  - ground state relative rotational population

### References

1. Chidsey, J.L. and Crosley, D-R, "Calculated Rotational Transition Probabilities for the A-X System of OH," *J. Quant- Spectrosc. Radiat. Transfer* 23, 187 (1980).
2. Dieke, G.H. and Crosswhite, H.M., "The Ultraviolet Bands of OH Fundamental Data," *J. Quant. Spectrosc. Radiat. Transfer* 2, 97 (1962).
3. Rouse, P.E. and Engleman, R., Jr., "Oscillator Strengths from Line Absorption in a High Temperature Furnace - I. The (0,0) and (1,0) Bands of the  $A^2\Sigma^+$  -  $X^2\Pi_i$  Transition in OH and OD," *J. Quant. Spectrosc. Radiat. Transfer* 13, 1503 (1973).
4. Rea, E.C., Jr., Chang, A.J., and Hanson, R.K., "Shock-Tube Study of Pressure Broadening of the  $A^2\Sigma^+ \leftarrow X^2\Pi(0,0)$  Band of OH by Ar and N<sub>2</sub>," Paper 86-3, The Combustion Institute (Banff - Alberta), April 1986.